ISTANBUL TECHNICAL UNIVERSITY ★ GRADUATE SCHOOL

GRAPHENE BASED PATCH ANTENNA DESING WITH SWITCHABLE POLARIZATION FOR THZ BAND

M.Sc. THESIS

Güner Atalık

Department of Communication Systems

Satellite Communication and Remote Sensing Programme

MAY 2024

ISTANBUL TECHNICAL UNIVERSITY ★ GRADUATE SCHOOL

GRAPHENE BASED PATCH ANTENNA DESING WITH SWITCHABLE POLARIZATION FOR THZ BAND

M.Sc. THESIS

Güner ATALIK
(705181030)

Department of Communication Systems

Satellite Communication and Remote Sensing Programme

Thesis Advisor: Asst.Prof. Dr Kamil KARAÇUHA

MAY 2024

ISTANBUL TEKNİK ÜNİVERSİTESİ ★ LİSANSÜSTÜ EĞİTİM ENSTİTÜSÜ

THZ BANDI İÇİN DEĞİŞTİRİLEBİLİR POLARİZASYONLU GRAFEN TABANLI YAMA ANTEN TASARIMI

YÜKSEK LİSANS TEZİ

Güner ATALIK
(705181030)

İletişim Sistemleri Anabilim Dalı

Uydu Haberleşmesi ve Uzaktan Algılama Programı

Tez Danışmanı: Asst.Prof. Dr Kamil KARAÇUHA

MAYIS 2024

Güner Atalık, an M.Sc. student of ITU Graduate School 705181030 successfully defended the thesis entitled “GRAPHENE BASED PATCH ANTENNA DESING WITH SWITCHABLE POLARIZATION FOR THZ BAND”, which he prepared after fulfilling the requirements specified in the associated legislations, before the jury whose signatures are below.

Thesis Advisor: Dr. Öğr. Üyesi Kamil KARAÇUHA ....
Istanbul Technical University

Jury Members: **Prof. Dr. Selçuk PAKER** ....
Istanbul Technical University

Prof. Dr. Evren EKMEKÇİ ....
Suleyman Demirel University

Date of Submission : 24 May 2024
Date of Defense : 07 July 2024

To my family and beloved wife,

FOREWORD

This thesis is the final phase of the journey of my Master’s study in Satallite Communication and Remote Sensing.

First of all, I would like to express my gratitude to my advisor, Asst. Prof. Dr. Kamil KARAÇUHA, for his assistance and support throughout the thesis process.

I am deeply grateful to my beloved spouse, Ferinoosh, who convinced me to complete my thesis and has always supported me. I also want to express my gratitude to my family.

January 2024

Güner ATALIK
(Electric-Electronic Engineer)

TABLE OF CONTENTS

Page

ABBREVIATIONS

LP : Linear Polarization
RHCP : Right-Hand Circular Polarization
LHCP : Left-Hand Circular Polarization
E : Electric Field Intensity
H : Magnetic Field Intensity
2D : Two Dimensional
AR : Axial Ratio
RFID : Radio Frequency Identification
AM : Amplitude Modulation
UAV : Unmanned Aerial Vehicle
VSWR : Voltage Standing Wave-Ratio
RL : Return Loss
CW : Clockwise
CCW : Counter-Clockwise
RLC : Resistor (R), Capacitor (C), and Coil (L)

LIST OF TABLES

Page

LIST OF FIGURES

Page

GRAPHENE-BASED PATCH ANTENNA DESIGN WITH SWITCHABLE POLARIZATION FOR THZ BAND

SUMMARY

Today, with the development of technology, antennas with higher bandwidth and operating at higher frequencies have become widespread. Especially in recent years, antennas operating at frequencies of 0.3 THz and above have appeared. THz band antenna applications have gained momentum in the last decade. Of course, advances in material technology have contributed greatly to reaching these frequencies and bandwidths. The most important of these, and the material that forms the basis of our work, is Graphene due to its unique electrical properties. In addition, we aimed to design a microstrip antenna with switchable polarization to eliminate losses such as polarization mismatch or omnidirectional fading. Different surface structures were obtained using copper and graphene on the microstrip antenna. The most important feature of graphene in our study is that its conductivity varies depending on the bias voltage applied to the graphene. In this way, the conductivity of the surfaces using graphene can be adjusted. This makes it possible to realize varying polarizations on a single structure. In the designs, the antenna structure provides Linear Polarization (LP), Right-Hand Side Circular Polarization (RHCP), and Left-Hand Side Circular Polarization (LHCP).

The biggest problem in this study and the thesis's main focus was obtaining LP, RCHP, and LHCP with a single feed. In order to realize these polarizations in a single structure, a circular antenna operating in linear polarization was first designed. The next stage of the design was to add structures that would provide circular polarization into the same design. For this purpose, asymmetric slots were added to the structure. An asymmetric slot is actually used to show that the slots shrink clockwise or counterclockwise and are located on the antenna surface. In the study, it was seen that the direction of shrinkage of the slots is the same as the direction of rotation of the currents. To adjust the Axial Ratio, the shrinkage rate of the slots was examined parametrically. Thus, RHCP and LHCP antennas were obtained from the antenna operating as LP. Afterward, graphene was added to the changing slot structure, and the conductivity of these regions was made variable. Thus, we have realized an antenna structure with variable polarization using only one simple feed structure. All designed antennas are simulated using CST Studio Suite.

THZ BANDI İÇİN DEĞİŞTİRİLEBİLİR POLARİZASYONLU GRAFEN TABANLI YAMA ANTEN TASARIMI

ÖZET

Günümüzde gelişen teknoloji ile birlikte daha yüksek bant genişliğine sahip ve daha yüksek frekanslarda çalışan antenler yaygınlaşmaya başlamıştır. Özellikle son yıllarda 0.3 THz ve üzeri frekanslarda çalışan antenler ortaya çıkmıştır. THz bandı anten uygulamaları son on yılda ivme kazanmıştır. Bu gelişmeler, telekomünikasyon, radar sistemleri ve medikal görüntüleme gibi çeşitli alanlarda devrim niteliğinde yenilikler sunmaktadır. Elbette bu frekanslara ve bant genişliklerine ulaşılmasında malzeme teknolojisindeki gelişmelerin büyük katkısı olmuştur. Malzeme teknolojisi, antenlerin performansını artırma ve yeni işlevler kazandırma açısından kritik bir rol oynamaktadır. Bu alandaki en önemli malzemelerden biri ve çalışmamızın temelini oluşturan malzeme, benzersiz elektriksel özellikleri nedeniyle Grafen'dir. Grafen, tek atom kalınlığında, karbon atomlarından oluşan bir malzemedir ve olağanüstü iletkenlik, esneklik ve dayanıklılık gibi özelliklere sahiptir. Grafen'in elektriksel özellikleri, anten teknolojisinde çığır açıcı yenilikler sunmaktadır. Özellikle polarizasyon uyumsuzluğu veya çok yönlü sönümlenme gibi kayıpları ortadan kaldırmak için değiştirilebilir polarizasyona sahip bir mikroşerit anten tasarlamayı amaçlanmıştır. Bu tür bir anten, farklı uygulamalarda daha verimli ve güvenilir performans sağlamaktadır. Çalışmamızda, mikroşerit anten üzerinde bakır ve grafen birlikte kullanılarak farklı yüzey yapıları elde edilmiştir. Bakır, yüksek iletkenlik özelliği ile antenlerin verimliliğini artırırken, grafen ise esnek ve ayarlanabilir iletkenlik özellikleri ile tasarımda esneklik sağlamaktadır. Grafenin en önemli özelliklerinden biri, iletkenliğinin grafene uygulanan bias voltajına bağlı olarak değişmesidir. Bu sayede grafen kullanılan yüzeylerin iletkenliği ayarlanabilmektedir. Bu da tek bir yapı üzerinde değişen polarizasyonların gerçekleştirilmesini mümkün kılmaktadır. Yapılan tasarımlarda anten yapısı Doğrusal Polarizasyon (LP), Sağ Taraf Dairesel Polarizasyon (RHCP) ve Sol Taraf Dairesel Polarizasyon (LHCP) sağlamaktadır. Bu polarizasyon çeşitliliği, antenlerin farklı frekanslarda ve

uygulamalarda optimal performans göstermesini sağlamaktadır. Ayrıca, değiştirilebilir polarizasyon özelliği, antenlerin çok çeşitli senaryolarda kullanılabilmesini mümkün kılmaktadır.

İlk olarak, sonraki adımlara temel oluşturması adına ilk bölümde anten temelleri hakkında genel bir bilgilendirme yaparak teze giriş yapmaktır. Bu kısımda anten çalışma ve geometrik yapısının belirlenmesinde oldukça önemli olan iletim hattı modeli ve boşluk modeli anlatılmıştır. Anten geometrisinin belirlenmesinde ve bunların belirlenmesinde etkin olan saçaklanma etkisi ve model içerisindeki hesaplamalara olanak sağlayan varsayımlar detaylı bir şekilde açıklanmıştır. Antenin ışıma mekanizmasının anlaşılması adına boşluk modeli üzerinde durulmuş, bu model içerisindeki mekanizmalar ve bu mekanizmalara etki eden anten boyutları arasındaki ilişkiler de ayrıntılı bir şekilde incelenmiştir. Ayrıca, anten besleme yöntemlerinden detaylıca bahsedilmiştir. Antenlerin verimli çalışabilmesi için doğru besleme yöntemlerinin seçimi çok önemlidir. Bu bağlamda, çeşitli besleme teknikleri ve bu tekniklerin avantajları ve dezavantajları ele alınmıştır. Tasarımların doğru bir şekilde değerlendirilmesini sağlamak ve yama antenlerin işleyişinin detaylıca anlaşılması için temel anten parametreleri hakkında bilgiler verilmiş ve açıklanmıştır. Bu parametreler arasında kazanç, verimlilik, bant genişliği, polarizasyon ve radyasyon modeli gibi önemli kavramlar yer almaktadır. Bu bilgiler, anten tasarımının optimizasyonu ve performans değerlendirmesi açısından kritik öneme sahiptir. Sonuç olarak, gelişen teknoloji ve malzeme bilimi sayesinde THz bandında çalışan antenler, gelecekte iletişim ve diğer teknolojik alanlarda önemli yenilikler sunmaya devam edecektir. Grafen gibi ileri malzemelerin kullanımı, antenlerin performansını artırmakla kalmayıp, aynı zamanda daha esnek ve çok yönlü çözümler sunmaktadır. Bu da, daha hızlı, daha güvenilir ve daha verimli iletişim sistemlerinin geliştirilmesine katkı sağlamaktadır.

Tezin içerisinde oldukça kilit rol oynayan grafenin yapısı detaylıca açıklanmıştır. Grafen yapısını oluşturan yapı içerindeki electron davranışları , orbital yapıları ve enerji-moment diyagramı üzeirnden açıklanmıştır.Literatür içerisinde grafenin iletkenliğinin hesaplanmasında kullanılan Kubo formülasyonu anlatılmış ve formül içerindeki parametreler ve etkilerinden bahsedilmiştir.Bu noktada tez hedeflerine ulaşmak adına dairesel polarizasyona sahip antenler ve grafen kullanılarak üretilen farklı besleme yapısına, alt yalıtkana ve polarizasyona sahip antenler incelenmiş ve değerlendirilmişir. Bu yapılardan yola çıkılarak doğrusal polarizasyona sahip yama anten tasarımı gerçekleştirilmiştir. Tasarım ilk olarak HFSS programında sınanmıştır. Ardından tasarıma asimetrik yarıklar eklenerek antenin dairesel polarizasyon göstermesi sağlanmıştır. Ardından grafenin daha kolay bir şekilde simule edilebilmesi için yapılan tüm simulasyonlar ve mevcut tasarım CST Studio Suite programına taşınmıştır. İlk olarak dairesel yama kenarlarında oluşturulan asimetrik slotların içerisi üç farklı kimyasal potansiyele sahip grafen ile doldurularak antenin Doğrusal, Sağ-el Dairesel ve Sol-el Dairesel polarizasyonlar arasında bu üç farklı grafen bölgesiin kimyasal potansiyelleri manipule edilerek aynı yapıdaki anten yapısı içerisinde geçiş sağlanmıştır. Yapılan bu ilk tasarımın eksiklerinden biri dairesel polarizasyon durumunda aksiyel oranlarının sınır bir değerde olması olduğu görülmüştür.

İlk tasarımdaki dairesel polarizasyonların iyileştirilmesi için ikinci bir tasarım olarak anten ortasına asimetrik bir haç şekli ilave edilmiştir. Yarık içerisine üç farklı kimyasal potansiyele sahip grafen kullanılarak antenin yapısının aynı kalarak polarizasyonlar arasında geçiş yapması sağlanmıştır. Tasarım içerisinde manipule edilen grafen kullanılarak yapılan polarizasyonlar arasında geçiş ile beraber anten çalışma frekenasının değiştiği görülmüştür. Aksiyel oranın ise neredeyse sıfıra yakın olduğu görülmüştür. Bu tasarımın eksikliği olarak ise polarizasyonlar arasındaki çalışma frekansı farklılıkları gösterilebilir.

Birinci ve ikinci tasarımların eksikliklerin iderilmesi için üçüncü bir tasarım yapılmıştır. Yapılan tasarımda dairesel yama anten üzerine cassini ovaline benzer bir eğriye sahip yonca yaprakları merkezde dört yaprak olacak şekilde yerleştirilmiştir. Bu asimetrik yapraklar içinde önceki tasarımlardan farklı olarak biribirinden farklı iki kimyasal potansiyele sahip grafen kullanılmıştır. Tasarımın aksiyel oranı ilk tasarımdan oldukça iyi olmakla beraber farklı polarizayonlardaki çalışma frekanslarına bakıldığında mezkez freknaslarının aynı olduğu görülmüştür. Üçüncü ve son tasarımda benzer prensiplerden yaralanarak farklı bir geometri kullanılarak önceki tasarımların eksiklikleri giderilmiştir.

Tez içerisinde yama anten çalışma prensipleri vey ama anten parametreleri anlatılarak bir temel oluşturulmuş sonrasında tasarımda kritik bir rol oynayan ve çalışmaya değer katan grafen ve grafenin modellenmesi hakkında bilgiler verilmiştir. Ardından üç farklı tasarım ortaya konmuş tasarımların birbirilerine karşı avantaj ve dezavantajları

berlirtilmiştir. Yapılan üç tasarımın da polarizasyonlar arasında geçiş yapma özellikleri bulunduğu görülmüştür.

1. INTRODUCTION

Due to the increasing need for high-speed communication, telecommunication systems endeavor to find the most effective ways to transmit data. Antennas, a cornerstone component of communication systems, play a critical role in data transmission. In a typical wireless communication system, increasing the gain of the deployed antennas enhances wireless coverage, minimizes errors, increases achievable bit rates, and reduces battery consumption of wireless communication devices. One of the main reasons for losses in communication systems is polarization mismatch in transceiver systems. Achieving identical polarization requires having equivalent axial ratios, spatial orientations, and polarization senses between the transmitter and receiver**.** [1] To overcome this polarization mismatch problem, the main focus of this thesis is to present a polarization switchable antenna structure. In doing so, the compactness of the structure and its structural simplicity, such as being fed by a single transmission line, have been taken into consideration for future manufacturability. However, due to all these reasons, the design phase is also challenging. To achieve this, it is first necessary to understand circular polarization. Although circular polarization can be achieved in many different ways, the best choice for us was the structure that allows the most compact design. In this design, the transmission line is connected diagonally to the antenna. In order to increase the axial ratio of the antenna, two perpendicular axes of symmetry are created on the antenna by adding or removing various elements to the antenna edges on the diagonal perpendicular to the diagonal to which the transmission line is connected. All these studies constitute the first stage of our thesis. At this stage, in order to be innovative, an antenna design with circular polarization operating in the THz band, which has been studied in recent years, has been revealed. The antenna has an operating frequency of 5.98 THz.

In the second phase of the thesis, Graphene structures, which have increased in use with a better understanding of their usage areas in the last ten years, were used in the design. The conductivity of these graphene structures varies according to the bias voltage applied to them. In this way, while the antenna remains structurally the same, the polarization of the antenna can be changed according to the voltage applied to these variable conductivity surfaces. In this second stage of the thesis, these graphene structures are modeled first, and how their electrical properties change depending on the applied voltage is modeled. Kobo Formula was used to model the conductivity and permittivity of graphene.

After the graphene modeling was done, these graphene structures were placed in the antenna structure, and antenna designs that can change polarization were tried to be realized by using these structures whose conductivity can change within the antenna. For this, 3 different designs were realized in the thesis. As a result of this study, antennas with switchable polarization (RHCP, LHCP, and LP) operating around 6 THz were obtained.

1.1 Purpose of Thesis

Nowadays, due to the increasing use of mobile devices and the need for high data transfer speed, more efficient communication methods are sought. Polarization mismatch is one of the most important factors causing inefficiency. Polarization mismatch increases errors, reduces bit rate, and causes the device to consume more power. Circular polarization offers a suitable solution to resolve this situation. In the face of increasing data speed and bandwidth, material and production technologies that allow communication at higher frequencies have begun to move from theory to reality. The most interesting and high potential of these materials is Graphene**.** [2]

The primary aim of this study, which focuses on all these problems, is to design an antenna with switchable polarization. For the secondary purpose, we wanted the antenna design to have a simple structure. To reach that goal, it is necessary first to understand what circular polarization is and how circular polarization can be achieved practically. We see in the literature that circular polarization can be achieved by 3 different methods. It is the connection of two different feed points to the antenna, giving a phase difference of 90 degrees from two 90-degree edges. In this method, a feed network that will create a phase difference must be designed. Another method is to obtain an antenna array by rotating linearly polarized antennas by 90 degrees. In this method, even if the same antennas are used in a 4×4 array, at least one feed must be used for each antenna. Additionally, since the structure is an array, it is considerably larger than a single antenna. The feed network in the first method makes the system difficult. In the second method, the system will be complex as a large number of feeds will need to be used, and the cost will increase since it consists of 4 antennas instead of a single antenna.

2. MICROSTRIP ANTENNA BASICS

2.1 Introduction

In this work, all terms are explained in an easily understandable way, and sometimes analogies are used. Nowadays, in communication, we are transmitting information with electromagnetic waves from one point to another. These electrical signals can be transmitted in two ways: via transmission line (fiber cables, phone cables, etc.) or in empty space using antennas (one receiver and one transmitter antenna at least in one system). These transmission lines consist of two parts: a conductive material and an isolation coating. The main purpose of this coating material is to confine the electrical signals and energy of the electromagnetic wave to a near region or, ideally, inside the transmission line. On the contrary, the purpose of antennas is to radiate these electrical signals far away. Basically, it can be said that transmission lines serve as a guide for the transmission of electromagnetic waves, while antennas are converters that convert guided waves (come from a transmission line) to a free-space wave or vice versa. In order to explain how the antenna does this, we first need to understand how antennas create these electromagnetic waves. These waves are actually created by electrical charges moving with acceleration on the antenna surface, as shown in Figure 2.1. This movement creates a harmonic oscillation depending on the antenna frequency. To explain it more simply with an analogy, think of a container under a dripping faucet. Each drop that drips from this faucet refers to an electrical charge that carries a piece of our electrical signal. Frequency is referred to as how many drops drip in one second. In this case, we see a fluctuation on the surface of the container, which is our space, depending on the size and frequency of the drops.

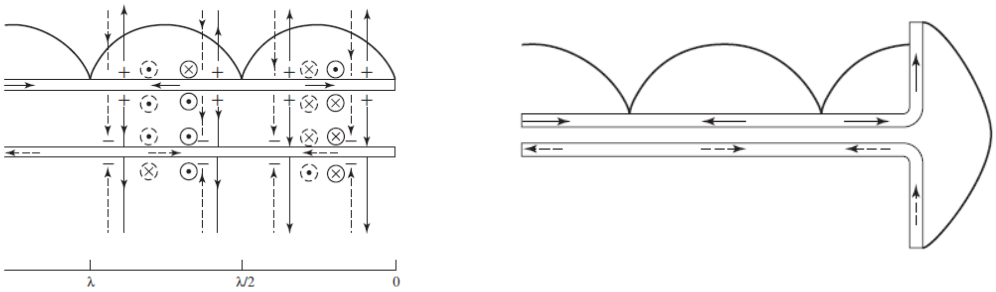

Figure 2.1 : Antenna working principle and how the Antenna creates Electromagnetic waves [1]

The spectrum is classified according to frequencies to organize communication systems. For example, in RFID applications or AM broadcasting, the used bands are Low Frequency (LF) and Medium Frequency (MF), which means frequency range from 30 to 300 kHz for LF and from 300 kHz to 3 MHz for (MF) and the wavelength is from 10 to 1 km for LF and from 1 km to 100 m for MF. As can be seen from this example, frequencies are classified according to applications, and frequency ranges are called bands (LF, MF, etc.). In Table 2.1, band descriptions and properties like frequency and wavelength are used.

Table 2.1 : Electromagnetic Spectrum [1]

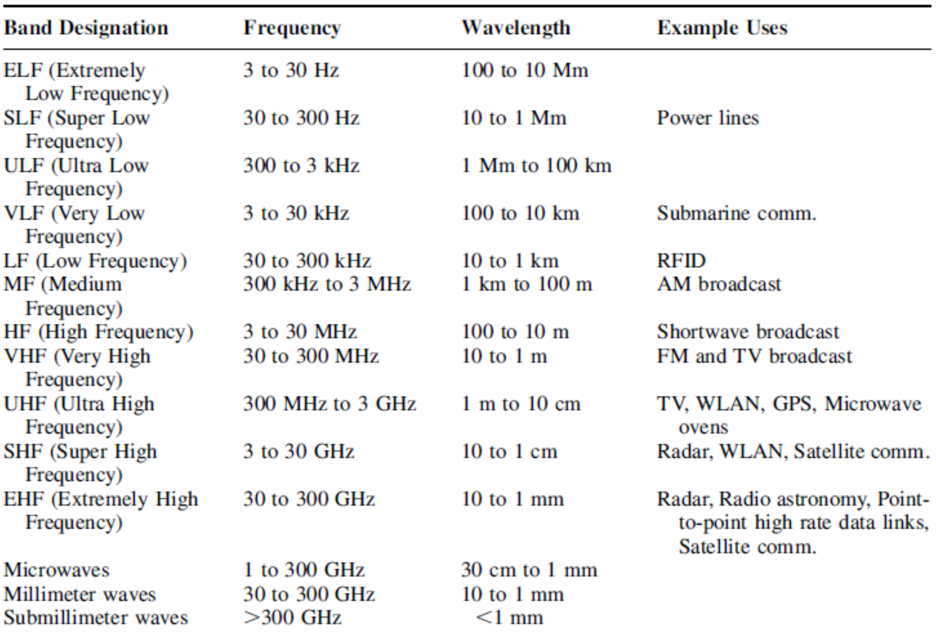

Band Designation	Frequency	Wavelength	Example Uses
ELF (Extremely Low Frequency)	3 to 30 Hz	100 to 10 Mm	
SLF (Super Low Frequency)	30 to 300 Hz	10 to 1 Mm	Power lines
ULF (Ultra Low Frequency)	300 to 3 kHz	1 Mm to 100 km	
VLF (Very Low Frequency)	3 to 30 kHz	100 to 10 km	Submarine comm.
LF (Low Frequency)	30 to 300 kHz	10 to 1 km	RFID
MF (Medium Frequency)	300 kHz to 3 MHz	1 km to 100 m	AM broadcast
HF (High Frequency)	3 to 30 MHz	100 to 10 m	Shortwave broadcast
VHF (Very High Frequency)	30 to 300 MHz	10 to 1 m	FM and TV broadcast
UHF (Ultra High Frequency)	300 MHz to 3 GHz	1 m to 10 cm	TV, WLAN, GPS, Microwave ovens
SHF (Super High Frequency)	3 to 30 GHz	10 to 1 cm	Radar, WLAN, Satellite comm.
EHF (Extremely High Frequency)	30 to 300 GHz	10 to 1 mm	Radar, Radio astronomy, Point-to-point high rate data links, Satellite comm.
Microwaves	1 to 300 GHz	30 cm to 1 mm	
Millimeter waves	30 to 300 GHz	10 to 1 mm	
Submillimeter waves	>300 GHz	<1 mm	

In addition to its differences in terms of operation, as explained in the previous paragraph, transmission lines are also a good option for transmitting electromagnetic waves, such as antennas. That brings us to the next question: “How do we choose one of these options: transmission lines or antennas?”. Although the first thing that comes to mind is propagation loss during transmission, the answer to this question varies depending on many factors. Transmission lines are generally used over short distances and at low frequencies. The cost of transmission lines to be used at high frequencies or in long-distance applications is considerably higher than that of antennas. Apart from this, transmission lines can be preferred in high-frequency applications as they offer high bandwidth. To illustrate the cost increase of transmission lines, fiber optic cables can carry up to 60 terabits of data per second, just below the speed of light, while copper cables have a maximum carrying capacity of up to 40 gigabits per second. However, while the cost of copper cables is between 0.9-1.55 dollars per foot, the cost of fiber cables varies between 1-6 dollars per foot.[3] As seen in the illustration, antennas are preferred due to increasing transmission line costs as distances increase or frequency increases. For example, in radio communication, using antennas is more cost-effective than using transmission lines. On the other hand, transmission lines are less affected by factors such as weather conditions, especially those buried underground.

To explain antennas and their place in our daily life better, there are antennas on all vehicles in the air, on the ground and at sea, and on all mobile devices. All broadcasting TV and Radio channels need an antenna. At the same time, it is not surprising to see different types of antennas being used in many places, from satellite communications to medical devices and radio telescopes used for space observations. In the military industry, antennas are used in many places, such as modern guided missiles, missile shield systems, smart ammunitions, UAVs (unmanned aerial vehicles), etc.

2.2 Antenna Parameters

Antennas are devices that can operate in two directions. They show the same characteristic behavior during transmission or reception; for example, the transmitting antenna ensures the propagation of the signal coming from the transmission line while acting as a receiver; the antenna structure collects electromagnetic waves from the antenna surface and directs them toward the attached transmission line.

Some antennas can focus in a certain direction, such as lenses that allow optical focusing to a certain point, like eyeglasses. This shows us a directionality characteristic of the antenna. Directivity is actually an indicator that shows in which directions the antenna transmits the signal better. The radiation pattern shows radiation around the antenna changes angularly during transmission. Additionally, while in the receiving state, the antenna picks up the incoming wave from a specific direction based on its radiation pattern. The higher the value in this pattern, the more efficient the antenna captures the signal. 'Figure 2 depicts the Radiation Pattern of directional antennas, which includes a primary lobe and smaller side lobes that radiate alongside it. In this pattern, the values labeled as S correspond to the power density measured at a constant distance r from the antenna.

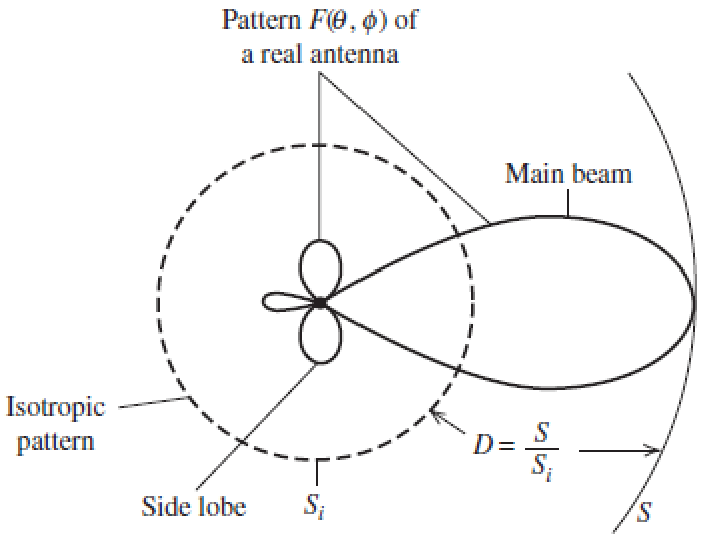

Figure 2.2 : Radiation Pattern and Directivity [1]

To explain it more simply with an example, Directional Antennas can be preferred for communication between two specific points. These antennas display a Radiation Pattern composed of main and side lobes. Contrarily, since antennas such as radio and television broadcasting antennas need to spread their broadcast in all directions to the region where they are located, the Radiation Patterns of these types of antennas emit almost the same power in all directions, and their pattern shapes are circular. An antenna with this design is commonly referred to as an Isotropic Antenna. The power radiated from the main lobe of a directional antenna is much more concentrated than that of an isotropic spatial distribution. This is important because it indicates that as the directivity of the antenna increases, the radiation towards the direction of the main lobe increases. In addition, the wave radiated will be weak due to losses on the antenna. To define this, we use the feature that we define as Gain and denote as G. Gain (G) is simply Reduced Directivity due to losses.

2.2.1 Radiation Power Density

Through the use of electromagnetic waves, data can be transmitted between two points using a remote medium. It is at that point normal to expect the energy and power to be related to electromagnetic fields. We will characterize the power of an electromagnetic wave as follows:

$$\mathrm{W} = \mathcal{E} \times \mathrm{H} \tag{2.1}$$

W= instantaneous Poynting vector(W/m^2)

Ɛ = instantaneous Electric field intensity (V/m)

H = instantaneous Magnetic field intensity (A/m)

By considering the density of power indicated by the Poynting vector, we can calculate the overall power passing through a closed surface by summing the perpendicular component of the Poynting vector (W) over the entire surface, as depicted below:

$$\mathcal{P} = \oiint_S \mathcal{W} \cdot ds = \oiint \int_S \mathcal{W} \cdot \hat{\mathrm{n}} dd \tag{2.2}$$

$\mathcal{P}$ = instantaneous total power (W)

n̂ = unit vector perpendicular to the surface

da = infinite small area of the closed surface (m^2)

The average in time of the Poynting vector or average density of power can be calculated as;

$$\mathrm{W}_{\mathrm{av}}(x, y, z) = [\mathcal{W}(x, y, z; t)]_{\mathrm{av}} = \frac{1}{2}\mathrm{Re}[E \times H^*] \ \ (\mathrm{W/m^2}) \tag{2.3}$$

The ½ calculation shows up within the condition since the E and H fields peak to crest values, and for RMS (Root Mean Square) values, this factor must be disregarded. The real portion of (ExH)/2 speaks to the normal (real) density of power. It is accurate to say that the imaginary component reflects the reactive power density associated with electromagnetic fields. One can calculate the average radiated power of the antenna by using the following formula:

$$\begin{aligned} P_{\mathrm{rad}} &= P_{\mathrm{av}} = \oiint_S \mathrm{W}_{\mathrm{rad}} \cdot ds = \oiint_S \mathrm{W}_{\mathrm{av}} \cdot \hat{\mathrm{n}} da \\ &= \frac{1}{2} \oiint \int_S \mathrm{Re}\,(\mathrm{E} \times \mathrm{H}^*) \cdot ds \end{aligned} \tag{2.4}$$

All directions receive equal transmission from the perfect isotropic antenna. In spite of the fact that it is not accessible in hone, it gives a helpful isotropic reference for comparing other antennas. Since its radiation is similarly conveyed in all directions, the Poynting vector will not be a work of the worldwide facilitate points θ and ϕ.

Moreover, there will be a component in the radial direction; thus, the entire energy transmitted can be described as:

$$P_{\text{rad}} = \oiint \mathrm{W}_0 \cdot ds = \int_0^{2\pi}\int_0^{\pi} [\hat{\mathrm{a}}_r W_0(r)] \cdot [\hat{\mathrm{a}}_r r^2 \sin\ \theta d\theta d\phi] = 4\pi r^2 W_0 \tag{2.5}$$

$$\mathrm{W}_0 = \hat{\mathrm{a}}_r W_0 = \hat{\mathrm{a}}_r \left(\frac{P_{\text{rad}}}{4\pi r^2}\right) (\mathrm{W/m^2}) \tag{2.6}$$

and the consistent dispersal of power density across a circular surface with a radius of r.

2.2.2 Radiation Intensity

Radiation that is focused in a specific direction can be defined as "the amount of power transmitted from an antenna per unit of solid angle”. The far-field measurement of radiation intensity can be calculated by multiplying the intensity by the distance squared and given below:

$$U = r^2 W_{\text{rad}} \tag{2.7}$$

U = Intensity of radiation (W/unit solid angle)

W_{rad} = density of radiation ($\mathrm{W/m^2}$)

The equation below calculates the overall power by coordinating the radiation intensity across the entire solid angle of 4π;

$$P_{\text{rad}} = \oiint_{\Omega} U d\Omega = \int_0^{2\pi}\int_0^{\pi} U \sin\theta d\theta d\phi \tag{2.8}$$

where dΩ = element of solid angle = sinθ dθ dϕ.
In the scenario of an isotropic source, both U and W rad will not change with respect to the angles θ and ϕ. Consequently, the equation can be expressed as for a source with isotropic properties.;

$$P_{\text{rad}} = \oiint_{\Omega} U_0 d\Omega = U_0 \oiint_{\Omega} d\Omega = 4\pi U_0 \quad \text{or} \quad U_0 = \frac{P_{\text{rad}}}{4\pi} \tag{2.9}$$

4

2.2.3 Directivity

The proportion of radiation emitted in a specific direction compared to the total radiation emitted in all directions is known as the directivity of an antenna. The usual intensity and strength of radiation equals the total radiated power of the antenna divided by 4π. When the course is not mentioned, the calculation will assume the direction with the highest level of radiation intensity. Put simply, the directivity of a non-isotropic source is equivalent to the ratio of radiation intensity in a specific direction compared to that of an isotropic source and can be determined by the following formula;

$$D = \frac{U}{U_0} = \frac{4\pi U}{P_{\mathrm{rad}}} \quad \text{and} \quad D_{max} = D_0 = \frac{U|_{max}}{U_0} = \frac{U_{max}}{U_0} = \frac{4\pi U_{max}}{P_{\mathrm{rad}}} \tag{2.10}$$

D = directivity (dimensionless)

D_0 = maximum directivity (dimensionless)

U = radiation intensity (W / unit solid angle)

U_{max}= maximum radiation intensity (W /unit solid angle)

U_0 = radiation intensity of isotropic source (w /unit solid angle)

P_{rad} = entire radiated power(W)

$$D(\theta,\phi) = 4\pi \frac{F(\theta,\phi)}{\int_0^{2\pi}\int_0^{\pi} F(\theta,\phi)\sin\theta d\theta d\phi} \tag{2.11}$$

$$D_0 = 4\pi \frac{F(\theta,\phi)|_{max}}{\int_0^{2\pi}\int_0^{\pi} F(\theta,\phi)\sin\,\theta d\theta d\phi} \tag{2.12}$$

This equation can also be written:

$$D_0 = \frac{4\pi}{\left[\int_0^{2\pi}\int_0^{\pi} F(\theta,\phi)\sin\,\theta d\theta d\phi\right] / F(\theta,\phi)|_{max}} = \frac{4\pi}{\Omega_A} \tag{2.13}$$

Let Ω_A denote the beam solid angle, which can be calculated as:

$$\Omega_A = \frac{1}{F(\theta,\phi)|_{max}} \int_0^{2\pi}\int_0^{\pi} F(\theta,\phi)\sin\,\theta d\theta d\phi = \int_0^{2\pi}\int_0^{\pi} F_n(\theta,\phi)\sin\,\theta d\theta d\phi \tag{2.14}$$

$$F_n(\theta,\phi) = \frac{F(\theta,\phi)}{F(\theta,\phi)|_{max}} \tag{2.15}$$

2.2.4 Antenna Efficiency

The use of e_0 (total antenna efficiency) allows for compensation of losses at the input terminals or within the antenna structure. Outlined below are the factors contributing to these losses:

1. Thoughts arising from the difference between transmission line and antenna

2. I^2R losses (conduction and dielectric)

Taken as a whole, the total efficiency can be stated:

$$e_0 = e_r e_c e_d \tag{2.16}$$

e_0 = total efficiency (dimensionless)

e_r = reflection (mismatch) efficiency = $(1 - |\Gamma|^2)$ (dimensionless)

e_c = conduction efficiency (dimensionless)

e_d = dielectric efficiency (dimensionless)

Γ = voltage reflection coefficient at the input terminals of the antenna

[$\Gamma = (Z_{in} - Z_0)/(Z_{in} + Z_0)$ where Z_{in} = antenna input impedance, Z_0 = characteristic the impedance of the transmission line]

VSWR = voltage standing wave ratio calculated;

$$\frac{1+|\Gamma|}{1-|\Gamma|} \tag{2.17}$$

For the most part, e_c and e_d are exceptionally troublesome to calculate, but in spite of the fact that they can be decided tentatively, they cannot be measured independently. In this manner, we are able to type in the condition as follows:

$$e_0 = e_r e_{cd} = e_{cd}(1 - |\Gamma|^2) \tag{2.18}$$

The term "e_{cd}" represents the antenna radiation efficiency, which is utilized to establish the correlation between gain and directivity.

2.2.5 Gain and Realized Gain

When discussing an antenna's gain (in a particular direction), it refers to "the relationship between the intensity in that direction and the radiation intensity that would be received if the antenna emitted radiation evenly." The energy of the radiation is equivalent to the isolated power received by the antenna divided by 4π. In the condition frame, this could be communicated as antenna gain can be calculated utilizing (2.19):

$$\text{Gain } = 4\pi \frac{\text{radiation intensity}}{\text{total input (accepted) power}} = 4\pi \frac{U(\theta,\phi)}{P_{in}} \tag{2.19}$$

In the absence of direction or unclear instructions, the power gain is commonly achieved during maximum radiation.

The total input power (Pin) is directly linked to the total radiated power (Prad)

$$P_{\text{rad}} = e_{cd} P_{in} \tag{2.20}$$

Due to losses of the mismatch and reflections, our equation is;

$$G(\theta,\phi) = e_{cd}\left[4\pi \frac{U(\theta,\phi)}{P_{\text{rad}}}\right] \tag{2.21}$$

Gain and directivity are directly related to each other, and the relationship between them can be shown by the following equations:

$$G(\theta,\phi) = e_{cd} D(\theta,\phi) \tag{2.22}$$

$$G_0(\text{dB}) = 10\log_{10}\left[e_{cd} D_0(\text{ dimensionless })\right] \tag{2.23}$$

2.2.6 Antenna Polarization

Polarization is one of the most difficult parameters to understand. During transmission, an antenna's polarization indicates the specific direction of the propagated wave. Understanding the polarization of electromagnetic waves is crucial to understanding the polarization of antennas. Therefore, we will begin our exploration by examining the former, which will lead us to a better understanding of the latter.

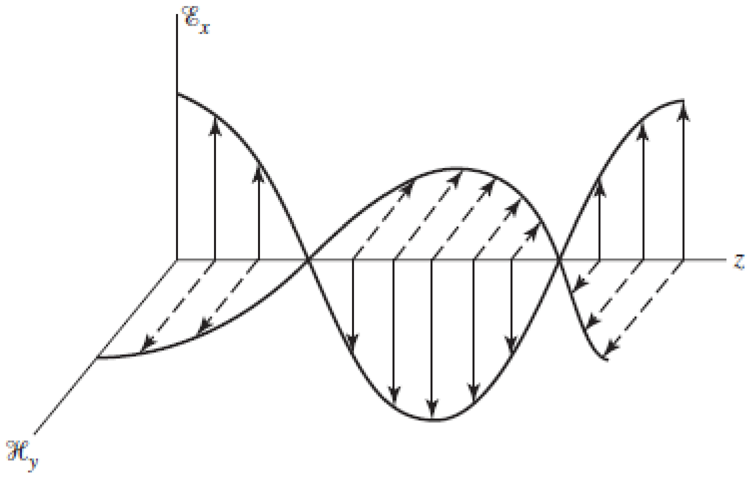

Figure 2.3 : Electric and Magnetic fields of a linear polarized wave [1]

In order to make the concepts in the chapter easier to understand, they will first be shown geometrically and then expressed mathematically. Figure 2.3 shows the electric and magnetic fields that make up a wave. The +Z axis can be considered as the direction in which the wave propagates on the graph, and this interpretation would not be erroneous. Accordingly, if we look at this wave from the +Z axis towards the E_x and H_y plane. The electric field demonstrates linear oscillation ranging from $+E_x$ to $-E_x$ values, originating at point 0 on the E_x-axis. The amplitude of this oscillation corresponds to the size of the E_x (electric field) of the wave. The same is true for the magnetic field magnitude H_y. H_y oscillates linearly on the horizontal axis. It wouldn't be wrong to explain it this way to present a different perspective. Imagine drawing a straight line up and down with your hand. You constantly move up and down without lifting your hand, and as you make this movement, a computer records the position of your hand over time. The oscillation you will see in this recording will form a sinusoidal; that is, it will oscillate similarly to the electrical field of our wave in Figure 2.3. In this case, when time is added as the 3rd dimension to the oscillation you have made only on a straight line in the two-dimensional plane, it creates a sinusoid. For the sake of understanding geometrically, Figure 2.4a and Figure 2.4b can be shown as examples of the oscillation in the E_x and H_y axes, respectively. It wouldn't be wrong to explain it this way to offer a different perspective. Imagine drawing a straight line up and down with your hand. You constantly move up and down without lifting your hand, and as you make this movement, the computer records the position of your hand over time. The oscillation you will see in this recording will create a sinusoidal form;

that is, it will oscillate similarly to the electric field of our wave in Figure 2. In this case, when time is added as the 3rd dimension to the oscillations you make, it creates a sinusoid on a straight line in only a two-dimensional plane. This perspective is very crucial for understanding circular and elliptical polarization.

(*a*) Vertical linear polarization. (*b*) Horizontal linear polarization.

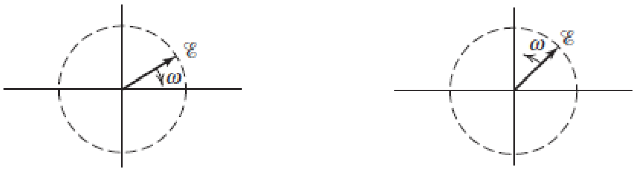

(*c*) Left-hand circular polarization. (*d*) Right-hand circular polarization.

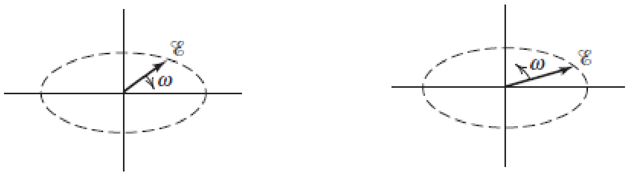

(*e*) Left-hand elliptical polarization. (*f*) Right-hand elliptical polarization.

Figure 2.4 : a) Vertical Linear Polarization b) Horizontal Linear Polarization c) Left-hand Circular Polarization d) Right-hand Circular Polarization e) Left-hand Elliptical Polarization f) Right-hand Elliptical Polarization [4] (Currents outward from page)

To understand other polarizations, we need to make our example a little more complex. In this scenario, allow the electric field to be formed by the combination of two vectors. One of them represents E_x, an electrical field vector with horizontal polarization, and the other represents E_y, an electrical field vector with vertical polarization. Considering that the combination vector of E_x and E_y vectors forms the electrical field of the wave, these two sinuses will form a circular wave as in Figure 2.5a, and its projection will be similar to Figure 2.5b. What distinguishes circular polarization from elliptical polarization is the proportional difference between the maximum magnitudes of the E_x and E_y vectors that form the electrical field of the wave. If the maximum magnitudes of E_x and E_y are equal, the combination will have a circular polarization as in Figure 2.4c or Figure 2.4d. If E_y has a larger magnitude than E_x, the projection of the electric field will have an elliptical polarization, as in Figure 2.4e and Figure 2.4f. The same is true when E_x is greater than E_y. To understand the difference between Right-hand Circular Polarization and Left-hand Circular Polarization, can be effective to use Figure 2.5b. If we consider that the wave in Figure 2.5b represents the change in time of a vector, such as the minute hand of a clock. If the wave is traveling in the +z direction, the minute hand will move counterclockwise, and this is called Right-Hand Polarization. If the wave is traveling in the −Z direction, the minute hand will move clockwise, and this is called Left-Hand Polarization

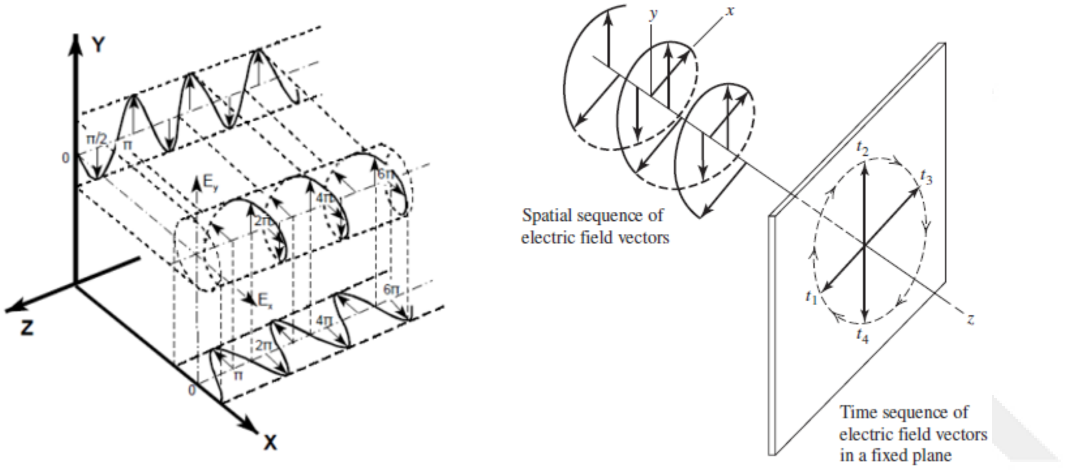

Figure 2.5 : a) Relation Between Sinusoidal wave and Circular Polarized Wave [5]
b) 2D Projection of a Circular Polarized [1]

Another parameter that we mentioned but did not define when describing circular polarization is the axial ratio. We can use Figure 2.6 to define this parameter. Figure 2.6 shows the projection of a wave as in Figure 5b. Figure 2.6 displays the Polarization Pattern, with the Major-Axis and Minor-Axis being designated based on the magnitudes of the E_x and E_y vectors in the image. The axial ratio refers to the proportion of the major and minor axis measurements.

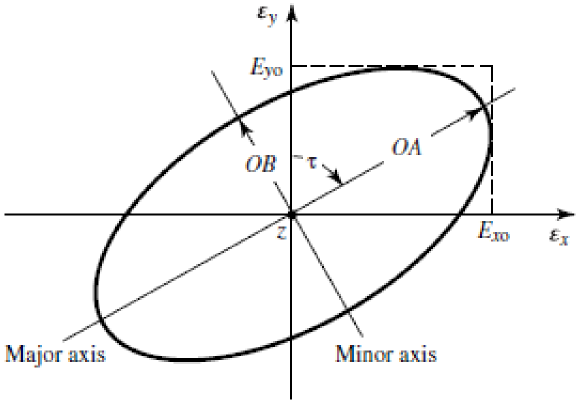

Figure 2.6 : Polarization Pattern for E_x and E_y [4]

Now that we have geometrically defined the Polarization types and axial ratio, we can look at how they are expressed mathematically. First of all, the Electric Field has two different components, E_x and E_y, for all polarization types. In order to express the Electric Field moving in the -Z direction, we can use the following mathematical equation:

$$\mathcal{E}(z;t) = \hat{a}_x \mathcal{E}_x(z;t) + \hat{a}_y \mathcal{E}_y(z;t) \qquad (2.24)$$

Additionally, we can represent the E_x and E_y components using mathematical expressions:

$$\begin{aligned}\mathcal{E}_x(z;t) &= \mathrm{Re}\left[E_x^- e^{j(\omega t+kz)}\right] = \mathrm{Re}\left[E_{xo} e^{j(\omega t+kz+\phi_x)}\right] \\ &= E_{xo}\cos\left(\omega t+kz+\phi_x\right)\end{aligned} \qquad (2.25)$$

$$\begin{aligned}\mathcal{E}_y(z;t) &= \mathrm{Re}\left[E_y e^{j(\omega t+kz)}\right] = \mathrm{Re}\left[E_{yo} e^{j(\omega t+kz+\phi_y)}\right] \\ &= E_{yo}\cos\left(\omega t+kz+\phi_y\right)\end{aligned} \qquad (2.26)$$

The maximum magnitudes of the x and y components are represented by E_{x0} and E_{y0}, respectively.

For a linearly polarized wave, the phase difference should be as follows:

$$\text{For } \Delta\phi = \phi_y - \phi_x = n\pi, n = 0,1,2,3,\ldots$$

$$|\mathcal{E}_x| = |\mathcal{C}_y| \Rightarrow E_{xo} = E_{yo}$$

$$\Delta\phi = \phi_y - \phi_x = \begin{cases} +\left(\dfrac{1}{2} + 2n\right)\pi, n = 0,1,2,\ldots & \text{for CW} \\ -\left(\dfrac{1}{2} + 2n\right)\pi, n = 0,1,2,\ldots & \text{for CCW} \end{cases} \tag{2.27}$$

Clockwise is denoted by CW, while Counter-Clockwise is represented by CCW.

The attainment of circular polarization relies on the equality of the two-component magnitudes and an odd multiple of $\pi/2$ for the time-phased difference, as expressed in Equation 2.27.

In order to achieve elliptical polarization, the time-phase difference between the two components must not be a multiple of $\pi/2$, and the magnitudes must be unequal or in situations where the time-phase discrepancy between the two components is not a multiple of $\pi/2$ and:

$$|\mathcal{E}_x| \neq |\mathcal{E}_y| \Rightarrow E_{xo} \neq E_{yo}$$

$$\text{when } \Delta\phi = \phi_y - \phi_x = \begin{cases} +\left(\frac{1}{2} + 2n\right)\pi & \text{for CW} \\ n = 0,1,2,\ldots & \text{for CCW} \end{cases} \tag{2.28}$$

or

$$\Delta\phi = \phi_y - \phi_x \neq \pm\frac{n}{2}\pi = \begin{cases} > 0 & \text{for CW} \\ < 0 & \text{for CCW} \end{cases} \tag{2.29}$$
$$n = 0,1,2,3,\ldots$$

Meanwhile, we can calculate Axial Ratio (AR) as follows:

$$\mathrm{AR} = \frac{\text{major axis}}{\text{minor axis}} = \frac{OA}{OB}, 1 \leq \mathrm{AR} \leq \infty \tag{2.30}$$

Also, the axial ratio is equal to E_{x0}/E_{y0} or E_{y0}/E_{x0}.

In brief, the polarization of an antenna aligns with the polarization of the emitted wave. In order to comprehend the polarization, the X-Y plane from a stationary point on the axis observed, aligning with the wave's propagation. The Polarization Pattern (Figure 2.6) is then created by projecting the wave's movement over time onto this plane. In understanding polarization, it is essential to consider the interplay of vectors in the X and Y axis of the electric field, as depicted in this pattern. In the same manner, the ratio between the major and minor axes is important in the calculation of the axial ratio, which is a vital parameter in identifying the polarization of the wave. In the light of this information, we can say the following:

For Linear Polarization, the following conditions must be met;

a) Only one component, E_x or E_y, must be existed or;
b) E_x and E_y must have a perpendicular relationship and be either 180° or multiples of 180^0 out of phase in a linear manner.

The conditions listed below must be satisfied in order to achieve Circular Polarization;

a) It is necessary for the E field to possess two linear elements, E_x and E_y, that are perpendicular to each other and
b) The magnitudes of E_x and E_y must be equivalent
c) It is required that the time-phase difference between E_x and E_y is an odd multiple of 90 degrees.

For Elliptical Polarization, the following conditions must be met;

a) The linear E_x and E_y must be orthogonal and
b) E_x and E_y magnitudes can be different or equal
c) When E_x and E_y possess differing magnitudes, it is important to avoid a time-phase difference of 0^0 or any multiple of 180^0 in order to prevent linear polarization.
d) The requirement for E_x and E_y to have identical magnitudes means that the time-phase difference between them cannot be an odd multiple of 90 degrees, as this would lead to circular polarization.

2.3 Microstrip Antenna Design and Models

2.3.1 Introduction

Microstrip antennas have earned an indispensable place in contemporary technologies through a combination of structural features that seamlessly adapt the technology to the demands of modern day-to-day applications. Their importance today is based on a combination of factors that collectively contribute to their widespread adoption in various industries. The compact size and low profile of microstrip antennas are increasingly finding their place in today's technological devices with the increasing emphasis on space efficiency and sleek design.

Furthermore, the unique ability of microstrip antennas to integrate with microwave integrated circuits (MICs) and other planar technologies underscores their importance in communication systems and wireless devices. As the world increasingly relies on the Internet of Things (IoT), the miniaturization possibilities and efficient space utilization provided by microstrip antennas are becoming crucial in the development of compact and high-performance communication modules. Another factor contributing to the continued relevance of microstrip antennas is their ease of manufacture and cost-effectiveness.[1] They offer a practical and cost-effective solution for mass production. Offering an inexpensive and practical solution given the industry's ever-increasing production costs, the seamless integration of microstrip antennas into manufacturing processes ensures that their benefits are not only technological but also economic, rendering them appropriate for a broad spectrum of uses. The wide operating frequency range offered by microstrip antennas greatly diversifies their modern application areas. This allows them to be used in scenarios ranging from satellite communication systems to automotive radar systems, an emerging field that is rapidly advancing. Beyond providing a compact form factor, the planar structure of microstrip antennas is particularly well-suited for phased array configurations. In radar systems, communication networks, and satellite applications, the ability to precisely control the direction of electromagnetic beams is vital. Microstrip antennas are essential for improving the functionality of these systems and fulfilling the requirements for beam steering and directivity [4].

Today, emerging materials and manufacturing techniques are further improving the performance of microstrip antennas. In general, material development activities focus on optimizing dielectric materials and improving manufacturing processes to achieve higher efficiency, higher bandwidth, and optimized radiation characteristics. Another emerging area is the incorporation of superconductors and conductors such as graphene, whose conductivity varies with frequency or temperature, and the ability of applications to adapt to these emerging technologies in this way keeps microstrip antennas at the forefront of innovation, making them essential components in the ever-evolving environment of wireless communications, satellite communications, and radar systems. Ultimately, the combination of compact form factor, integration capabilities, versatility, and adaptability position microstrip antennas as vital contributors to the ongoing transformation of modern technology.

Although the importance of microstrip antennas was understood in the 1970s, their discovery dates back to 1953, and their patent registration dates back to 1955. [1] While circular and rectangular antennas are the most frequently utilized microstrip antennas, there are also other designs available, such as meander structures or half-ring shapes. Some of the traditional antenna shapes preferred in the industry are commonly shown in Figure 2.7. [4]

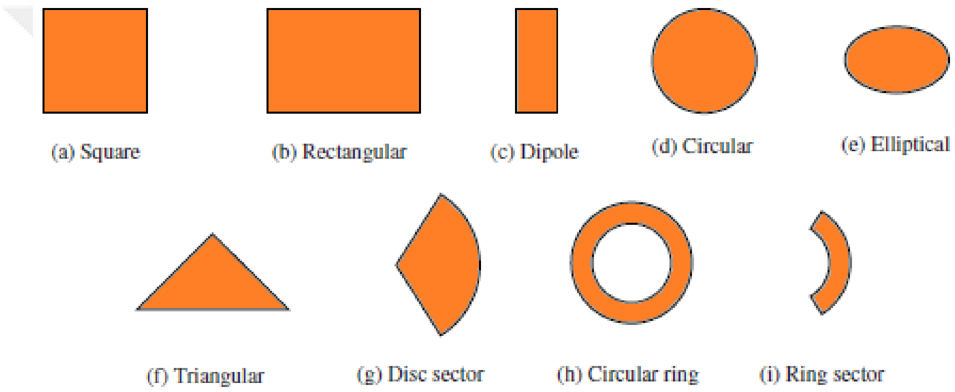

Figure 2.7 : Commonly used patch antenna shapes [4]

2.3.2 Feeding Methods

Before giving more information about microstrip antennas, I think it would be better to explain antenna feeding methods for a better understanding of the subject. In this section, we will explore various antenna feeding techniques and examine their benefits and drawbacks. Antenna feeding refers to the manner in which the antenna is connected to the transmission line.

Microstrip antennas consist of three basic structures. The components of these structures include a resonator patch, ground conductor plates, and a dielectric plate sandwiched between them. According to this explanation, feeding methods can be classified into two primary groups: direct contact methods and non-contact methods.

The antenna resonator and transmission line are directly connected by direct contacting feeding methods, whereas non-contacting methods do not involve this direct connection. The most common direct contacting feeding methods are microstrip line feeding (inset) and probe feeding, whereas non-direct contacting methods are aperture-coupled feeding and proximity-coupled feeding.

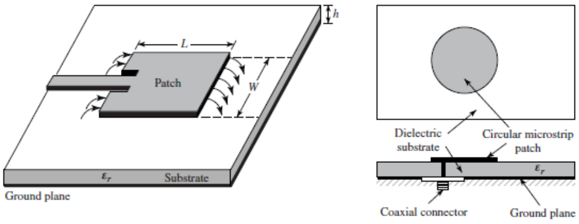

(a) Microstrip line feed (b) Probe feed

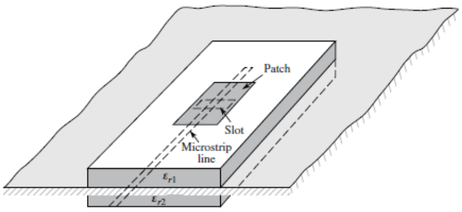

(c) Aperture-coupled feed

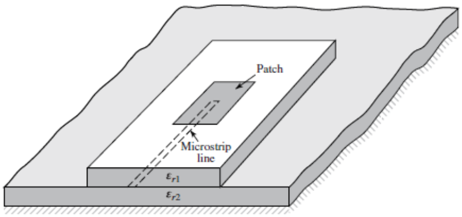

(d) Proximity-coupled feed

Figure 2.8 : Feeding methods of microstrip antenna [4]

Certain limitations, such as the simplicity of the feeding circuit and the isolation between the output circuit and the antenna, play a role in determining the preferred feeding method. Maximize the efficiency of the circuit between the feed and the antenna by adhering to these general guidelines for choosing the ideal excitation type:

- Specify the operational mode for the antenna
- Describes the distribution of the field in the vicinity of the excitation
- Identify excitation field components (E fields and H fields) that contribute effectively to coupling

- Decides on the optimal placement for excitation, allowing for optimal coupling

- Take into account parasitic effects of the supply such as polarization purity distortion, pattern distortion, back radiation, resonant frequency shift, etc

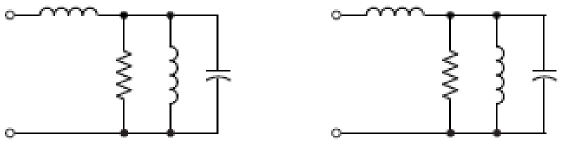

(a) Microstrip line (b) Probe

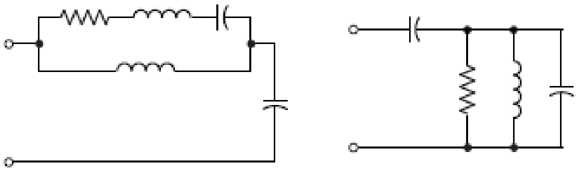

(c) Aperture-coupled (d) Proximity-coupled

Figure 2.9 : Equivalent circuits of Feeding methods [4]

In the Microstrip Line Feed Method, the microstrip feed line, which gives the method its name, is a simple conductive strip. The width of this strip should be considerably smaller than the antenna width. The primary benefit of utilizing this method is its effortless production process. Furthermore, by changing the inset position, input impedance matching becomes easy, and the modeling becomes relatively simple. This model's downside lies in the fact that as the substrate thickness increases, so do surface waves and spur, placing a limitation on the bandwidth available for partial designs (typically between 2-5%). As shown in Figure 2.9a, The RLC tank circuit is used to refer to both the patch antenna and the feed, which is represented by the lone inductor. The impedance at extremely low frequencies is not zero but rather possesses a finite inductance. As the thickness of the substrate grows, so does the inductance of the feed, resulting in a larger offset from the short circuit point. [1]

In the method of probe feeding, a coaxial line serves as the power source, with the inner conductor joined to the radiation patch and the outer connector grounded to the ground plane. Unlike microstrip line feed, probe feed has low spurious radiation and can be more easily matched by manipulating the input resistance with the probe position. One disadvantage of probe feed is its restricted bandwidth and complicated modeling. In comparison to microstrip line feeding, fabrication is a more complex task. As shown in Figure 2.9b, In the context of the RLC tank circuit, the patch antenna is represented by the single inductor, which functions as the feed like a microstrip line. In these cases, the inductance of the feed gets higher when the length of the feed increases. The substrate thickness is restricted for a direct contact-fed patch due to this feed inductance. Beyond about 0.06 λ, achieving a balance in impedance response is challenging, which in turn affects the radiation efficiency. [4]

Non-direct contacting methods have certain benefits than direct contact feeding methods. Higher-order modes are generated by the microstrip line and probe feed asymmetries, causing the emission of cross polarized radiation. Non-contact feeds are implemented as a solution to this problem.

Aperture-coupled feeding has five elements: one radiator patch, one ground plane, and one microstrip feed line as conductors, and one dielectric material (first substrate) between the ground plan and patch also has a second dielectric material (second substrate) between the microstrip feed line and ground plane (representing Figure 2.8c). Commonly, the first substrate has a low dielectric constant, and the second substrate has a high dielectric constant. The patch and feed are isolated by the ground plane, which in turn minimizes the effects of spurious radiation and ensures polarization purity. On the other hand, ground planes have slots, and because of that, back radiation increases. In this structure, to match input impedance, optimize feedline width, slot size, and slot position. When the patch's electric field becomes zero, and the magnetic field reaches its maximum, the slots below are centered. With the aid of magnetic coupling, the control of polarization is highly effective, resulting in no cross-polarized radiation in the principal planes and a wider bandwidth. However, that method is harder to produce than previous methods and harder to simulate.

Proximity-coupled feeding has a similar structure to aperture-coupled feeding, but the main difference is that the ground plane shifted place with the feeding microstrip line shown in Figure 2.8d. The main idea behind this feeding method is the isolation patch and the feed. Also, this method leads to generating capacitive coupling, as shown in Figure 2.9, which allows the thickened substrate, therefore, a much wider bandwidth. In the feed, less parasitic radiation exists. In order to enhance coupling efficiency in this approach, modify the thickness ratio between two substrate layers and align the input impedance by adjusting the length and width of the feeding stub to match the patch ratio. The main advantage of this method is that it offers the largest bandwidth of all these methods and also has low spurious radiation. But it is difficult to simulate and fabricate. Also, alignment is crucial for impedance matching.

2.3.3 Microstrip Antenna Models

Different models are used for antenna analysis. We can be classified into two groups of these methods based on integral or differential equations. Based on differential equations, models are Finite-difference time-domain (FDTD), Finite Element method (FEM), Finite-difference frequency-domain (FDFD), Transmission line model, and Cavity model. In this chapter, we examine the Transmission line model and the Cavity model. Among these models, we have two approximation models and several full-wave analysis models. The simplest of these is the transmission line model, which provides a good understanding of the physical properties but may be less accurate and tricky when demonstrating coupling.

2.3.3.1 Transmission Line Model

In this chapter, we continue to explain the rectangular patch for demonstration. The fringing at the edges of the field is a result of the patch's finite dimensions along its length and width, shown in Figure 2.10a and Figure 2.10b.

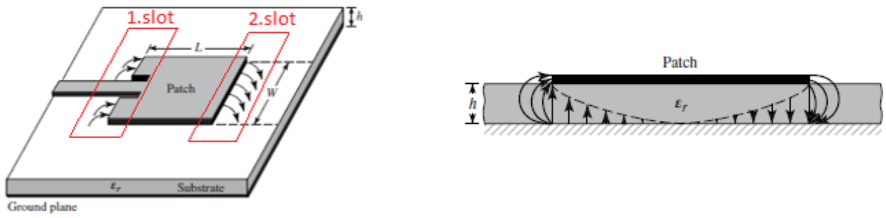

a) Microstrip Antenna

b) Side View

c) Electric Field Lines

d) Effective Dielectric Constant

Figure 2.10 : Fringing Effect on edges (a and b), Electric Field Lines (c), Effective Dielectric Constant (d) [4]

Fringing levels differ depending on the patch size and substrate height. The fringing effect will actually affect the length L for a fringing antenna depending on this mode of operation, as shown in Figure 2.10a, and due to the fringing, the antenna will radiate as if the size of the antenna is greater than the length L and called effective length and explain more detailly later. In the case of the prime E-plane (xy-plane), the extent of fringing is determined by the patch length to substrate height ratio (L/h) and the dielectric constant εr of the substrate. In microstrip patch antennas, the fringing effect is lessened because of the high value of L / h (where L is the patch length and h is the substrate thickness). Nevertheless, it must be acknowledged as it can influence the antenna's resonant frequency. This also holds true for the antenna's width.

The resulting electric field lines pass through the substrate and the medium (let's assume air) in which the antenna is located and reach the ground plane (shown in Figure 2.10c.) There are a variety of paths for electric field lines to reach the ground plane, including some that pass directly through the substrate and others that first travel through the air before reaching their destination. Of course, this generalization depends on the following conditions: When W/ h is considerably larger than 1, and ε_r is greatly higher than 1, the electric field lines will predominantly be concentrated inside the substrate and are appropriate for generalization. Due to the presence of both substrate and airwaves, the effective dielectric constant εreff is introduced to account for scattering and wave movement in the line, simplifying the calculation by combining the two media into one. In this case, the fringing makes the microstrip line appear to have an electrically wider structure compared to its physical dimensions. In this approach, the antenna is considered to be in a substrate with effective dielectric constant ε_{reff} (shown in Figure 2.10d). Within this context, the effective dielectric constant is limited to values between 1 and εr. In the majority of cases where the substrate's dielectric constant is much larger than unity ($\varepsilon_r \gg 1$), ε_{reff} will closely match the true dielectric constant εr of the substrate. Besides, the effective dielectric constant is affected by the operating frequency of the antenna. As the frequency increases, the effective dielectric constant gets closer to the substrate's dielectric constant ε_r. The concentration of electric field lines shifts from the air to the substrate as the frequency increases, making it possible to determine the effective dielectric constant εreff using the following equation;

$$\mathrm{W/h} > 1$$

$$\varepsilon_{\mathrm{reff}} = \frac{\varepsilon_r + 1}{2} + \frac{\varepsilon_r - 1}{2}\left[1 + 12\frac{h}{W}\right]^{-1/2} \tag{2.31}$$

As previously stated, the fringing effect results in the antenna behaving as though it is larger than its actual size. We called the antenna of length L in the example Effective Length L_{eff}, which means that the antenna has a length greater than its actual size due to fringing. The same definition can be made for effective width. In order to determine the effective length, L_{eff}, one must consider both the effective dielectric constant, reff, and the width-to-height ratio (W/h). For determine L_{eff}, we must calculate ΔL, which defines the change in length on both edges due to the fringing effect:

$$\frac{\Delta L}{h} = 0.412\frac{(\varepsilon_{\mathrm{reff}} + 0.3)\left(\frac{W}{h} + 0.264\right)}{(\varepsilon_{\mathrm{reff}} - 0.258)\left(\frac{W}{h} + 0.8\right)} \tag{2.32}$$

the Effective Length L_{eff} will be;

$$L_{\mathrm{eff}} = L + 2\Delta L \tag{2.33}$$

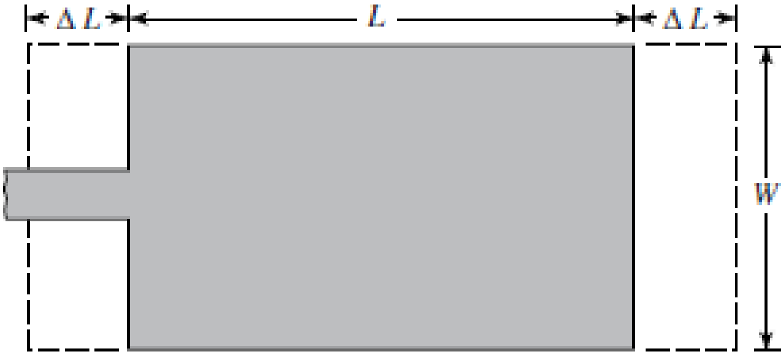

Figure 2.11 : Difference between the Effective and Physical length of the antenna [4]

Also, we can usually calculate the resonant frequency for the dominant TM_{010} mode,

$$(f_r)_{010} = \frac{1}{2L\sqrt{\varepsilon_r}\sqrt{\mu_0\varepsilon_0}} = \frac{v_0}{2L\sqrt{\varepsilon_r}} \tag{2.34}$$

where v_0 is the free-space velocity of light.

But because of the fringing effect, our L actually L_{eff}, so the equation must change;

$$(f_{rc})_{010} = \frac{1}{2L_{\text{eff}}\sqrt{\varepsilon_{\text{reff}}}\sqrt{\mu_0\varepsilon_0}} = \frac{1}{2(L+2\Delta L)\sqrt{\varepsilon_{\text{reff}}}\sqrt{\mu_0\varepsilon_0}} \tag{2.35}$$

And the ratio of these two frequencies gives us the Fringe Factor or Length Reduction Factor (q):

$$q = \frac{(f_{rc})_{010}}{(f_r)_{010}} \tag{2.36}$$

To summarize, as the substrate increases in height, the fringing also increases and causes the antenna dimensions to behave as if they are larger, lowering the resonant frequency. Based on the fringing, the antenna size appears longer, as shown in Figure 2.11. Fringing can lead to a 2-6% decrease in resonant frequency. [4]

With a solid understanding of how the antenna is generally modeled and the methods used in the transmission line model, we can now turn to explain how this model is utilized to determine the physical characteristics of the antenna. For this, we first need to determine 3 parameters: The resonant frequency (f_r) to be selected depending on the application area of the antenna, the substrate to be used and the dielectric coefficient (ε_r) it, and the height of substrate (h) which is thicknesses of the antenna. In short, it is important to determine the resonant frequency (f_r), the dielectric constant of the substrate (ε_r), and substrate height (h). [4]

The calculation of the Length and Width of the rectangular antenna requires knowledge of the resonant frequency (f_r), the dielectric constant of the substrate (ε_r), and the height of the substrate (h);

$$W = \frac{1}{2f_r\sqrt{\mu_0\varepsilon_0}}\sqrt{\frac{2}{\varepsilon_r+1}} = \frac{v_0}{2f_r}\sqrt{\frac{2}{\varepsilon_r+1}} \tag{2.37}$$

.

$$\mathrm{L} = \frac{1}{2\mathrm{f_r}\sqrt{\varepsilon_{\mathrm{reff}}}\sqrt{\mu_0\varepsilon_0}} - 2\Delta\mathrm{L} \tag{2.38}$$

It is also possible to calculate the conductance of the antenna within the model. In the beginning, we assumed that the antenna radiates through two slots, as shown in Figure 2.12. [4]

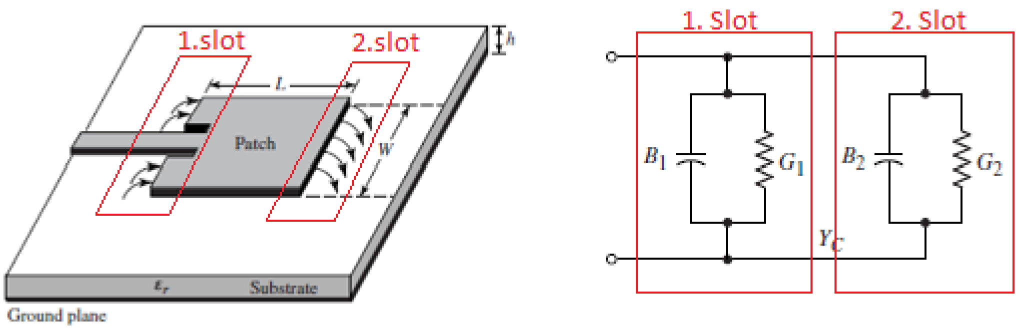

Figure 2.12 : Radiating Slots and Circuit Equivalents [4]

Accordingly, the circuit diagram of these two slots can be modeled as follows:

$$Y_1 = G_1 + jB_1 \tag{2.39}$$

Y_1 represent admittance and G_1 is conductance and B_1 is susceptance of Slot 1

And for the antenna has finite width W;

$$\begin{aligned} G_1 &= \frac{W}{120\lambda_0}\left[1 - \frac{1}{24}(k_0h)^2\right] \qquad \frac{h}{\lambda_0} < \frac{1}{10} \\ B_1 &= \frac{W}{120\lambda_0}\left[1 - 0.636\ln(k_0h)\right] \frac{h}{\lambda_0} < \frac{1}{10} \end{aligned} \tag{2.40}$$

Since Slot 1 and Slot 2 are identical;

$$Y_2 = Y_1, G_2 = G_1, B_2 = B_1 \tag{2.41}$$

G1 also expressed as;

$$G_1 = \frac{2P_{\text{rad}}}{|V_0|^2} \tag{2.42}$$

Therefore, asymptotic values of the conductance can be expressed as:

$$G_1 = \begin{cases} \frac{1}{90}\left(\frac{W}{\lambda_0}\right)^2 & W \ll \lambda_0 \\ \frac{1}{120}\left(\frac{W}{\lambda_0}\right) & W \gg \lambda_0 \end{cases} \tag{2.43}$$

Taking advantage of the fact that these two radiating slots are identical, we can write the following:

$$\tilde{Y}_2 = \tilde{G}_2 + j\tilde{B}_2 = G_1 - jB_1 \quad \text{and} \quad \begin{aligned} \tilde{G}_2 &= G_1 \\ \tilde{B}_2 &= -B_1 \end{aligned} \tag{2.44}$$

Hence, the overall resonant input admittance is purely real and can be computed as;

$$Y_{in} = Y_1 + \tilde{Y}_2 = 2G_1 \tag{2.45}$$

And input admittance will be real so that input impedance is also real:

$$Z_{in} = \frac{1}{Y_{in}} = R_{in} = \frac{1}{2G_1} \tag{2.46}$$

Also, input resistance can be affected by mutual effects between two slots so that our equation will be:

$$R_{in} = \frac{\mathbf{1}}{\mathbf{2}(\boldsymbol{G_1} \pm \boldsymbol{G_{12}})} \tag{2.47}$$

And G_{12} can be defined as:

$$G_{12} = \frac{1}{|V_0|^2} \mathrm{Re} \iint_S \mathrm{E}_1 \times \mathrm{H}_2^* \cdot ds \tag{2.48}$$

The measurement and calculation may pose challenges, so we can utilize an alternative approximation to find the input impedance of a rectangular patch:

$$R_{in} = 90 \frac{(\varepsilon_r)^2}{\varepsilon_r - 1}\left(\frac{L}{W}\right) \tag{2.49}$$

2.3.3.2 Cavity Model

The cavity model offers a framework for understanding the fields in the antenna and the propagating fields. It was developed in the late 1970s. In this model, the antenna resembles a dielectric-loaded cavity and gives rise to high-order resonances. [1]

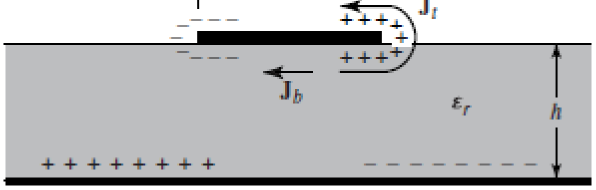

Figure 2.13 : Charge distribution and densities on the surfaces of the patch antenna [4]

One of the key benefits of this model is its ability to accurately depict the normalized fields between the patch and ground plane, unlike the transmission line model. This process takes into account certain assumptions, which are listed as follows: the antenna is defined as a cavity bordered by patch and ground conductors at the top and bottom and a magnetic wall at the periphery. The fundamental idea behind this model is an approximation that generates a reactive input impedance (zero or infinite resonance value) and does not emit power. [4]

As the antenna begins to operate and receive energy, it initiates a charge distribution on both the patch and ground conductor surfaces at the top and bottom, as shown in Figure 2.13. There are two factors at play in controlling the distribution of charge: an attractive and a repulsive mechanism. The repulsive mechanism is triggered by the presence of identical charges on the bottom surface of the patch, resulting in a push toward the patch's edge and top surface. The bottom and top surfaces of the patch experience current densities of J_b and J_t, respectively, as a result of the charges in this motion shown in Figure 2.13. In general, microstrip antennas have a low height-to-width ratio, causing the attractive mechanism to have a strong influence. As a result, the bottom surface of the patch experiences the most current flow and charge concentration. The patch's top surface receives a small current flow from its edges. Nonetheless, this current decreases as the ratio of height to width decreases. If the current flow towards the top is non-existent, there will be no tangential magnetic field created at the edges of the patch. By functioning as perfect magnetic conductors, the four side walls will not disrupt the magnetic field and will maintain the electric field distribution underneath the patch. The performance of this show results in exceptional electric and magnetic field modes beneath the patch. For a better understanding of the calculation of the normalized magnetic and electric field modes underneath the patch, we must understand equivalent current densities.

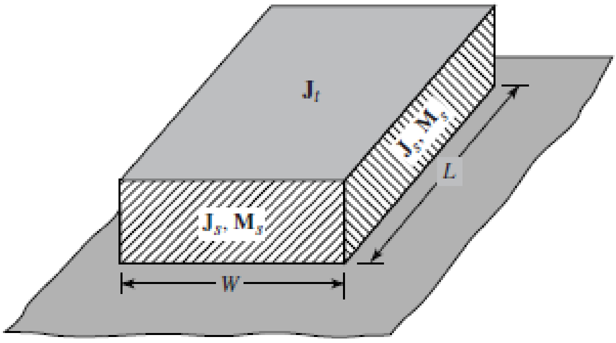

(a) J_s, M_s with ground plane

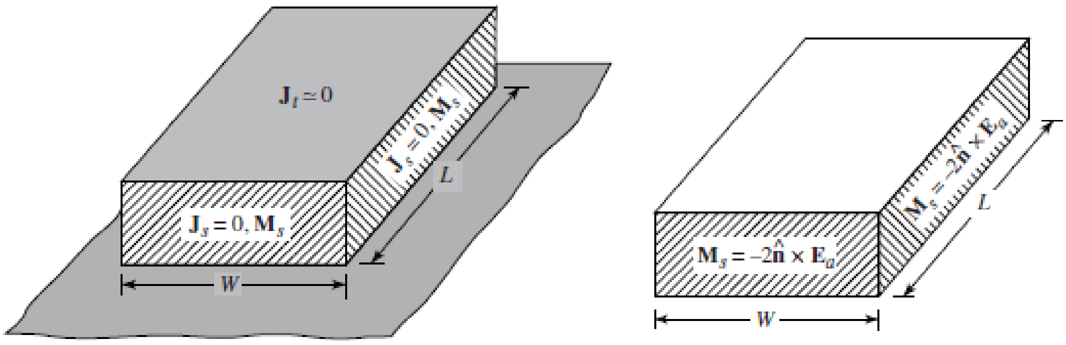

(b) $J_s = 0$, M_s with ground plane

(c) M_s with no ground plane

Figure 2.14 : Equivalent current densities on four edges of rectangular microstrip patch [4]

Radiation is transmitted through four narrow slits, which are depicted as the four side walls. Using the field equivalence principle, for the purpose of this model, the microstrip patch is simplified to an equivalent current density Jt on its top surface, accounting for its impact. (Please note that there is also a current density Jb present on the bottom surface, but it is not required in this model.) The four side gaps are denoted as J_s and M_s, signifying equivalent current and magnetic current (represented in Figure 2.14a), can be calculated as follows:

$$J_s = \hat{n} \times H_a \tag{2.50}$$

$$M_s = -\hat{n} \times E_a \tag{2.51}$$

$\hat{n}$ represents direction vector.

As stated before, microstrip antennas typically have a small height-to-width ratio. The current density on the top surface of the patch is much less than the current density on the bottom side of the patch. So, we can accept the current density on the bottom side is equal to zero, as shown in Figure 2.14b. Furthermore, the tangential magnetic fields at the edges of the patch are minute, as discussed in detail earlier, and can be postulated to be zero. The only remaining part not equal to zero is the equivalent magnetic current density Ms on the edges shown in 2.14b. Therefore, the final equivalent of the magnetic current density will be shown in Figure 2.14c:

$$\mathrm{M}_s = -2\hat{\mathrm{n}} \times E_a \tag{2.52}$$

The cavity model exhibits a very small height-to-width ratio for the antenna, the fringing effect is virtually eliminated, and the current density on the top surface of the patch is extremely low, permitting the fields to only travel in the region between the patch and the ground. Due to the substrate's small height compared to the wavelength, the waves within this cavity are believed to be constant. It is, therefore, possible to observe only TM modes in the cavity model.

The vector potential A_x must satisfy the homogeneous wave equation when utilizing the vector potential approach.;

$$\nabla^2 A_x + k^2 A_x = 0 \tag{2.53}$$

Also, can be written by using the separation of variables:

$$\begin{aligned} A_x = {} & [A_1 \cos(k_x x) + B_1 \sin(k_x x)]\left[A_2 \cos\left(k_y y\right) + B_2 \sin\left(k_y y\right)\right] \\ & \cdot [A_3 \cos(k_z z) + B_3 \sin(k_z z)] \end{aligned} \tag{2.54}$$

In regards to the wavenumbers k_x, k_y, and k_z in the x, y, and z directions, respectively, and the constants A_1, A_2, A_3, B_1, B_2, and B_3, the electric and magnetic fields within the cavity are dependent on the vector potential A_x.:

$$\begin{aligned} E_x &= -j\frac{1}{\omega\mu\varepsilon}\left(\frac{\partial^2}{\partial x^2} + k^2\right)A_x & H_x &= 0 \\ E_y &= -j\frac{1}{\omega\mu\varepsilon}\frac{\partial^2 A_x}{\partial x\,\partial y} & H_y &= \frac{1}{\mu}\frac{\partial A_x}{\partial z} \\ E_z &= -j\frac{1}{\omega\mu\varepsilon}\frac{\partial^2 A_x}{\partial x\,\partial z} & H_z &= -\frac{1}{\mu}\frac{\partial A_x}{\partial y} \end{aligned} \tag{2.55}$$

For the boundary conditions of:

$$\begin{aligned} &E_y(x'= 0{,}0 \le y' \le L, 0 \le z' \le W) \\ &\qquad = E_y(x' = h, 0 \le y' \le L, 0 \le z' \le W) = 0 \\ &H_y(0\le x' \le h, 0 \le y' \le L, z' = 0) \\ &\qquad = H_y(0 \le x' \le h, 0 \le y' \le L, z' = W) = 0 \\ &H_z(0\le x' \le h, y' = 0{,}0 \le z' \le W) \\ &\qquad = H_z(0 \le x' \le h, y' = L, 0 \le z' \le W) = 0 \end{aligned}$$

The primed coordinates x′, y′, z′ are used to shown the fields inside the boundary in the cavity.

From the first boundary condition Ey (x′ = 0, 0 ≤ y′ ≤ L, 0 ≤ z′ ≤ W) = 0 and Ey (x′ = h, 0 ≤ y′ ≤ L, 0 ≤ z′ ≤ W) = 0, result of that B1=0 and;

$$k_x = \frac{m\pi}{h}, m = 0{,}1{,}2, \ldots \qquad (2.56)$$

From the second boundary condition H_y (0 ≤ x′ ≤ h, 0 ≤ y′ ≤ L, z′ = 0) = 0 and H_y (0 ≤ x′ ≤ h, 0 ≤ y′ ≤ L, z′ = W) = 0, result of that B_3 = 0 and:

$$_z = \frac{p\pi}{W}, p = 0{,}1{,}2, \ldots$$

(2.57)

From the third boundary condition H_z (0 ≤ x′ ≤ h, y′ = 0, 0 ≤ z′ ≤ W) = 0 and H_z (0 ≤ x′ ≤ h, y′ = L, 0 ≤ z′ ≤ W) = 0, result of that B_2 = 0 and;

$$k_y = \frac{n\pi}{L}, n = 0{,}1{,}2, \ldots \qquad (2.58)$$

Because of that, we can write the equation of vector potential A_x within cavity:

$$A_x = A_{\mathrm{mnp}} \cos\,(k_x x')\cos\,(k_y y')\cos\,(k_z z') \qquad (2.59)$$

Amnp represents the values for the amplitude coefficients of each mnp mode. The wavenumbers k_x, k_y, and k_z are equivalent to.;

$$\left.\begin{aligned} k_x &= \left(\frac{m\pi}{h}\right), \quad m = 0{,}1{,}2, \ldots \\ k_y &= \left(\frac{n\pi}{L}\right), \quad n = 0{,}1{,}2, \ldots \\ k_z &= \left(\frac{p\pi}{W}\right), \quad p = 0{,}1{,}2, \ldots \end{aligned}\right\} m = n = p \neq 0 \qquad (2.60)$$

The number of half-cycle field variations in the x, y, and z directions are represented by m, n, and p, respectively. The constraint equation also applies to the wavenumbers k_x, k_y, and k_z;

$$k_x^2 + k_y^2 + k_z^2 = \left(\frac{m\pi}{h}\right)^2 + \left(\frac{n\pi}{L}\right)^2 + \left(\frac{p\pi}{W}\right)^2 = k_r^2 = \omega_r^2 \mu\varepsilon \tag{2.61}$$

So, we can calculate resonant frequency in the cavity model as follows;

$$(f_r)_{mnp} = \frac{1}{2\pi\sqrt{\mu\varepsilon}}\sqrt{\left(\frac{m\pi}{h}\right)^2 + \left(\frac{n\pi}{L}\right)^2 + \left(\frac{p\pi}{W}\right)^2} \tag{2.62}$$

We can calculate E fields and H fields in the cavity model as;

$$\begin{aligned}
E_x &= -j\frac{(k^2-k_x^2)}{\omega\mu\varepsilon}A_{mnp}\cos(k_x x')\cos(k_y y')\cos(k_z z') \\
E_y &= -j\frac{k_x k_y}{\omega\mu\varepsilon}A_{mnp}\sin(k_x x')\sin(k_y y')\cos(k_z z') \\
E_z &= -j\frac{k_x k_z}{\omega\mu\varepsilon}A_{mnp}\sin(k_x x')\cos(k_y y')\sin(k_z z') \\
H_x &= 0 \\
H_y &= -\frac{k_z}{\mu}A_{mnp}\cos(k_x x')\cos(k_y y')\sin(k_z z') \\
H_z &= \frac{k_y}{\mu}A_{mnp}\cos(k_x x')\sin(k_y y')\cos(k_z z')
\end{aligned} \tag{2.63}$$

Using these equations. For all microstrip patch antennas, $h \ll L$ and $h \ll W$.

The TM_{010} is the dominant mode with the lowest frequency when L is larger than both W and h, and its resonant frequency is;

$$(f_r)_{010} = \frac{1}{2L\sqrt{\mu\varepsilon}} = \frac{v_0}{2L\sqrt{\varepsilon_r}} \tag{2.64}$$

The TM_{020} mode will be the dominant mode for $L > L/2 > W > h$, rather than the expected TM_{001} mode, and its resonant frequency can be calculated by;

$$(f_r)_{020} = \frac{1}{L\sqrt{\mu\varepsilon}} = \frac{v_0}{L\sqrt{\varepsilon_r}} \tag{2.65}$$

All these expressed TM modes are shown in Figure 2.15.

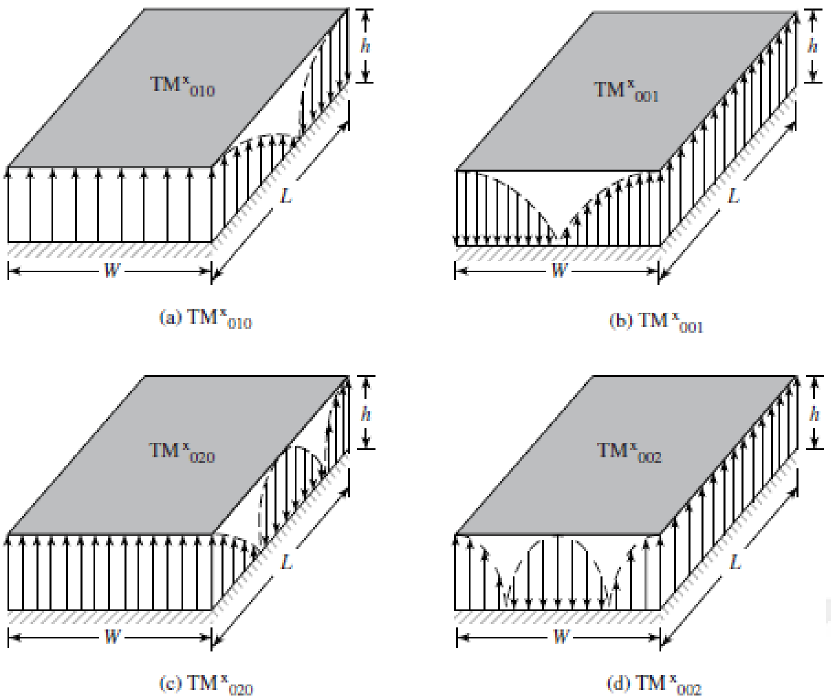

(a) TM$^x_{010}$ (b) TM$^x_{001}$

(c) TM$^x_{020}$ (d) TM$^x_{002}$

Figure 2.15 : Field modes for rectangular microstrip patch [4]

The TM$_{010}$ mode reigns supreme within the cavity, with the electric and magnetic field components exhibited as.;

$$
\begin{aligned}
E_x &= E_0 \cos\left(\frac{\pi}{L} y'\right) \\
H_z &= H_0 \sin\left(\frac{\pi}{L} y'\right) \\
E_y &= E_z = H_x = H_y = 0
\end{aligned}
\tag{2.66}
$$

Where $E_0 = -j\omega A_{010}$ and $H_0 = (\pi/\mu L)A_{010}$. Figure 2.16 shows the field lines for 4 radiating slots on the edges of the patch in the cavity model.

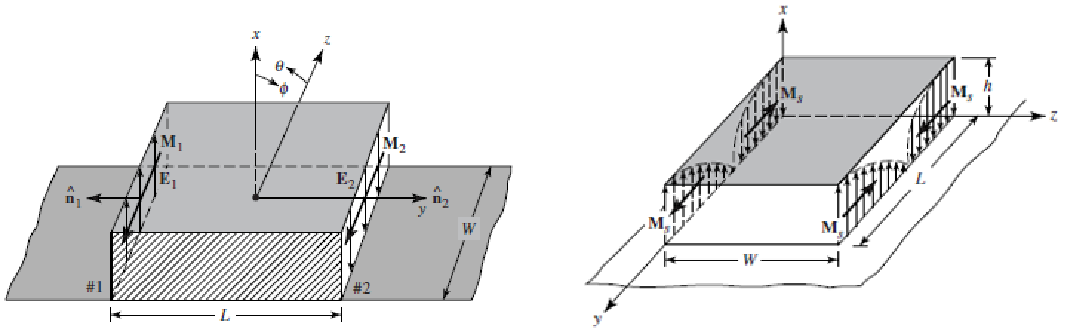

Figure 2.16 : a) Current densities on radiating slots of microstrip patch
b) Current densities on non-radiating slots of microstrip patch [4]

For the non-radiating slots, M_s cancels each other due to going towards opposite directions so that the E field and H fields of TM_{010} mode are shown Figure 2.17;

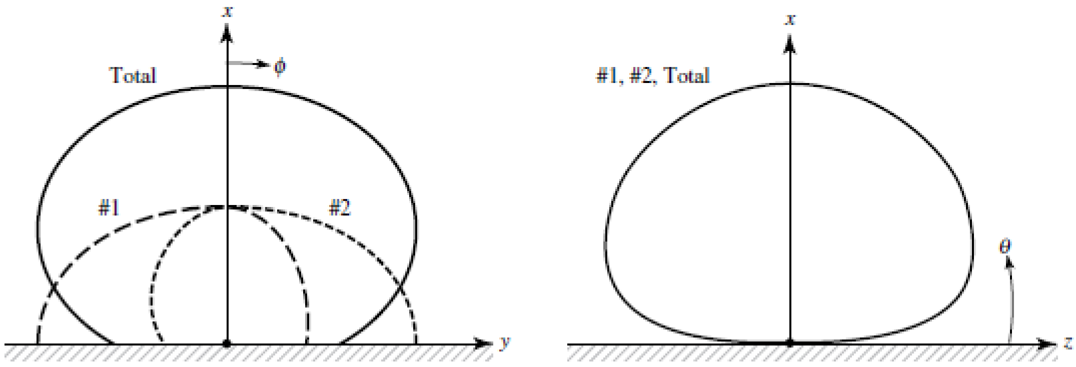

(a) *E*-plane

(b) *H*-plane

Figure 2.17 : Typical E- and H-plane patterns of each rectangular microstrip patch slot and of the two together [4]

3. PROPERTIES OF GRAPHENE

Graphene, a kind of carbon allotrope, is perhaps one of the most interesting materials to have emerged in recent years due to its unique properties. [6] Currently recognized as the thinnest elastic material in the world, graphene has also been widely acclaimed for its unique electrical, mechanical, optical, and thermal properties. [7-13] At room temperature, graphene's carrier mobility can be as high as 200,000 cm2/Vs [8], and its resistivity is as low as 30Ω/m. In addition, graphene has an intrinsic strength of 130 GPa, Young's modulus of 1 TPa, a tremendous thermal conductivity of about 3,000WmK, and complete impermeability to any gas, as well as an optical absorption of exactly pa<2.3%. Thanks to all these characteristics, graphene has significant potential for many applications, such as high-speed transistors, battery production technologies, transparent conductive films, high-frequency antennas, and many more. [11] In addition, the fact that carbon is one of the most common elements in nature and on our planet is very advantageous for graphene, considering the limited reserves of other materials. Professor Sir Andre Geim and Professor Kostya Novoselov, [7] faculty members at the University of Manchester, achieved the groundbreaking feat of isolating a single atomic layer of carbon in 2004. The micromechanical splitting technique, commonly referred to as the 'Scotch tape method', is employed. The swift growth of this field of science can be attributed to its simplicity and effectiveness, which has led to the participation of hundreds of laboratories worldwide in different aspects of graphene research.

Graphene is the name given to a two-dimensional (2D) structure that is as thick as a single carbon atom arranged hexagonally like a honeycomb lattice. [6] All graphene-based materials (graphitic materials) are obtained by stacking this two-dimensional structure on top of each other. Figure 3.1 shows the orbital structure formed by the carbon atoms coming together while being connected to each other in a honeycomb shape. The formation of three sp^2 hybrid orbitals in this structure can be attributed to the combination of the *2s* orbital of carbon with the *2px* and *2py* orbitals. When carbon atoms bond together, they produce the most robust type of covalent bonds, referred to as σ-bonds. The horizontal plane σ-bonds between carbon atoms are responsible for imparting strength, robustness, flexibility, and other electrical properties to graphene and carbon nanotubes (CNTs). *2pz* electrons form a weak covalent bond called π-bonds, which are normally distributed in the plane connecting the carbon atoms. In other words, the electrons in the π-bonds normally distributed in this plane can be displaced within the structure due to the weak bond. Graphene's electronic properties are influenced by π-bonds.[14]

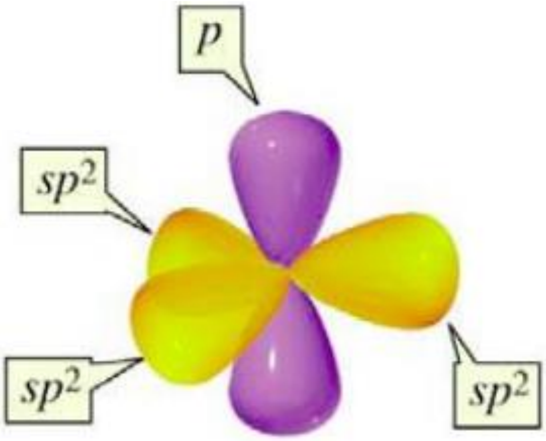

Figure 3.1 : Illustration of Orbitals of a single atom in the graphene structure [2]

Graphene can be considered infinitely large 2-dimensional single-layer carbon with an infinitesimal thickness of a single atom. Within the graphene structure, the carbon atoms are found in a *sp*^{2} hybrid state, with a 120° distance between each orbital. Three neighboring atoms are symmetrically arranged, with each carbon atom forming a lattice named Bravais Lattice, as shown in Figure 3.2. [15]

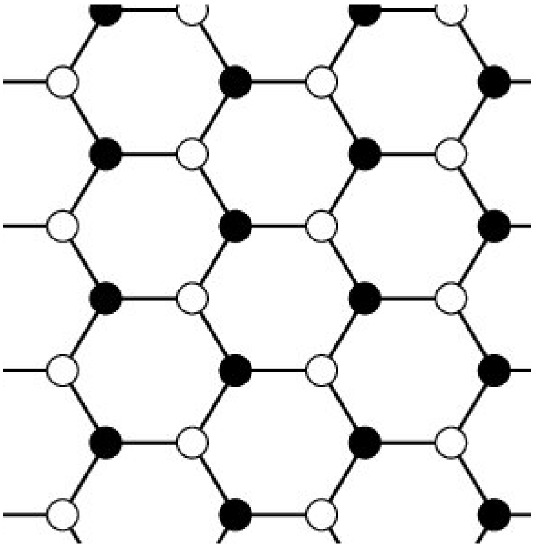

Figure 3.2 : The honeycomb lattice structure of graphene [2]

Traditional Microstrip Patch antenna designs usually consist of a patch made of copper. Due to its unique electrical properties, graphene is one of the most important materials that we believe could replace copper. Graphene is considered to be a suitable material to operate in the terahertz regime, especially in next-generation nano communication systems. Graphene has exceptional properties for the propagation of surface polarizations. An SPP (surface plasmon polariton) is the result of an electromagnetic wave interacting with a plasmon, a charge wave located at the interface of metal and dielectric materials. The wave's transverse E component must be directed parallel to the surface (TM-polarized). The oscillation of both photons and dipoles in a medium is referred to as polarization.

3.1 Graphene Conductivity

The principles of Maxwell's equations dictate the behavior of electromagnetic fields in metallic conductors. Nevertheless, our particular situation calls for a unique approach due to the involvement of graphene. The semi-classical intra-band mode and quantum-dynamical inter-band mode are responsible for the surface conductivity of graphene. The Kubo formulas were employed by Falkovsky et al. and Hanson et al. to compute the surface conductivity of a graphene film with infinitesimal dimensions in their research. [16] The surface conductivity can be represented in a local form through the application of the random-phase approximation, similar to the Drude-like contribution. So, we can calculate the conductivity of graphene by using Kubo Formula;

$$\sigma_g(\omega, \mu_c, \Gamma, T) = \sigma^{\gamma} + \mathrm{j}\sigma'' = \sigma_{\mathrm{intra}} + \sigma_{\mathrm{inter}} \tag{3.1}$$

$$\begin{aligned}\sigma_g = \frac{jq^2}{\pi\hbar(\omega - j2\Gamma)} \int_0^{\infty} \varepsilon \left[\frac{\partial f_d(\varepsilon)}{\partial \varepsilon} - \frac{\partial f_d(-\varepsilon)}{\partial \varepsilon}\right] d\varepsilon \\ - \frac{jq^2(\omega - j2\Gamma)}{\pi\hbar^2} \int_0^{\infty} \frac{f_d(-\varepsilon) - f_d(\varepsilon)}{(\omega - j2\Gamma)^2 - 4(\varepsilon/\hbar)^2} d\varepsilon\end{aligned} \tag{3.2}$$

And

$$Fd(\mathcal{E}) = \frac{1}{1 + e^{\frac{\mathcal{E} - \mu_c}{k_B T}}} \tag{3.3}$$

is the Fermi-Dirac distribution, where ε_r is the relative permittivity of the substrate the graphene is created with, and where vF ≈ 9.5×10^5m/s is the Fermi speed of graphene. [17] .Also, μc is the chemical potential of graphene and can be calculated as;

$$\mu_c \approx \hbar v_F \sqrt{\frac{\pi C_{ox} V_{\mathrm{DC}}}{e}} \tag{3.4}$$

Where C_{ox} is the gate capacitance;

$$C_{\mathrm{ox}} = \varepsilon_r \varepsilon_0 / t \tag{3.5}$$

Where ω is the angular frequency, μ_c denotes the chemical potential, Γ= 1/(2τ) is the scattering rate, τ is the relaxation time, T is the temperature, −q is the charge of an electron, ħ= h/2π denotes the reduced Planck's constant, kB denotes the Boltzmann's constant and t donates thickness of the graphene.

The intra-band contribution can be computed as;

$$\sigma_{\mathrm{intra}} = -\frac{jq^2 k_B T}{\pi \hbar^2 (\omega - j2\Gamma)} \left[\frac{\mu_c}{k_B T} + 2\ln\left(e^{-\mu_c/k_B T} + 1\right)\right] \tag{3.6}$$

The inter-band contribution can be calculated as;

$$\sigma_{\mathrm{inter}} = -\frac{jq^2}{4\pi\hbar} \ln\left[\frac{2|\mu_c| - (\omega - j2\Gamma)\hbar}{2|\mu_c| + (\omega - j2\Gamma)\hbar}\right] \tag{3.7}$$

For $k_B T \ll |\mu_c|, \hbar\omega$

The model used for this formulation simplifies graphene conductivity and does not account for magnetic hall conductivity. It assumes that graphene is solely influenced by electrical bias. [18] Also, Graphene's chemical potential manipulated by external bias V_{dc}. Because of that we can change electrical properties of the Graphene with applying different external voltages. [63] Figure 3.3 shows the conductivity changes with the change of chemical potential due to external bias voltage. Also, intra-band is dominant on the Terahertz Spectrum. [19]

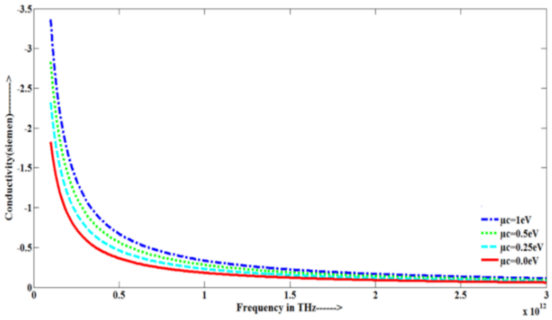

a) Real part of the intra-band conductivity of the graphene

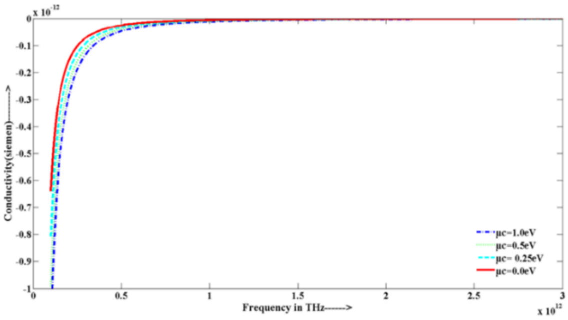

b) Imaginary part of the intra-band conductivity of the graphene

Figure 3.3 : Real & Imaginary Parts of the Intra-band Conductivity of Graphene [2]

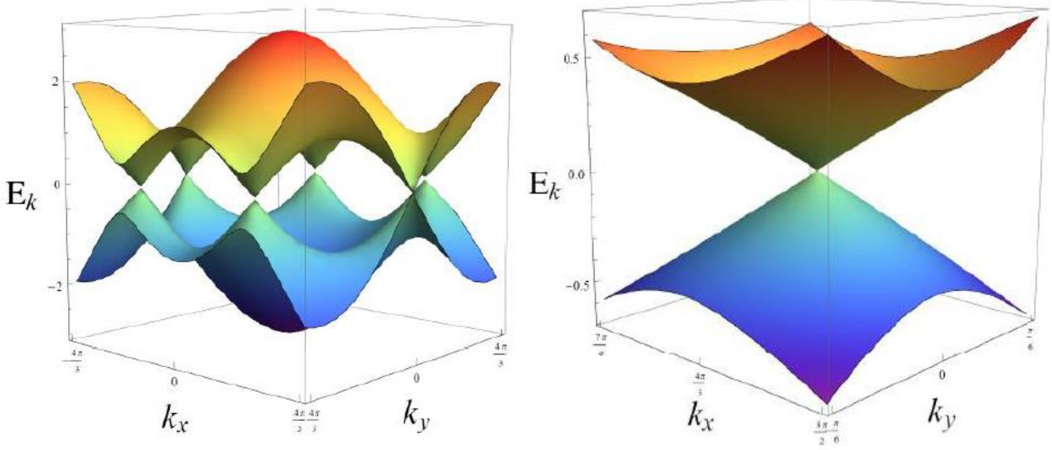

Figure 3.4 : Graphene Energy - Momentum Diagram [15,20]

Another factor affecting the change in the conductivity of graphene depending on its chemical potential, as described above, is the unique energy-momentum diagram of graphene. The electrons on graphene behave like particles of light (photons), and therefore, the energy-momentum diagram is not parabolic like conventional semiconductors but consists of linearly intersecting lines. Accordingly, depending on the chemical potential change, the intersection point (Dirac point) in this energy-momentum diagram changes, changing the conductivity of the material. [15,20] The conductivity of graphene, expressed mathematically above, is actually due to this structural feature.

3.2 Graphene Antenna Designs

The [21] is a Yagi-Uda antenna designed for medical applications, such as the detection of skin and liver cancers. It works between 2.35-2.7 THz and uses graphene to eliminate the disadvantages of microstrip antennas (low gain and low efficiency). The antenna confidently employs silicon dioxide as the substrate, incorporating parasitic graphene rectangular patches on both sides to enhance directivity effectively. The dimensions of the parasitic elements are precisely adjusted logarithmically to ensure optimal performance. Using the characteristics of graphene to change conductivity by chemical potential, the antenna has a reconfigurable working frequency for different chemical voltages of the graphene. The maximum simulated gain of the antenna is 9 dB, much higher than similar copper antennas. [21]

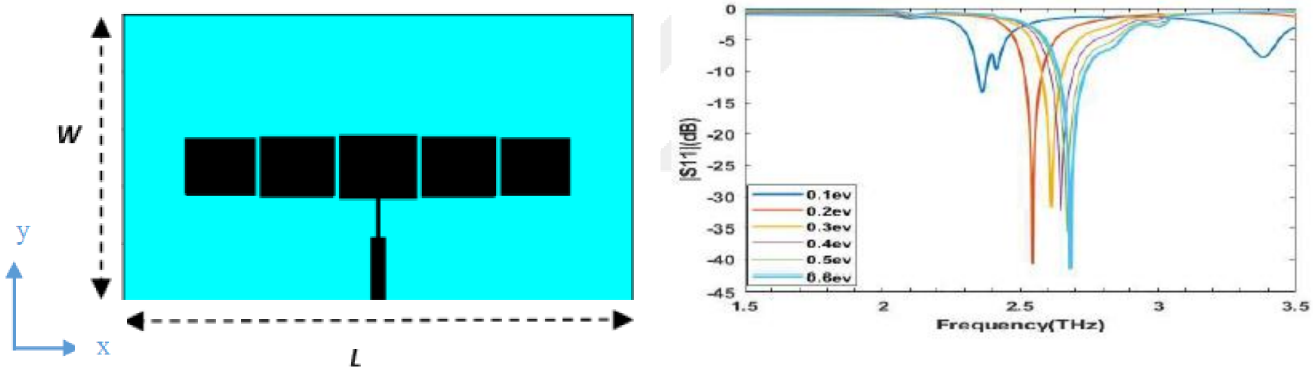

Figure 3.5 : Yagi-Uda Antenna Top view on the right and S_{11} Parameters for different chemical potentials on the left [21]

In [22], a copper antenna design for the 0.7 THz can be used for aerial applications. As a reference antenna, it has a maximum gain of 7.11 dB. Graphene is preferred for the suggested antenna structure because of adjustable surface conductivity. With using that antenna, the operating frequency can be changed between 0.65 THz and 0.8 THz, and the peak value of S_{11} is -29 dB for antenna works at 0.7 THz and 0.76 eV applied on graphene.

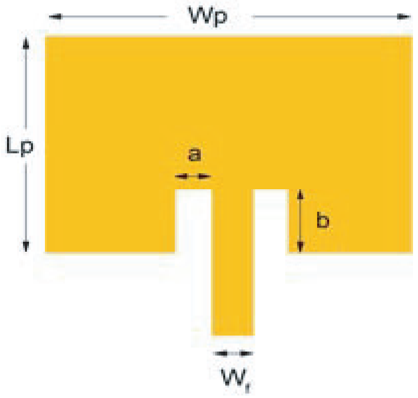

Figure 3.6 : Graphene-based reconfigurable patch antenna top view [22]

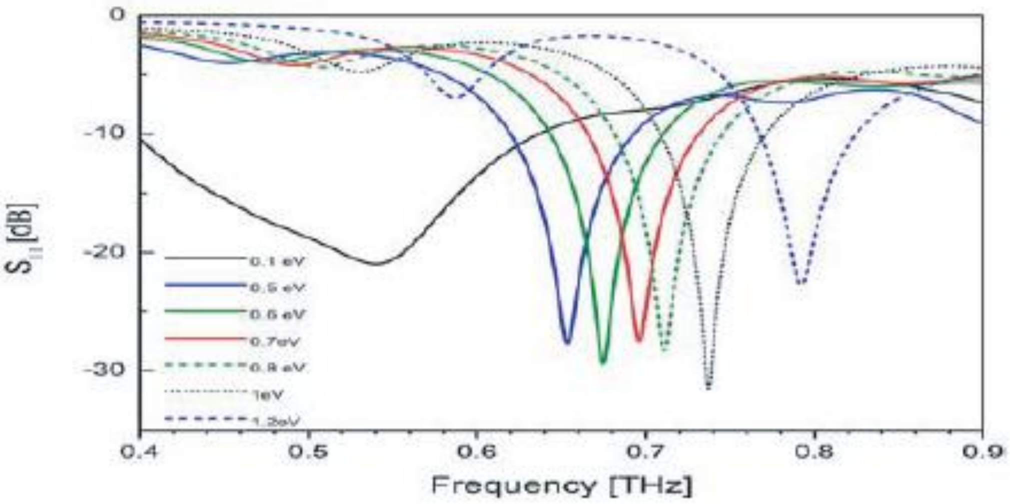

Figure 3.7 : S_{11} Parameters for different chemical potentials [22]

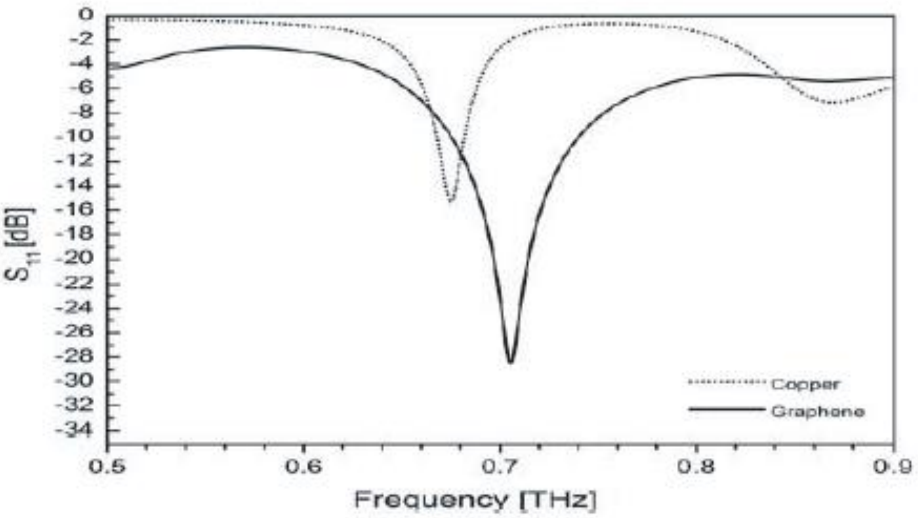

Figure 3.8 : Comparison between Grahepene and Copper patch antenna [22]

By using graphene as a replacement for copper, the gain of the antenna decreased from 5.63 dB to 7.11 dB. also, antenna frequency can be changed by applying a chemical potential to the graphene surface.

Graphene can be used to change the antenna radiation pattern in the temperature. [23] The antenna operates at 2.29 THz and has a peak gain of 8.19 dB.

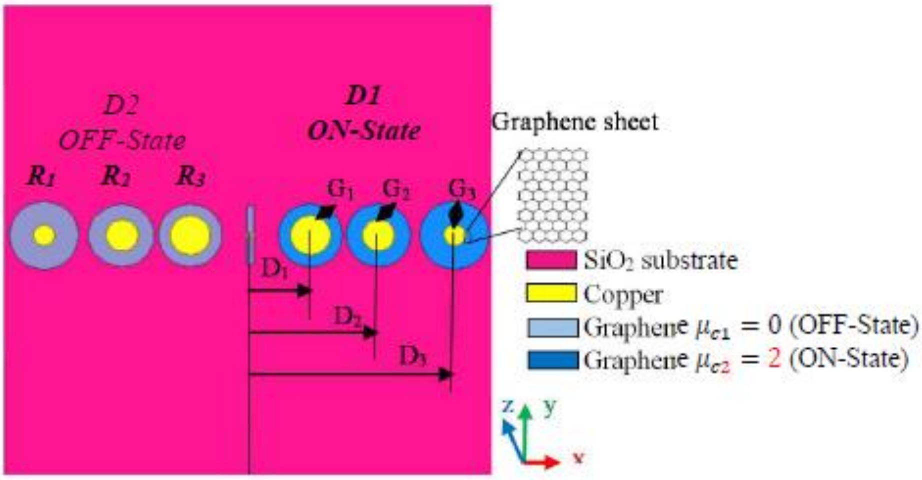

Figure 3.9 : Yagi-Uda Antenna Working Principle [23]

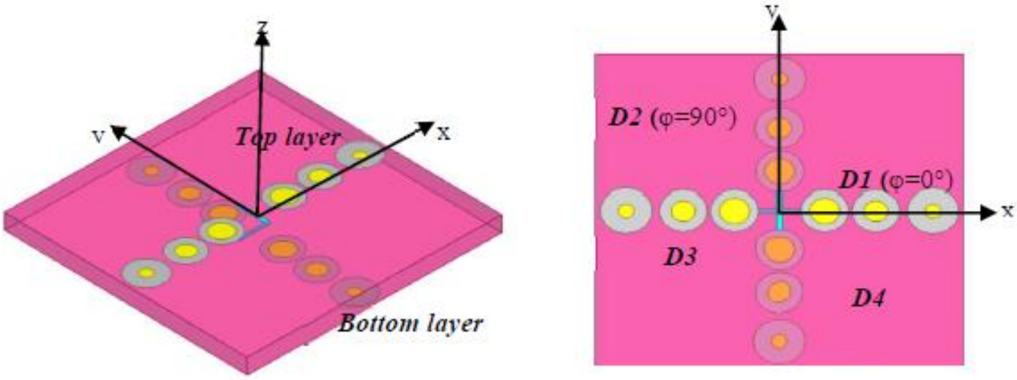

a. 3D view

b. Top view

Figure 3.10 : Yagi-Uda Structure [23]

In the structure of the antenna, graphene areas are turned on and off by changing the applied bias voltage, the mechanism shown in Figure 3.9. With the four orthogonal directions, the radiation beam can be changed for the same resonant frequency. [23]

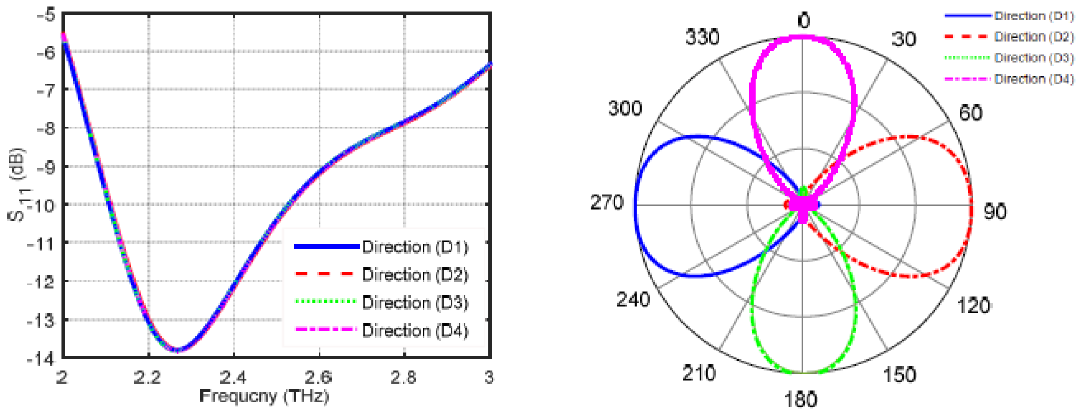

a. The reflection coefficients.

b. The 2D radiation patterns.

Figure 3.11 : Yagi-Uda antenna S_{11} and radiation patterns [23]

Another study [24] shows us that graphene is used like a pin-diode in the structure, with metal sheets in the same structure for the metasurface design for angle control at the THz band, and silicon dioxide is used as substrate. This structure is not an antenna, but it's very important to show us graphene used as pin-diode transistor switching with bias voltage. The structure designed for 3.3 THz, and the aim of the design is manipulating the reflected wave’s magnetic field angle using the 4 layers of the unit structure shown in Figure 3.12 and angular change shown in Figure 3.13

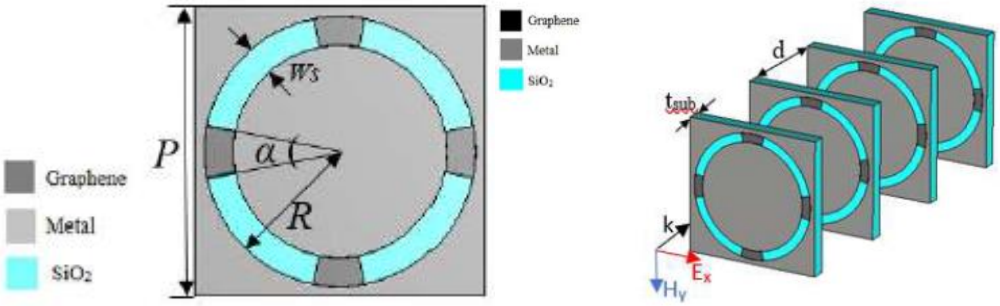

Figure 3.12 : The unit cell of the metasurface and four layers of the metasurface [24]

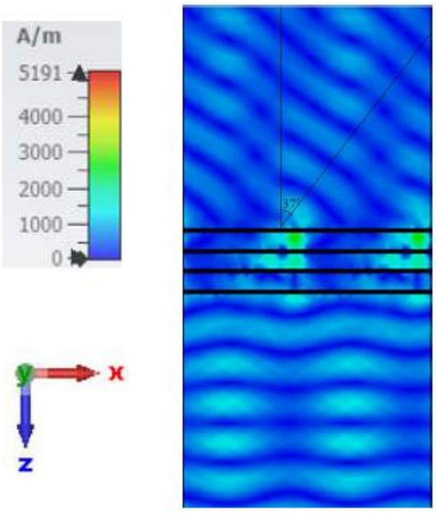

Figure 3.13 : The Magnetic Field, H_y, distribution of the wave at 3.3 THz [24]

According to a similar approach to [24], graphene is used as a gate when opened and closed by the applied bias voltage. In the antenna structure, the graphite is used for separating the area between them. according to an applied bias voltage, the antenna frequency changes between 2.472 THz and 2.652 THz, and the antenna bandwidth, respectively, is 176 GHz. With the graphene used in the two different areas of the antenna, the antenna acts like 4 different antennas for the on and off states of these two graphene areas. [25]

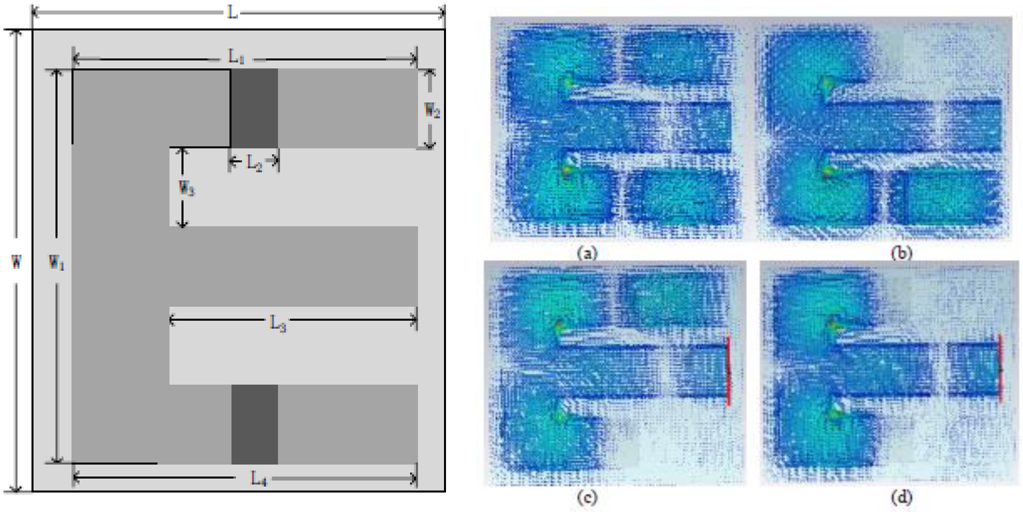

Figure 3.14 : Frequency Reconfigurable Antenna Structure and Working States [25]

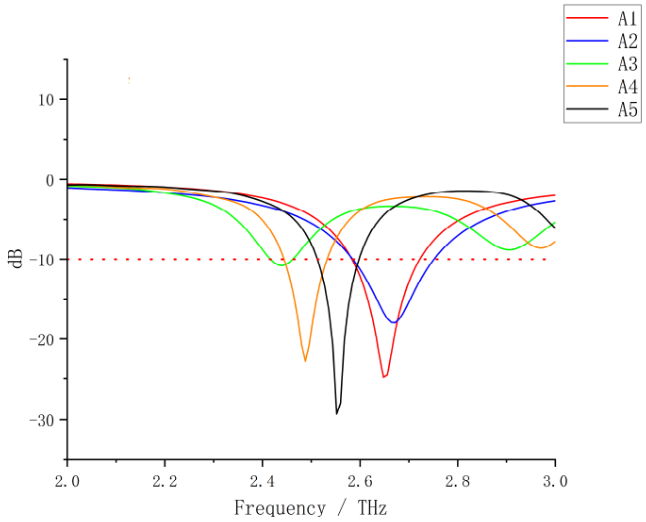

Figure 3.15 : S11 Parameters for each state of the antenna [25]

On the other hand, graphene-based antennas are used for beamforming for wireless ultrafast communication applications at 6.45 THz. [26] The maximum directivity of the antenna is 10.27 dBi, and the realized gain of the antenna is 9.86 dBi. The antenna has circular polarization and tuneable frequency using different applied bias voltages to graphene. After the unit antenna was designed, the antenna structure was modified to a MIMO antenna using the unit antenna for beam steering. [26]

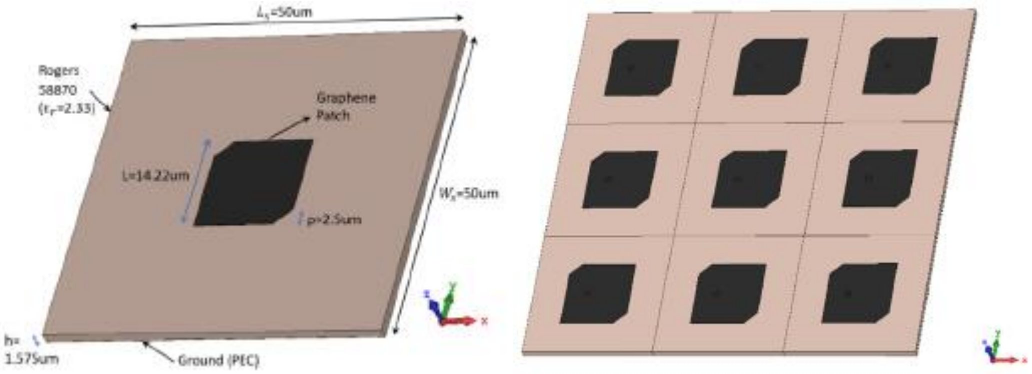

Figure 3.16 : Antenna Unit Cell and the MIMO Structure [26]

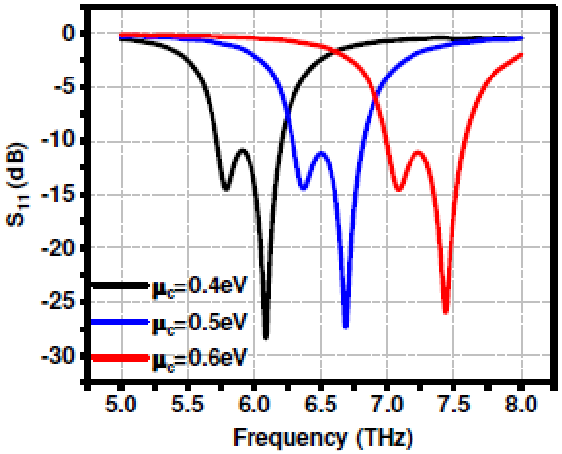

Figure 3.17 : S_{11} parameters of the MIMO [26]

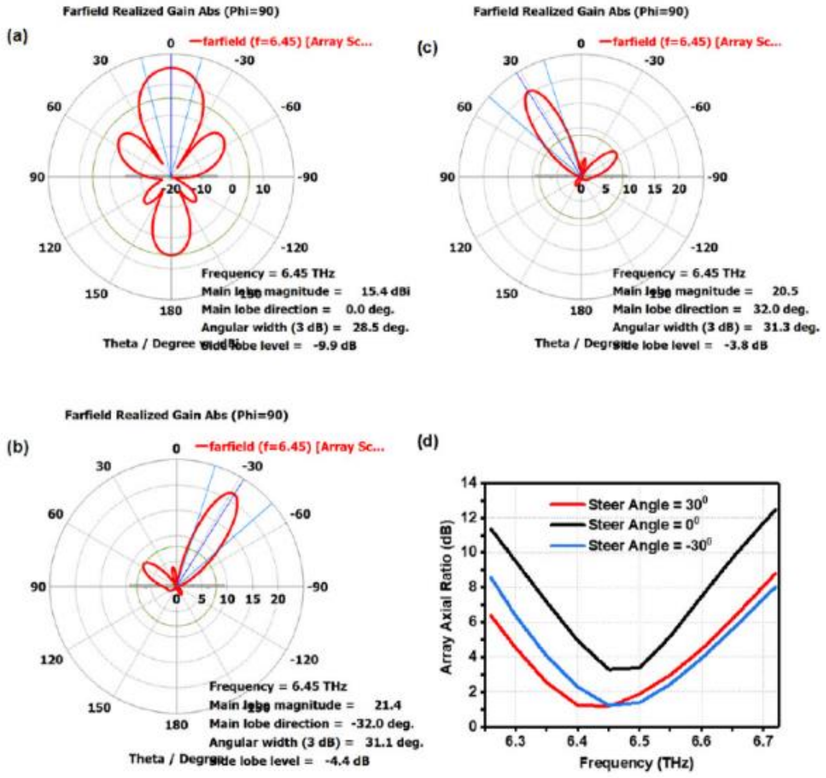

Figure 3.18 : Radiation Patterns and Axial Ratio for each beam steering state [26]

With that study [26] high efficient circular polarized tunable frequency antenna desinged and with the adjusting the phase diffrence for the units in MIMO beam steerig is achieved.

Another study about the wide bandwidth antenna with tunable frequency and beam steering characteristics is presented in [27]. The study describes the simple patch antenna structure with microstrip line feeding. The antenna uses silicon dioxide as a substrate and gold as a ground metal, with an operating frequency between 1.3 THz - 2.73 THz and 2.75 THz – 3.01 THz. The main difference in the study is that radiation angle chance with the frequency of the beam steering characteristic is not enabled at the same frequency.

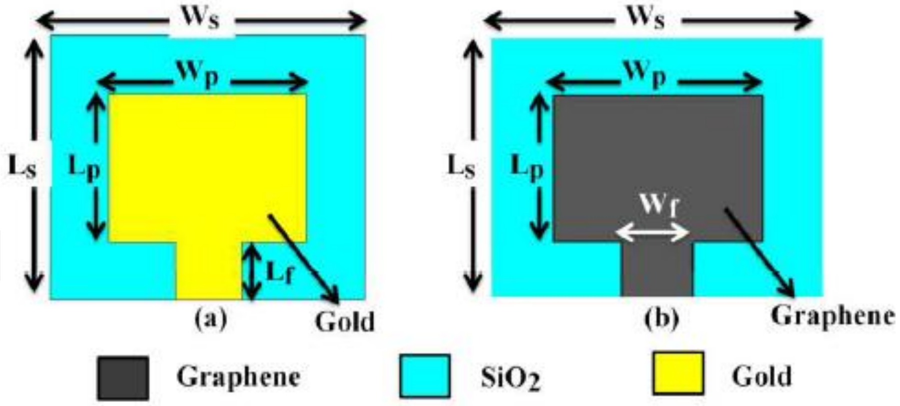

Figure 3.19 : Schematic for antenna structure [27]

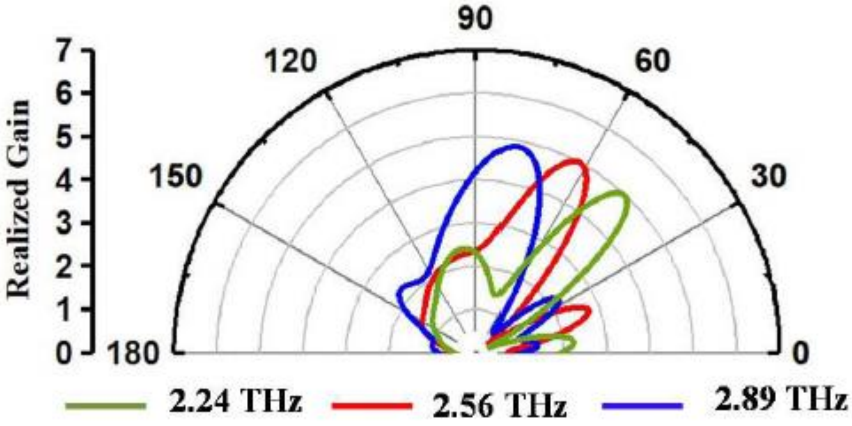

Figure 3.20 : Schematic for antenna structure [27]

When the antenna structures with circular polarization are examined [28], there are many different and interesting designs in the literature, but in some of these designs, the antennas have experimental designs [29], while under the designs and as in the circularly polarized patch antenna sections of many books on the subject, it is to create symmetry on the diagonal to create the electric field on the patch perpendicular to each other. Thus, it is aimed to create two electric fields of equal size and at right angles to each other on the antenna. To create this symmetry, different shapes of structures can be placed at the corners of the circular or nearly quadratic antenna. In the literature, it is possible to find many antennas that have achieved circular polarization in this way.

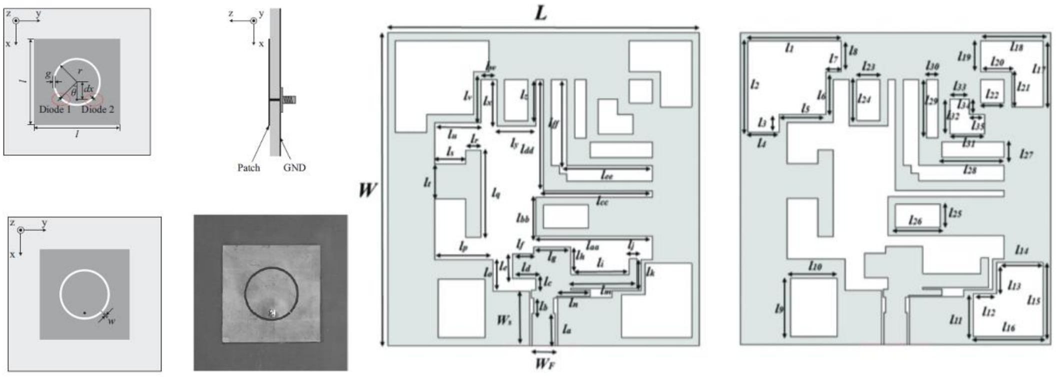

Figure 3.21 : Circular Polarization Patch Desing Examples [28,29]

In addition, another way to achieve circular polarization is to add slots inside the antenna, which are proportionally smaller in size. Thus, the currents generated on the patch rotate following the direction of shrinkage of the slots and form circular polarization.[8] This structure is called asymmetric slot in the literature. It offers a more practical application than antennas with circular polarization obtained by experimental approaches. [9,10] For this reason, a similar design was chosen to achieve circular polarization.

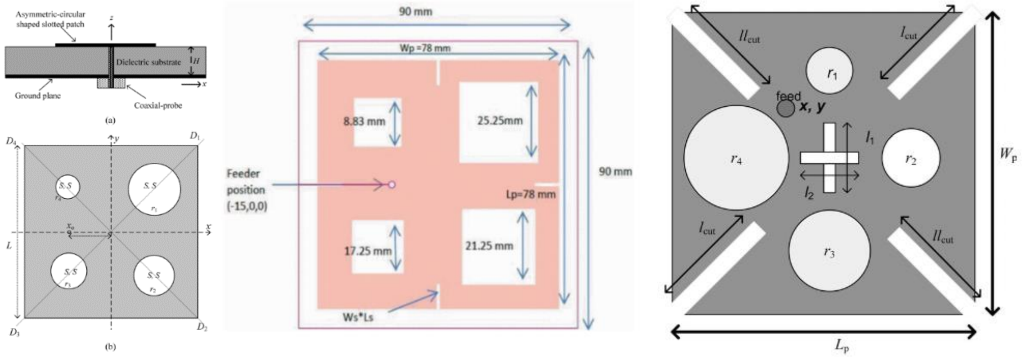

Figure 3.22 : Circular Polarization Asymmetrical Slots Antenna Examples [30,31,32]

As a second step, it will be important to understand the use of graphene in the antenna structure. Firstly, how graphene is integrated into the structure and how the structures of these antennas are constructed should be examined. In terms of feeding methods, microstrip feeding and probe feeding (or called pin feed in the literature) are used in antennas containing graphene. [33,34]

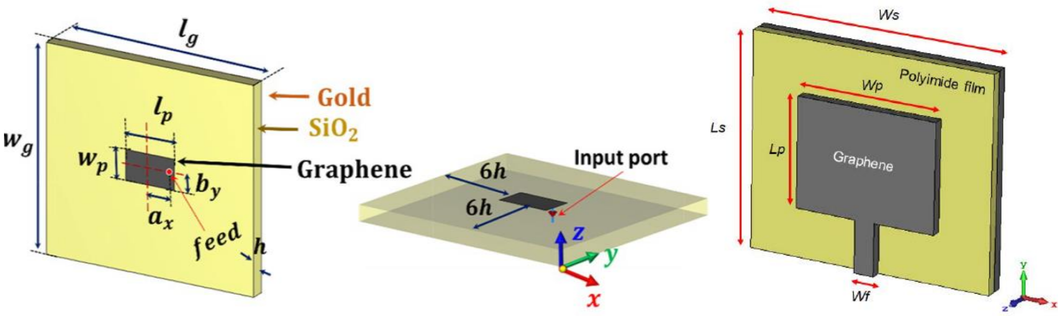

Figure 3.23 : Graphene Patch Antenna Feeding Examples [33.34]

In addition, although many different substrates are used, the most preferred substrate is generally silicon dioxide. [35] Considering these two issues, silicon dioxide was chosen as the substrate to be used in the design stages, and probe feeding was chosen as the feeding method because it is easy to match the antenna and provides the flexibility to feed the antenna from a symmetry point suitable for circular polarization.

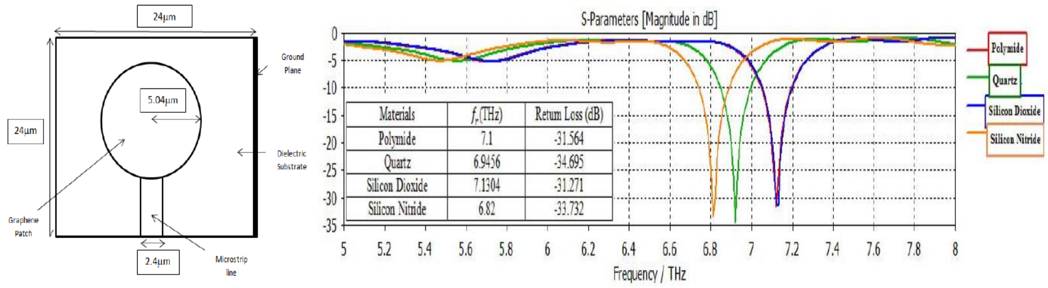

Figure 3.24 : Effects of Substrate Material for Graphene Patch Antenna [35]

Another thing that can be seen when examining graphene-containing antennas is that the characterization of the antenna can be changed by using voltage-applied graphene structures with different conductivity in different regions of the antenna. [36-38] These designs are an important guideline for achieving an antenna with switchable polarization, which is the aim of this thesis. Antenna structures that can switch between polarizations thanks to graphene placed on an ordinary patch antenna are a very important basis for this thesis.

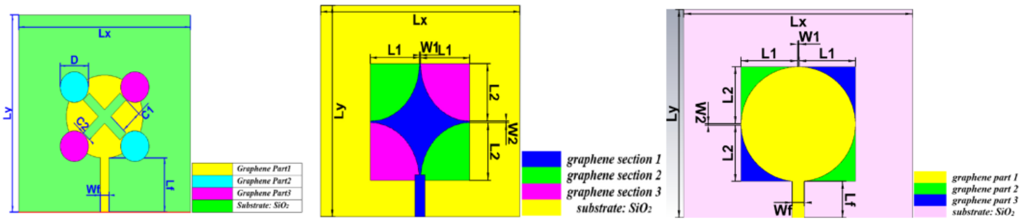

Figure 3.25 : Graphene Patch Antenna with Switchable Polarization [36-38]

4. GRAPHENE-COPPER BASED SWITCHABLE POLARIZATION PATCH ANTENNA FOR THz APPLICATIONS

In this study, our primary goal is to design a compact antenna that provides linear polarization, right-handed circular polarization, and left-handed circular polarization by feeding with a single transmission line in a simple structure. For this, we need to find out which methods and geometries we can use to achieve circular polarization. There are three traditional approaches to achieve this in the literature. The first one is to feed the patch antenna with multiple feedlines from different points with a phase difference between them. For example, the antenna can be fed by four feedlines with a phase difference of 90 degrees or three feedlines with a phase difference of 120 degrees. This method is one of the most effective, but it requires a complex feeding network design when only one feed is required. Otherwise, the antenna will be too far away from the simple design and will not be manufacturable because you are using too many feeds.

Another method is to rotate antennas with linear polarization at certain angles to obtain an array and feed the antennas in this array in sequence to obtain circular polarization. However, this approach also takes up a lot of space due to the large number of antenna elements in the structure

In the third and last method, the patch is designed to be almost symmetrical. For example, for a rectangular patch antenna, the antenna width and length should be almost identical. In this structure, the feed point is placed on the diagonal line of the antenna, creating two nearly equal symmetrical structures. Even though these structures are almost identical, due to the slight difference between them, they behave like two antennas operating at close frequencies and generating perpendicular electric fields. Another way to achieve this is to add or remove symmetrical structures at the corners of the diagonal line of the patch. In this way, an axis of symmetry can be created on the antenna, and circular polarization can be achieved. It is also possible to achieve circular polarization by adding asymmetric slots in the center of the patch. As you can see, there are many ways to achieve circular polarization. In this method, circular polarization can be realized with many design options and without complex structures. That is why we decided to use this method.

4.1 Design of Circular Polarization Circular Patch Antenna with Asymmetric Slots

First, a circular patch antenna with an operating frequency of 6 THz was designed. In the design, 1.5 micrometers thick Silicon dioxide was used as the substrate. Probe feeding was used as the feeding method. The first simulations of the design were performed in the HFSS program. With the integration of graphene into the design, the design was simulated in the CST program. The substrate size for the circular antenna was 35 x 35 micrometers. The patch radius was determined to be 6.8 micrometers and fed with probe feeding. Simulation results for these design parameters are shown below.

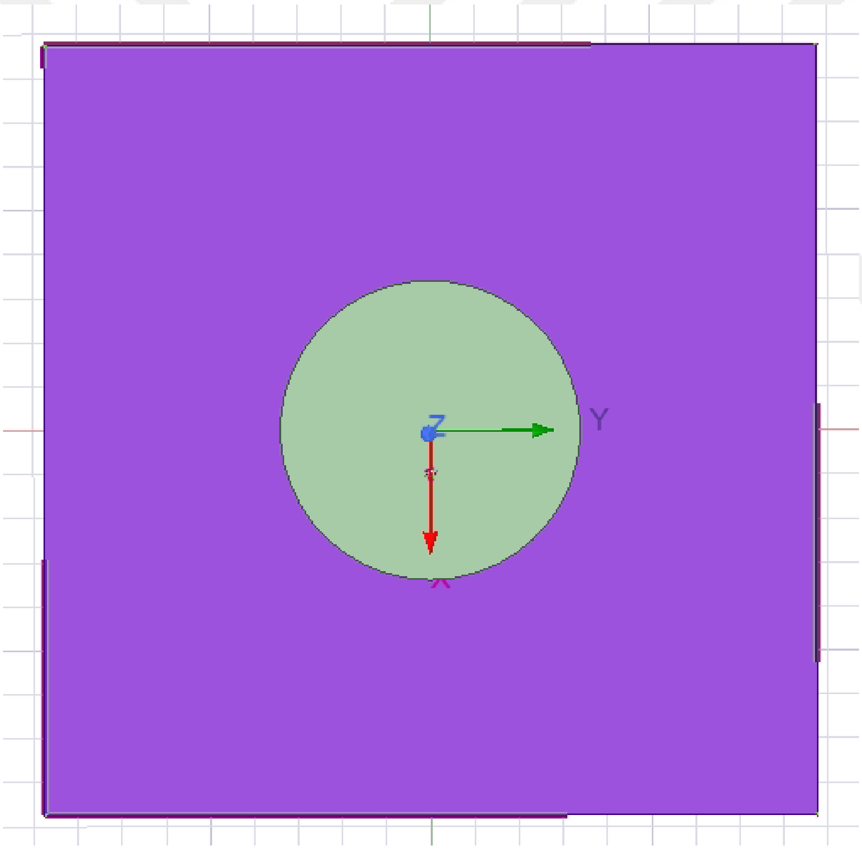

Figure 4.1 : Circular patch antenna

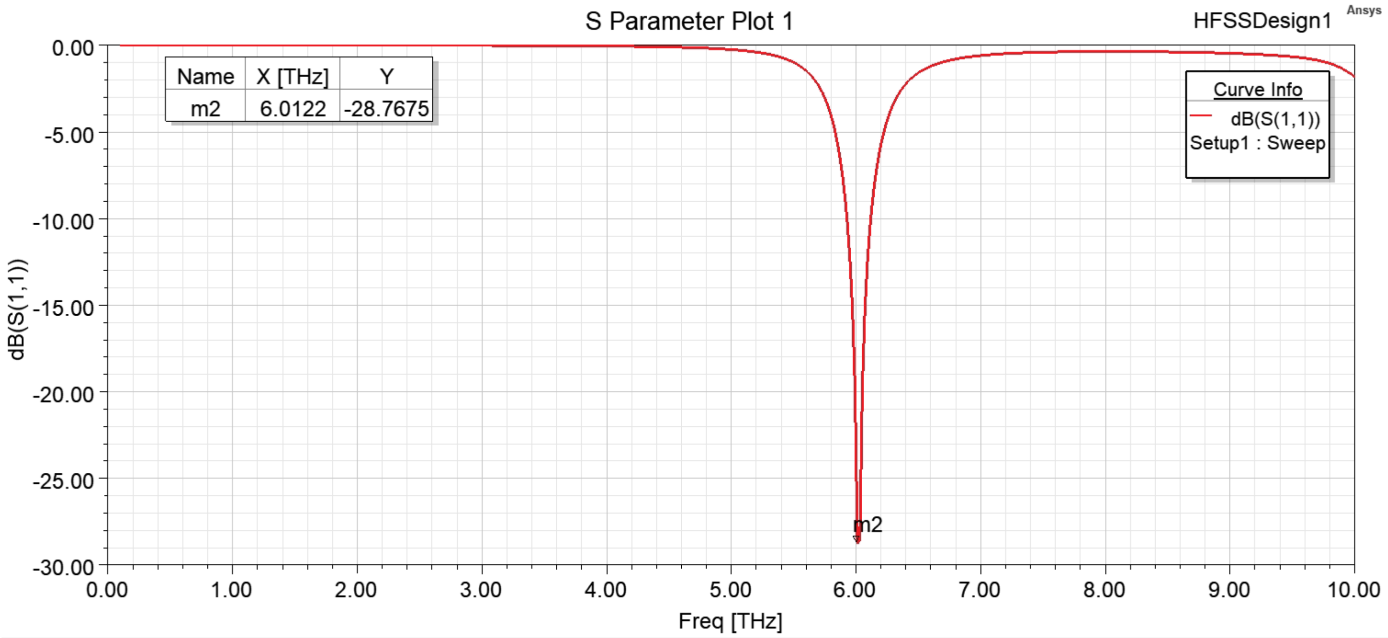

Figure 4.2 : S_{11} results of circular patch antenna

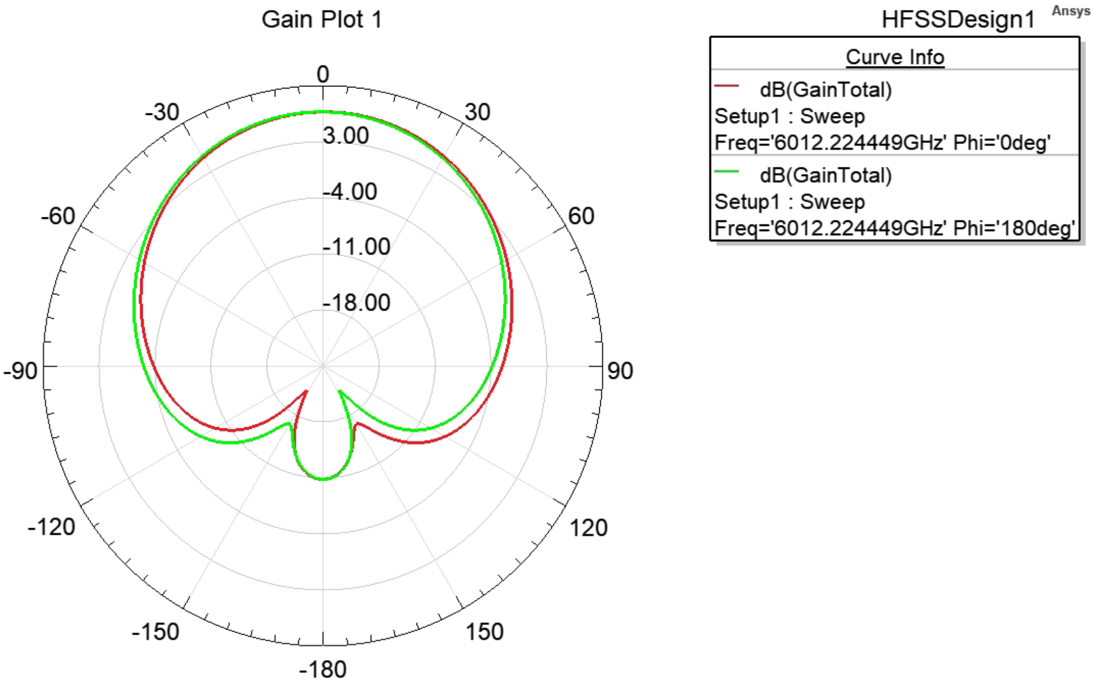

Figure 4.3 : Gain plot ($\Theta = 0^0$ and $\varphi = 180^0$ and 0^0) of circular patch antenna

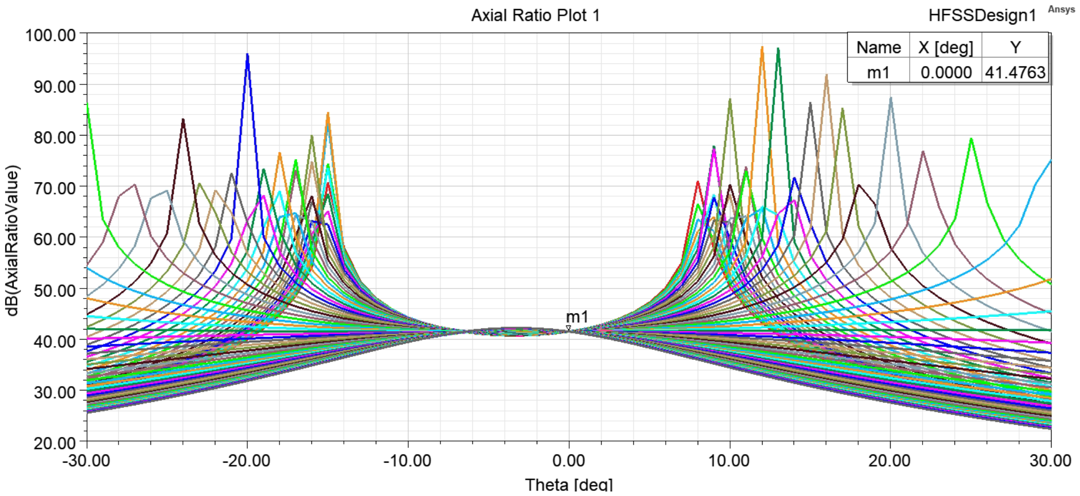

Figure 4.4 : Axial Ratio graphic of circular patch antenna

It was observed that the antenna operates at 6 THz frequency. When the axial ratio of the antenna was examined, it was found to be 41 in the main beam direction. We can say that the antenna has linear polarization.

In the next step of the design, circular polarization is achieved by adding asymmetric slots on the antenna edges. While creating the structure of the asymmetric slots, the tangent square corners around the circular patch formed the fixed corner of the slots. In these 4 fixed corners, 4 separate slots were placed. The sizes of the slots were determined to decrease proportionally so that the current on the patch surface rotates in the direction where the slot size decreases. The findings of the design can be found below.

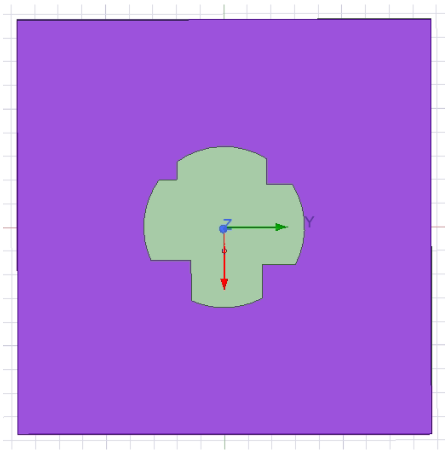

Figure 4.5 : Circular patch antenna with asymmetric slots

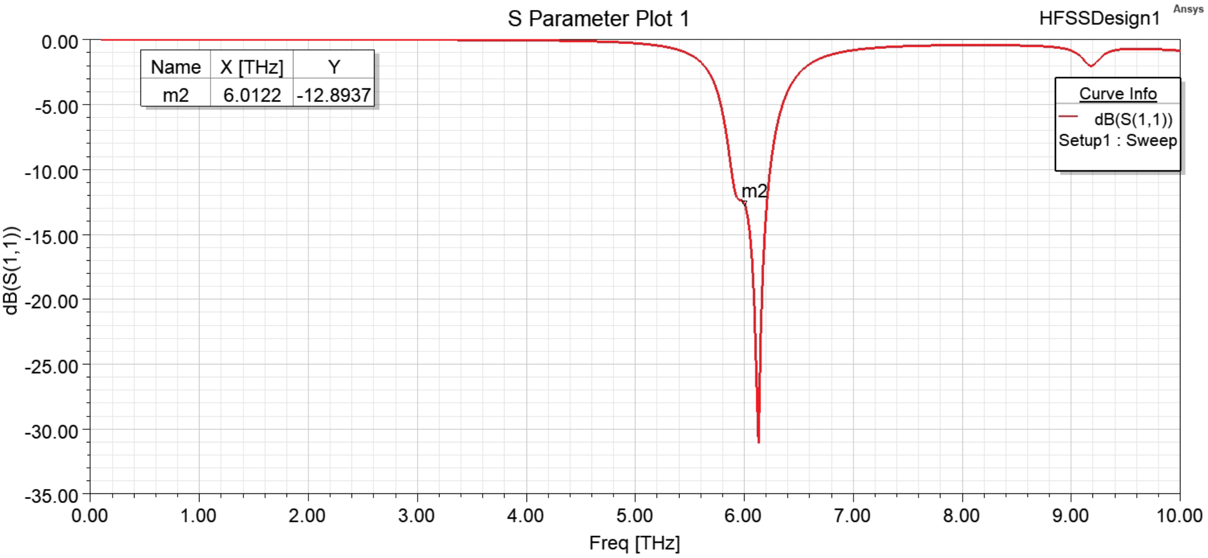

Figure 4.6 : S_{11} graph of circular patch antenna with asymmetric slots

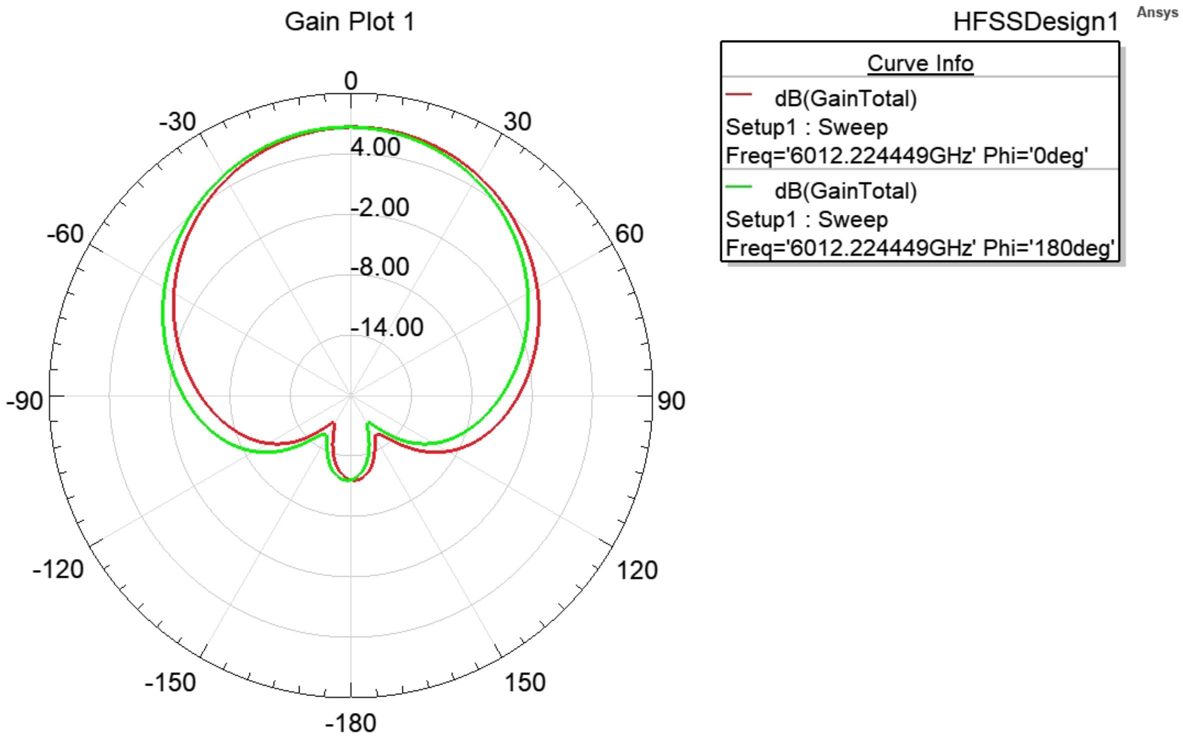

Figure 4.7 : Gain plot ($\Theta = 0^0$ and $\varphi = 180^0$ and 0^0) of circular patch antenna with asymmetric slots

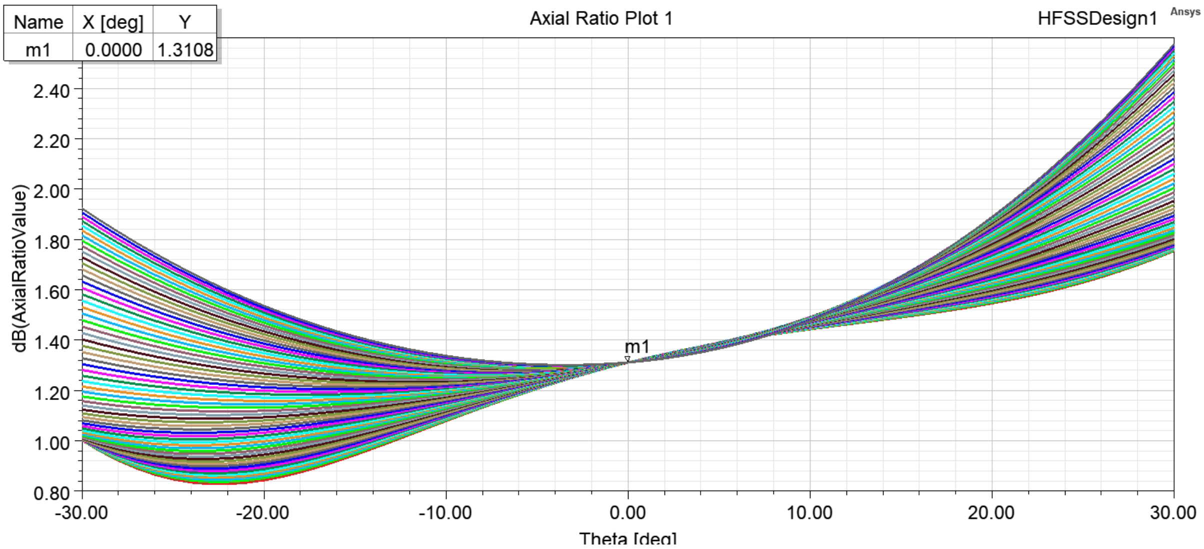

Figure 4.8 : Axial Ratio graphic of circular patch antenna with asymmetric slots

For circular polarization, the axial ratio of the antenna was 1.31 dB. Thus, it can be said that the antenna has circular polarization. In the S_{11} graph, it is seen that two different resonances are formed around 6 THz due to the asymmetry (horizontally dominant mode and vertically dominant mode due to the asymmetry at very close frequencies) and that the antenna provides circular polarization at 6THz where they intersect. The ratios of the slots from the biggest one to the smallest are 1, 0.9, 0.8, 0.7, and the first slot is square, and the dimension of the one edge of these squares is 4 micrometers from the reference corner as described before.

At this point, the difficult part of the design is to incorporate graphene, a material whose conductivity we can control, into the design so that the antenna has both bidirectional circular polarization (RHCP and LHCP) and linear polarization. At this point, different bias voltages were applied to the graphene parts used to switch between these polarizations. Due to the difficulty of simulating graphene in the HFSS program, CST was used as an alternative.

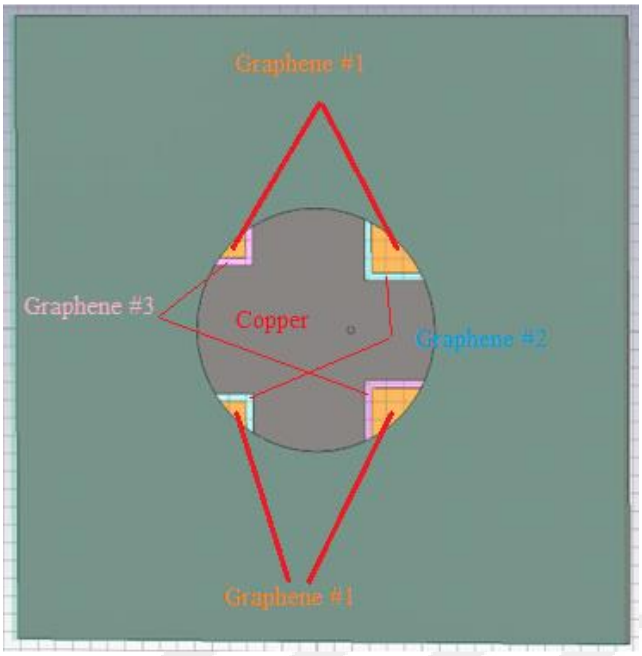

Figure 4.9 : Graphene added circular patch

The main part of the patch is the copper area, which is shown in gray. The areas shown in color are the different areas where graphene is used. Parameters used when defining graphene in the CST program are graphene thickness, graphene temperature in Kelvin, graphene chemical potential, and relaxation time of graphene in ps. All parameters are the same for all polarizations except the chemical potential of graphene. Graphene thickness was used as 0.01 micrometer, Graphene temperature in Kelvin was used as 300 Kelvin, and the Relaxation time of Graphene was 0.1 ps. The reason why these areas are different is that different bias voltage are applied to these areas to create different asymmetric slot structures to ensure the transition between polarizations. The chemical potential parameter of graphene is used to generate different bias voltages applied to graphene regions according to polarization. The chemical potential (eV) values applied according to polarization types are shown in the following table.

Table 4.1 : Graphene Chemical Potentials

Polarization	**Graphene 1 (Yellow)**	**Graphene 2 (Blue)**	**Graphene 3 (Pink)**
LP	ON (25 eV)	ON (25 eV)	ON (25 eV)
RHCP	OFF (0 eV)	ON (5 eV)	OFF (0.11 eV)
LHCP	OFF (0 eV)	OFF (0.11 eV)	ON (3 eV)

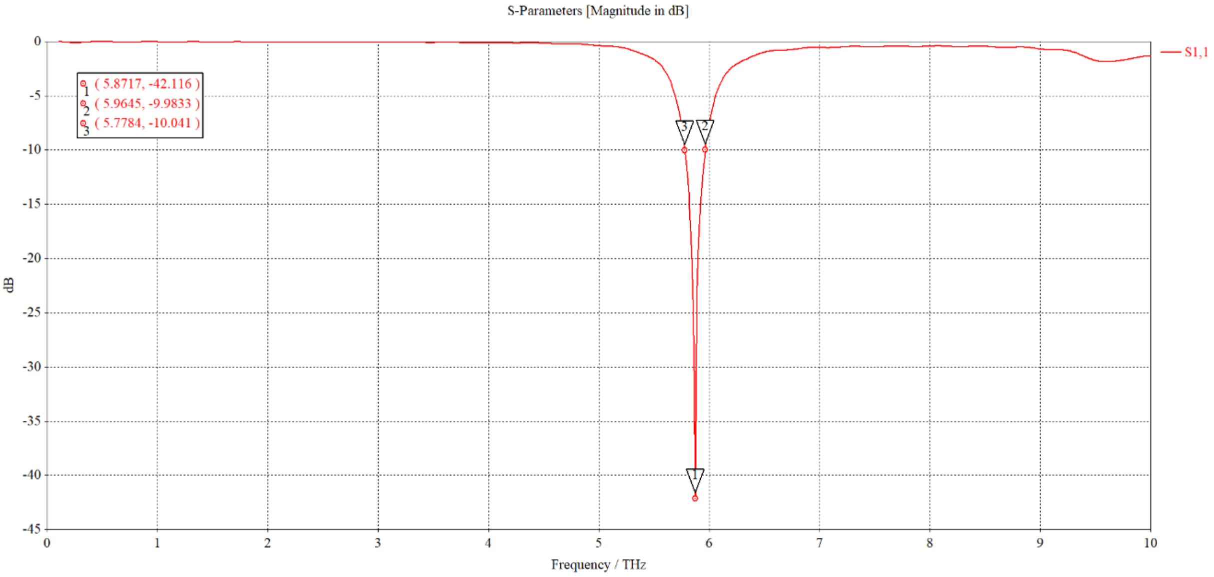

Figure 4.10 : S11 graph for Linear Polarization Configuration

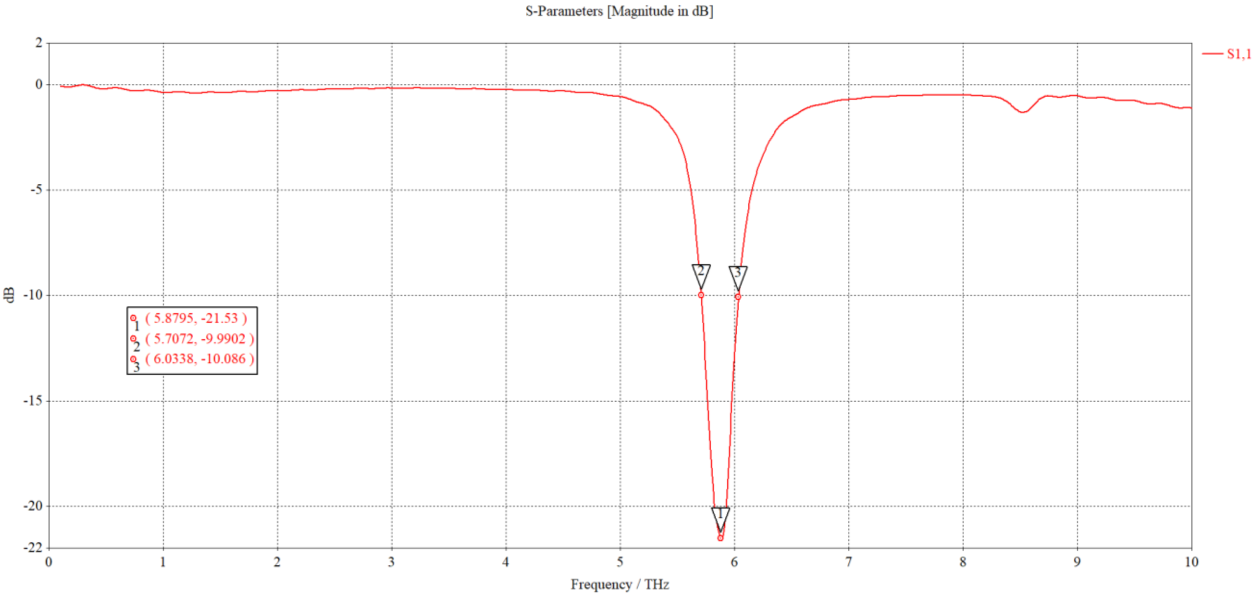

Figure 4.11 : S11 graph for LHCP Polarization Configuration

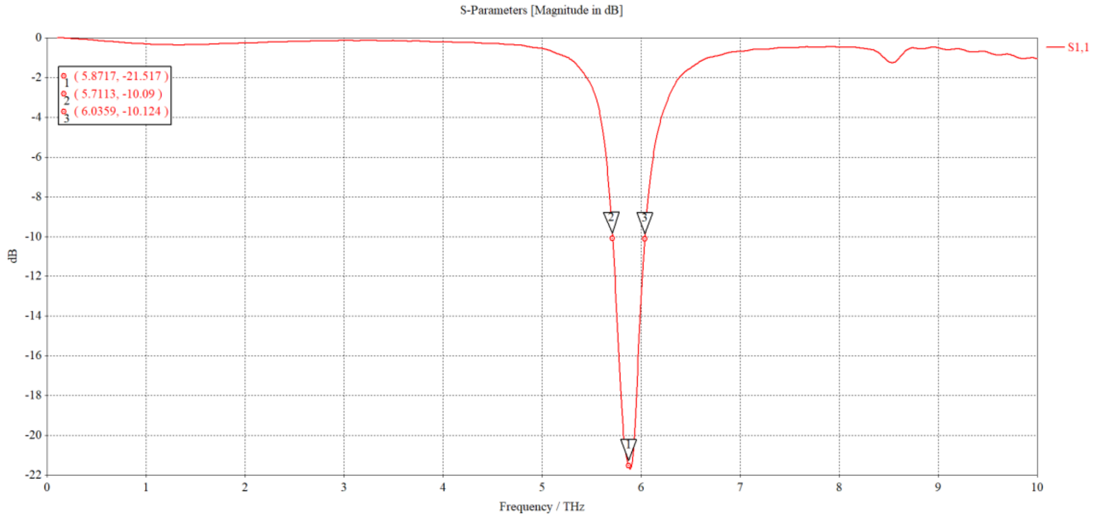

Figure 4.12 : S_{11} graph for RHCP Polarization Configuration

As can be seen from the S_{11} parameters, parametric analysis with the chemical potential of graphene showed that the operating frequency for all polarizations varies between 5.87 - 6 THz. It can be seen that the bandwidth for RHCP and LHCP polarizations is 0.3 THz and 0.2 THz for LP. However, when we look at the S_{11} graphs of all polarizations, it is seen that the graphs of LHCP and RHCP polarizations are almost the same, and the antenna with LP polarization is within the operating region of RHCP and LHCP. Although there is a shift in the operating frequency, it can be said that the antenna operates in the same frequency region in the case of 3 polarizations. The axial ratios of the antenna configurations can be found below.

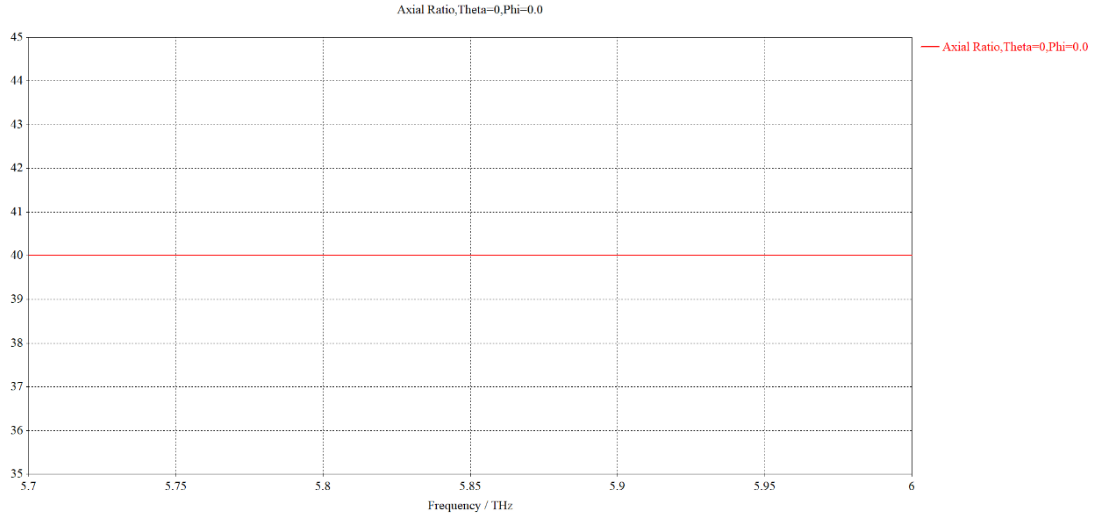

Figure 4.13 : Axial Ratio graph for Linear Polarization Configuration

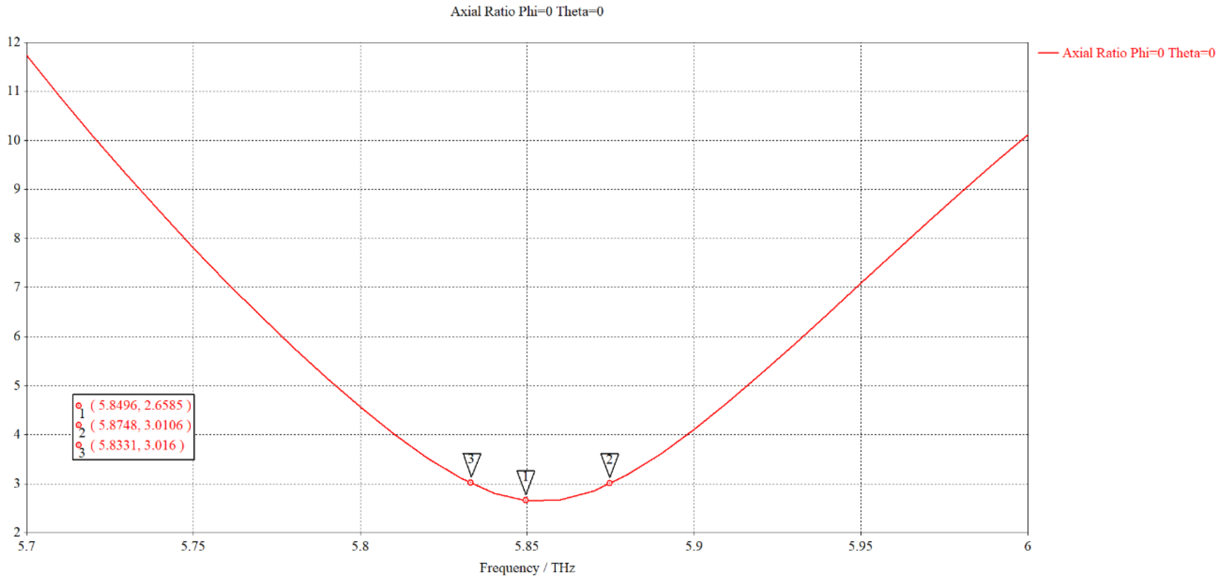

Figure 4.14 : Axial Ratio graph for RHCP Polarization Configuration

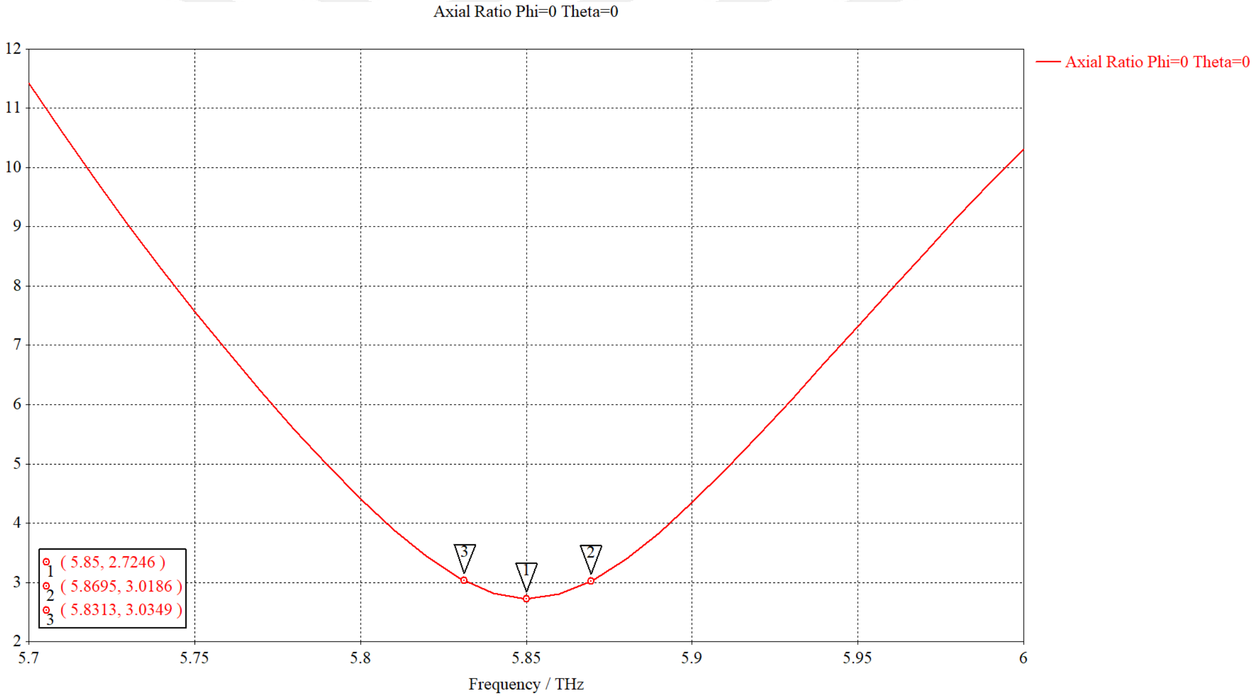

Figure 4.15 : Axial Ratio graph for LHCP Polarization Configuration

When we look at the axial ratios for different polarizations, we see that the axial ratio for LP is 40. This is a very ideal axial ratio value for linear polarization. When we examine the axial ratio for RHCP, it can be seen that it has an axial ratio between 5.87 THz and 5.83 THz, which is below 3 dB, which is the acceptable value for circular polarization. Likewise, LHCP can be seen to provide circular polarization with an axial ratio below 3 dB between 5.875 THz and 5.83 THz. All axial ratio measurements were made in the main beam direction and measured at φ=0^0 and Ө=0^0 angles. According to all these results, all polarizations provide LP, RHCP, and LHCP polarizations within the bandwidth shown in the S_{11} parameters. As mentioned, 2D radiation patterns are useful in showing the main radiation direction of the antennas.

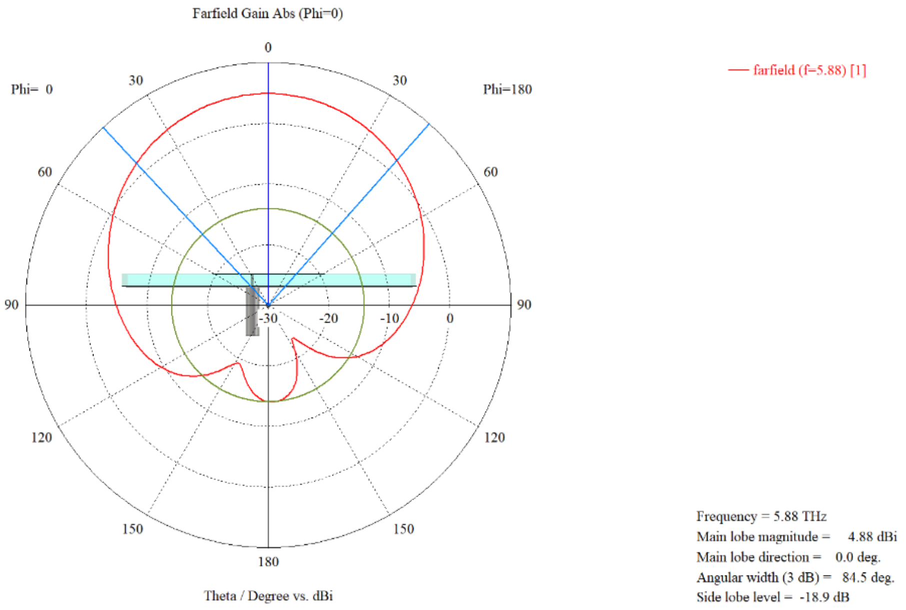

Figure 4.16 : Gain plot for LP

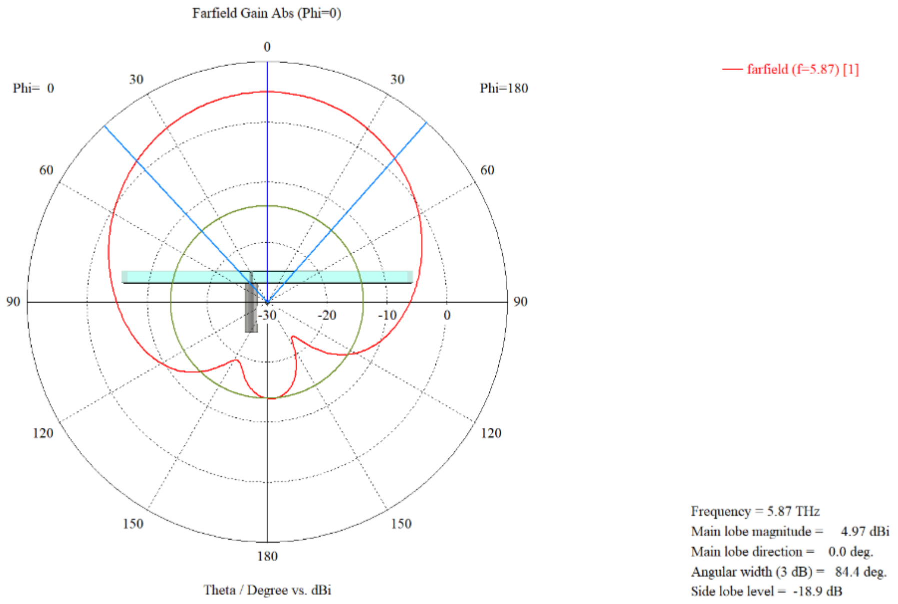

Figure 4.17 : Gain plot for RHCP

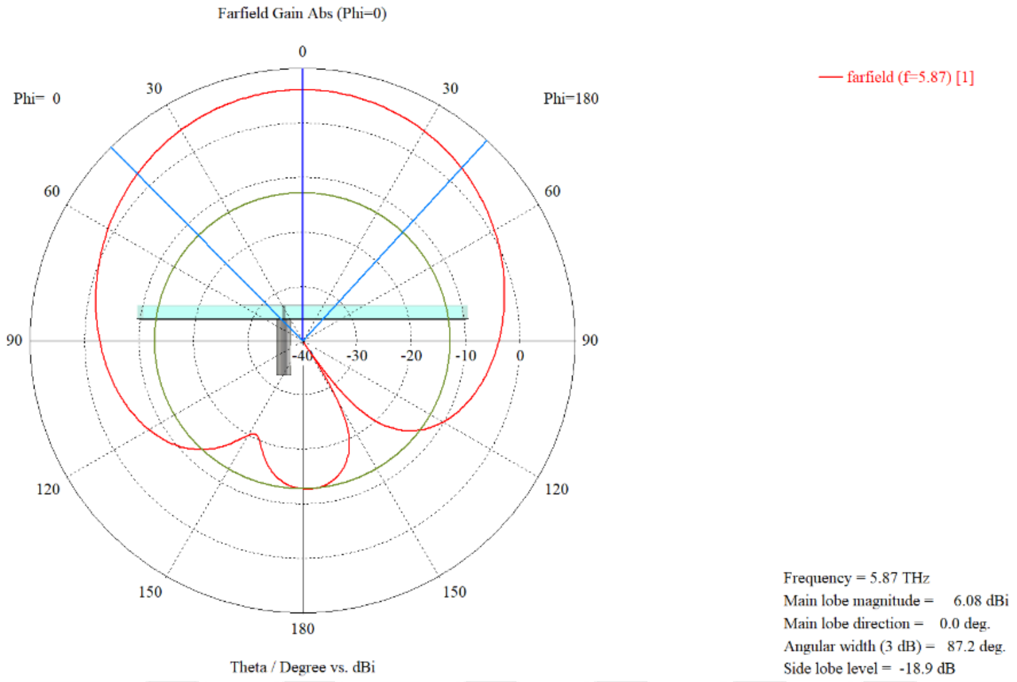

Figure 4.18 : Gain plot for LHCP

Table 4.2 : Antenna Gain and Directivity Table

Polarization	**Gain** **(φ=0, Ө=0)**	**Directivity** **(φ=0, Ө=0)**
LP	5.83 (dBi)	6.93 (dBi)
RHCP	5.27 (dBi)	6.89 (dBi)
LHCP	5.27 (dBi)	6.89 (dBi)

With different design approaches, it is possible to develop antenna designs with switchable polarization using graphene and copper. One of the antenna designs developed in this direction is the design we realized by placing an asymmetric cross in the middle of the patch. All basic parameters, such as the radius of the patch, the substrate used, and the substrate thickness, remain the same. In the asymmetrically designed slot, graphene is defined in 3 different regions. By applying different bias voltages to these regions, the conductivity of graphene is changed, and the antenna polarization is changed. The general structure of the antenna is shown below.

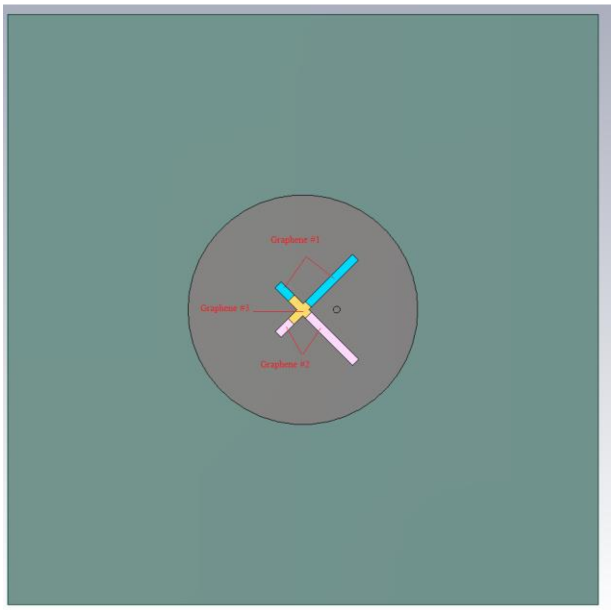

Figure 4.19 : Cross shape graphene added circular patch

Table 4.3 : Graphene Chemical Potentials

Polarization	**Graphene 1 (Blue)**	**Graphene 2 (Pink)**	**Graphene 3 (Yellow)**
LP	ON (3 eV)	ON (3 eV)	ON (3 eV)
RHCP	OFF (0.1 eV)	ON (2.5 eV)	OFF (0.6 eV)
LHCP	ON (2.5 eV)	OFF (0.1 eV)	OFF (0.6 eV)

S_{11} plots for all polarizations are shown below:

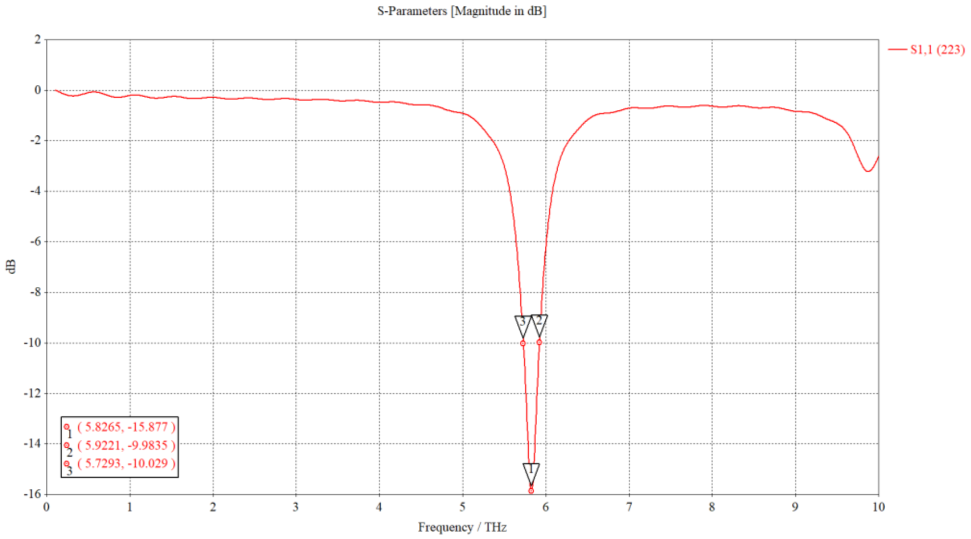

Figure 4.20 : S_{11} graph for Linear Polarization of antenna with cross

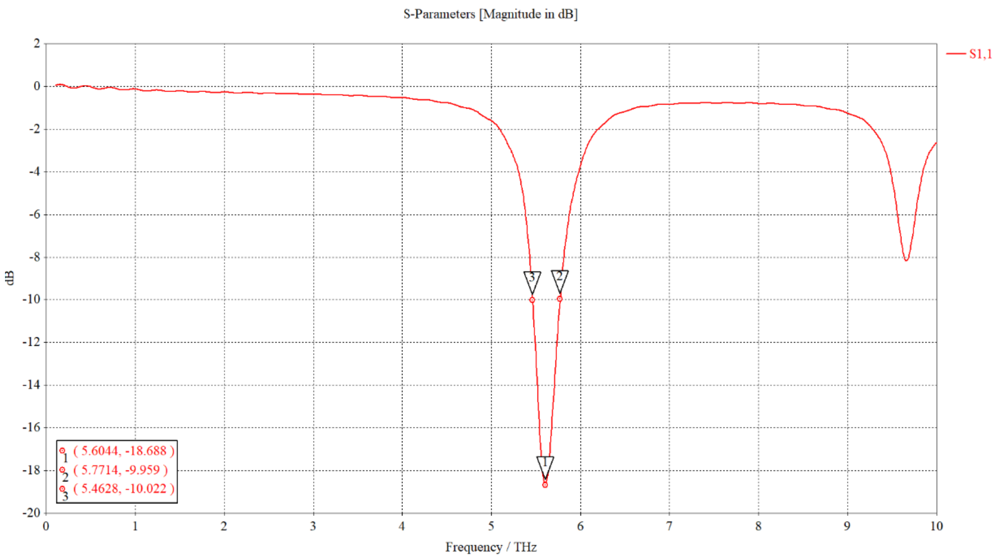

Figure 4.21 : S_{11} graph for RHCP Polarization of antenna with cross

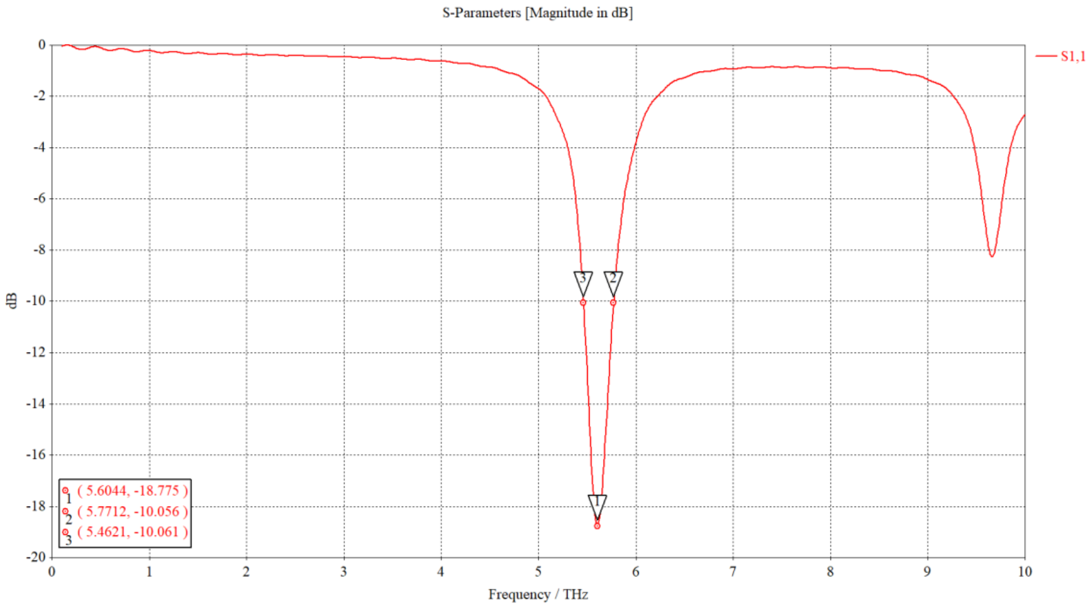

Figure 4.22 : S_{11} graph for LHCP Polarization of the antenna with cross

As seen in the S_{11} graphs of RHCP and LHCP polarizations, the patch operates at a frequency of 5.60 THz and has a bandwidth of approximately 0.3 THz. In the LP polarization, it is seen that it operates at a frequency of 5.82 THz and has a bandwidth of 0.2 THz. In this way, unlike the previous structure, there is a shift in the operating frequency in the configuration made for RCHP and LHCP polarizations with LP. Nevertheless, the ability to switch between different polarizations is preserved. The graphs of the axial ratios of the building are as follows:

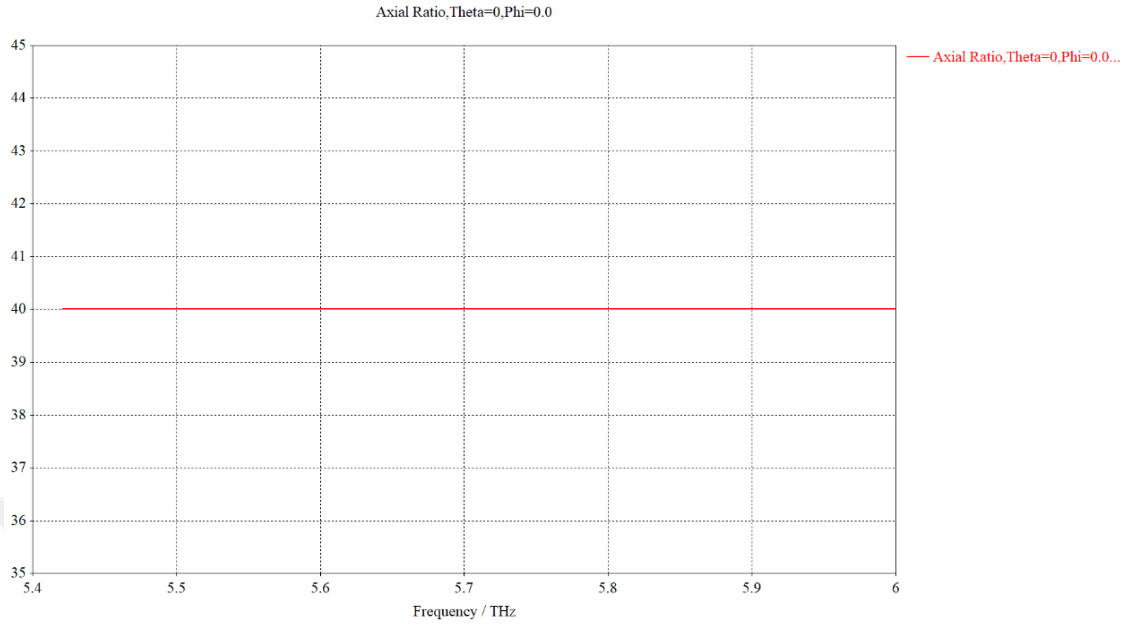

Figure 4.23 : Axial Ratio graph for Linear Polarization of the antenna with cross

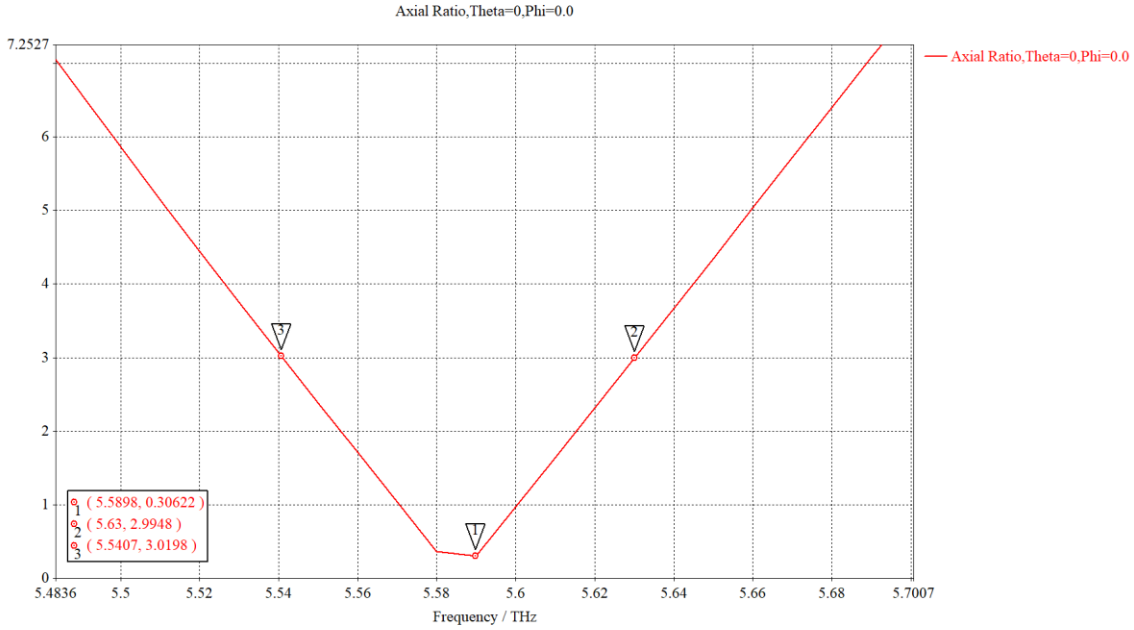

Figure 4.24 : Axial Ratio graph for RHCP Polarization of the antenna with cross

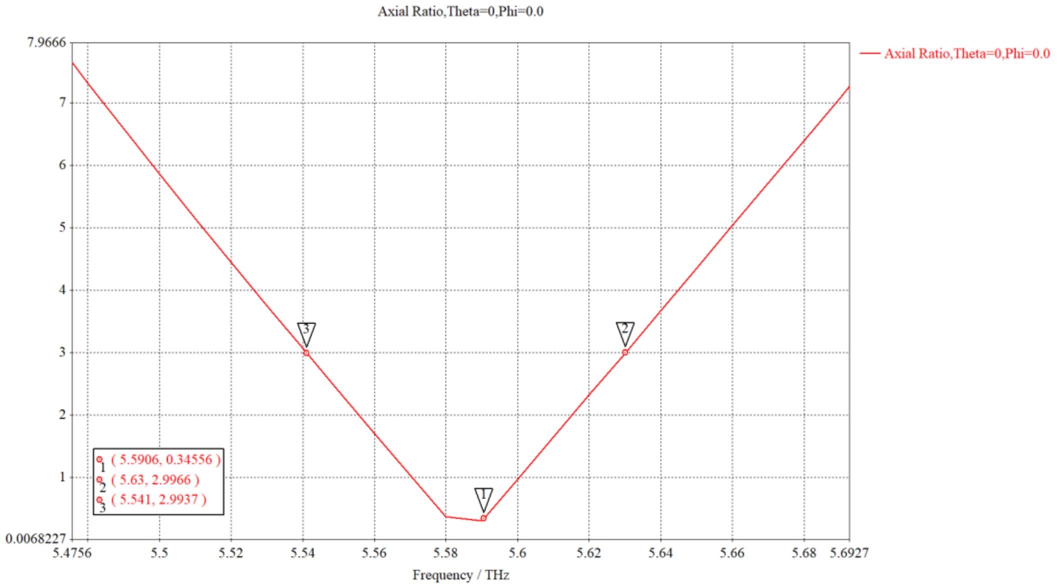

Figure 4.25 : Axial Ratio graph for LHCP Polarization of the antenna with cross

Looking at the axial ratios of RHCP and LHCP, according to the S_{11} plot, the axial ratios are 0.3 and 0.34 for RHCP and LHCP, respectively. Thus, a result that was much closer to the perfect circular polarization was obtained compared to the previous study. For LP, the axial ratio is obtained as 40. The minimum point of the axial ratio is almost at the center of the operating frequency. The measurement results were performed in the main radiation direction ($\Theta = 0^0$ and $\varphi = 0^0$). The radiation direction can be seen in the 2D radiation graphs below:

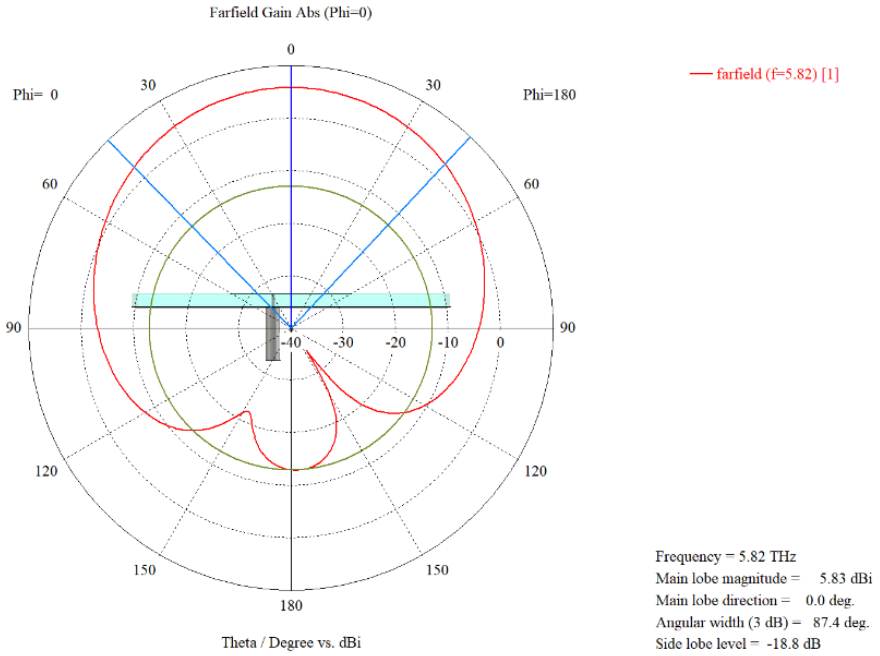

Figure 4.26 : Gain plot for LP antenna with cross

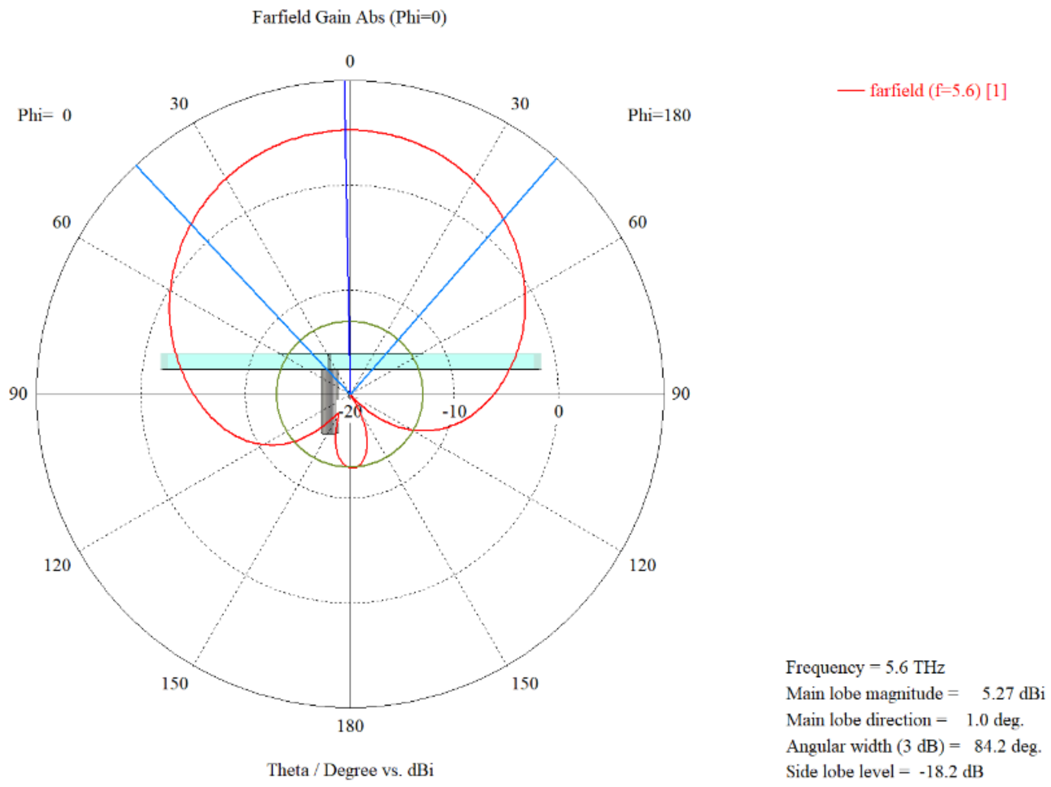

Figure 4.27 : Gain plot for RHCP antenna with cross

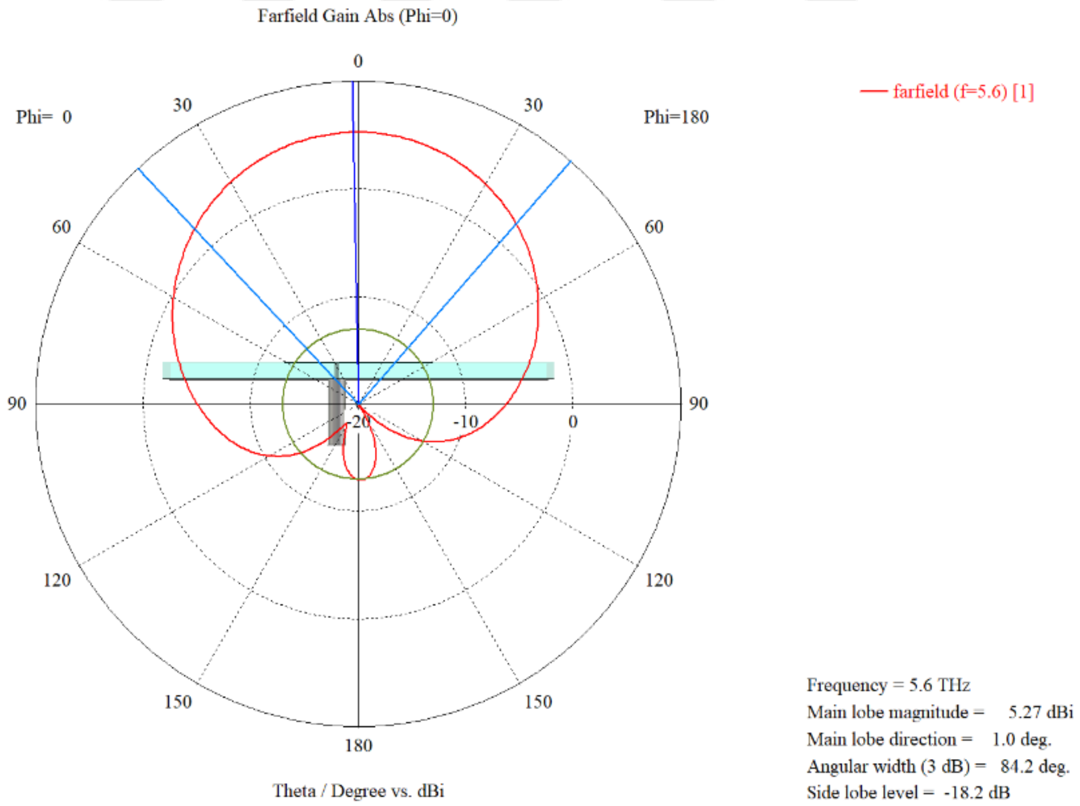

Figure 4.28 : Gain plot for LHCP antenna with cross

Table 4.4 : Antenna Gain and Directivity Table

Polarization	**Gain** **(φ=0, ϴ=0)**	**Directivity** **(φ=0, ϴ=0)**
LP	5.83 (dBi)	6.93 (dBi)
RHCP	5.27 (dBi)	6.89 (dBi)
LHCP	5.27 (dBi)	6.89 (dBi)

As a different design alternative, as a third design alternative, instead of a graphene region with 3 different bias voltages, only two graphene regions with two different bias voltages were designed. Instead of the sharp quadrangular structures in the previous designs, Cassini oval-like structures were used in the antenna. Since the x and y components of the Cassini oval equation are interconnected, equation 4.1 was used as the x component, and equation 4.2 was used as the y component due to the problematic modeling of such an equation in CST.

$$x = \mathrm{r}\cos(2\Theta) \tag{4.1}$$

$$y = r^3 \sin(\Theta) \tag{4.2}$$

where $\mathrm{r} = 2$ and $0 < \Theta < \pi$.

The substrate material and dimensions and antenna patch radius, are the same as the first design as previous ones. Based on the same principle as the previous designs, two different bias voltages were applied to the graphene in the antenna slots, as shown in Fig. 4.9, and different bias voltages were applied to the graphene regions to change the antenna polarization. During the design, slots are placed similarly to Cassini ovals, and the reduction ratio of the slots between each other is 0.6 for each size step.

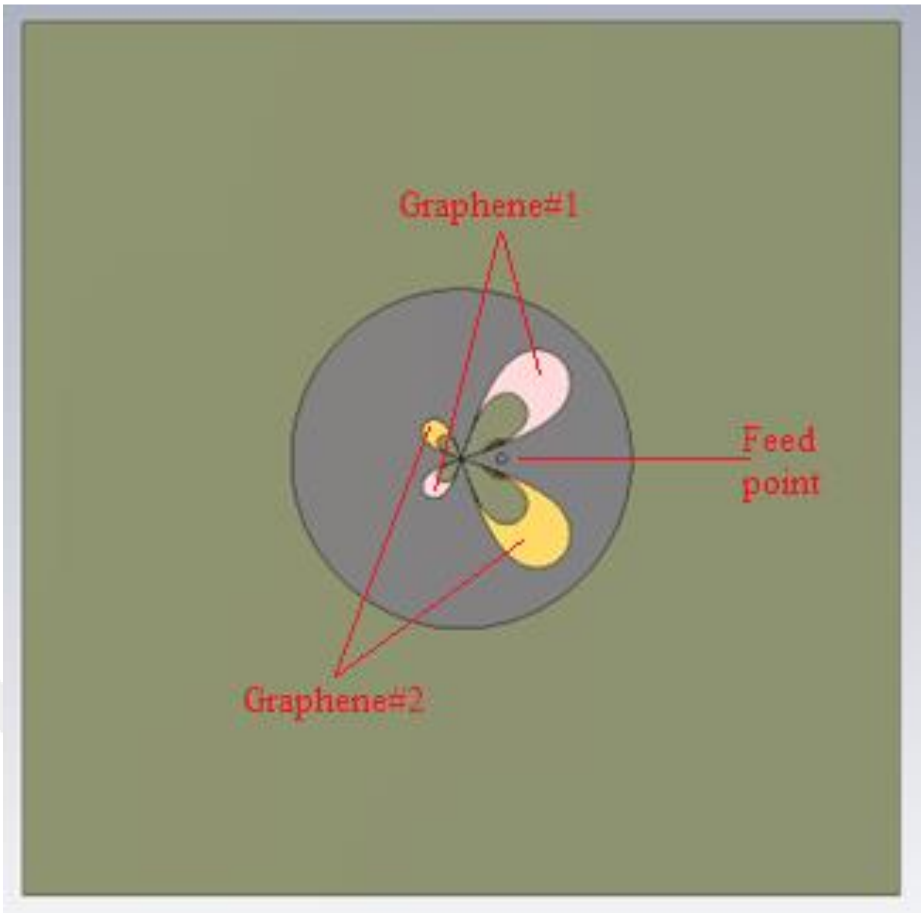

Figure 4.29 : Circular Patch with Cassini oval slots

Table 4.5 : Graphene Chemical Potentials

Polarization	Graphene 1 (Pink)	Graphene 2 (Yellow)
LHCP	ON (4.5 eV)	OFF (0.1 eV)
RHCP	OFF (0.1 eV)	ON (4.5 eV)
LP	ON (4.5 eV)	ON (4.5 eV)

The table above shows the bias voltage applied to the graphene regions for different polarizations of the antenna with Cassini oval slots. The graphene bias voltages are arranged so that the operating frequency of all polarizations is the same.

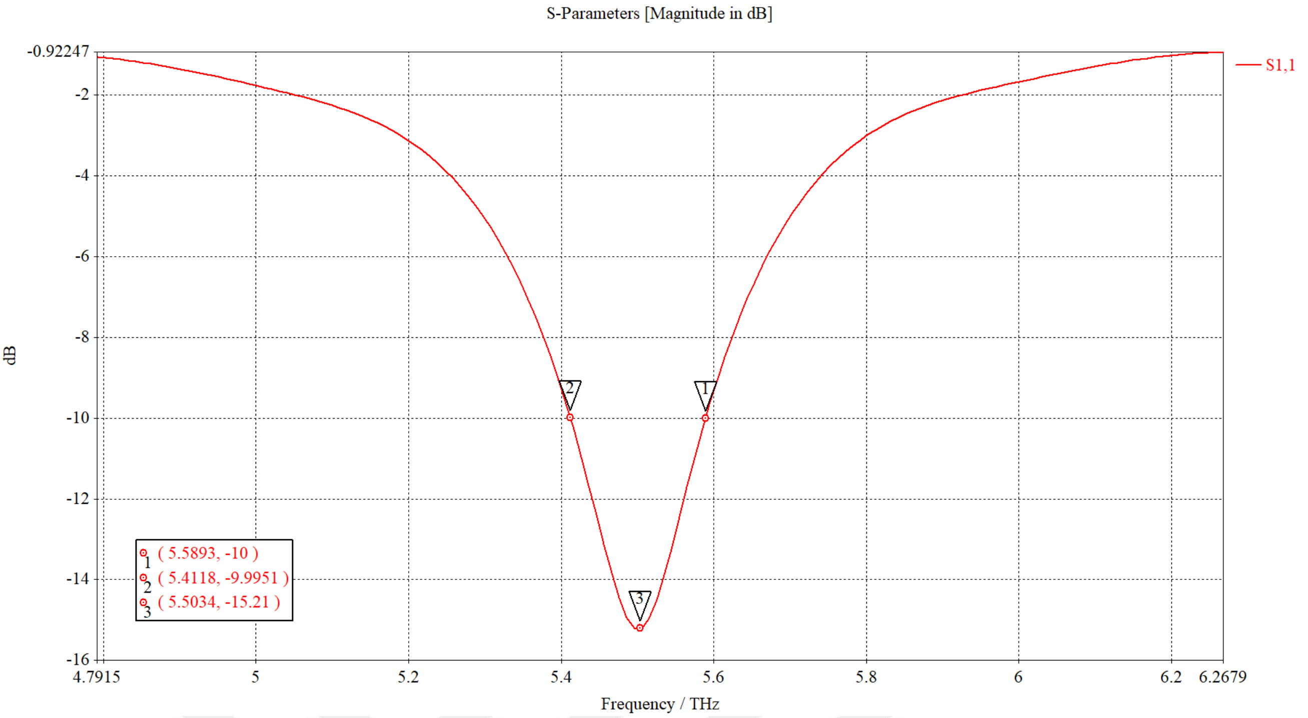

Figure 4.30 : S_{11} graph for LP Polarization of the antenna with cassini oval slots

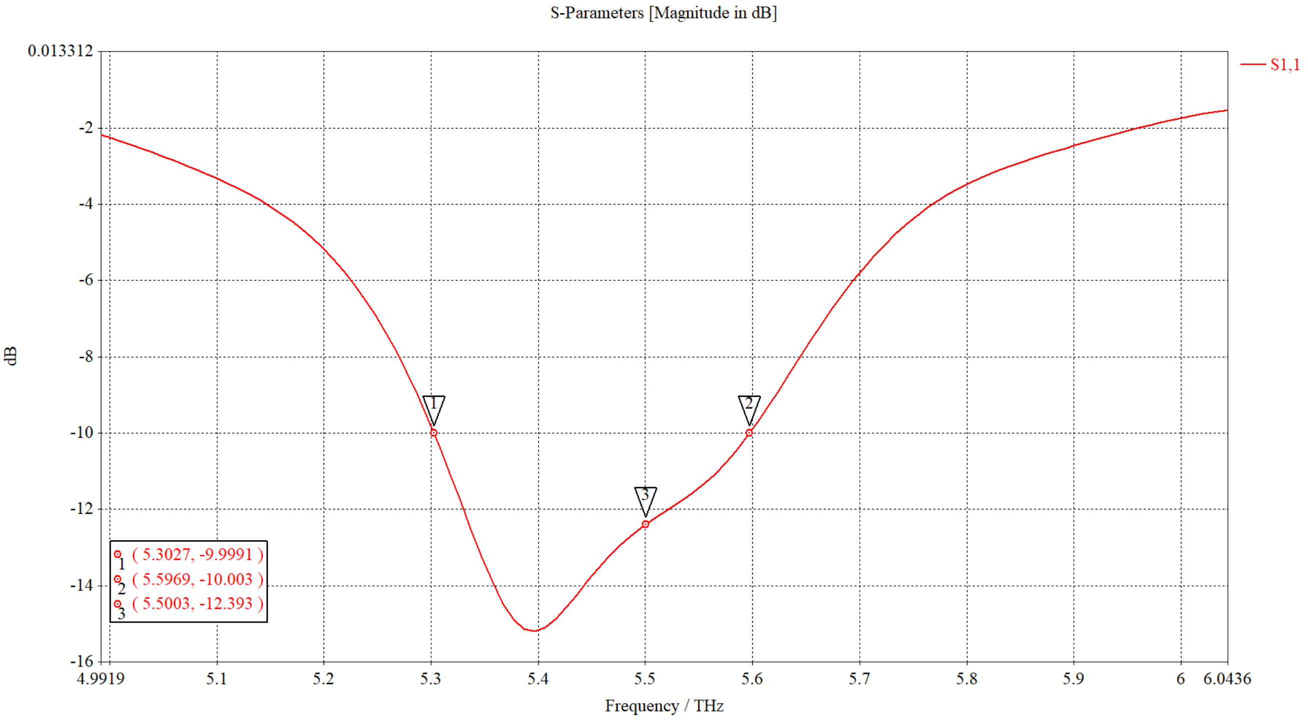

Figure 4.31 : S_{11} graph for RHCP Polarization of the antenna with cassini oval slots

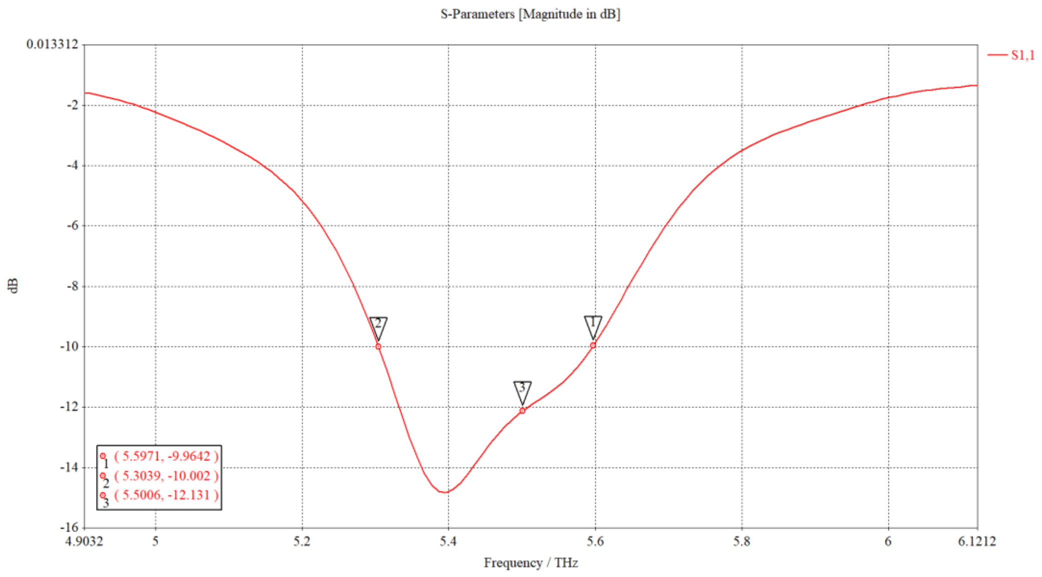

Figure 4.32 : S_{11} graph for LHCP Polarization of the antenna with cassini oval slots

S_{11} parameters for all polarizations of the design with Cassini slots are shown above. The antenna operating frequency range for linear polarization is 5.4 - 5.6 Thz, while the RHCP and LHCP antenna operating frequency range is 5.3 - 5.6 Thz. The bandwidth variation here is due to the intersection of the operating frequencies of the TM_{010} and TM_{100} modes, which will create circular polarization on the antenna. Since these two modes do not operate at exactly the same point, the bandwidth is increased.

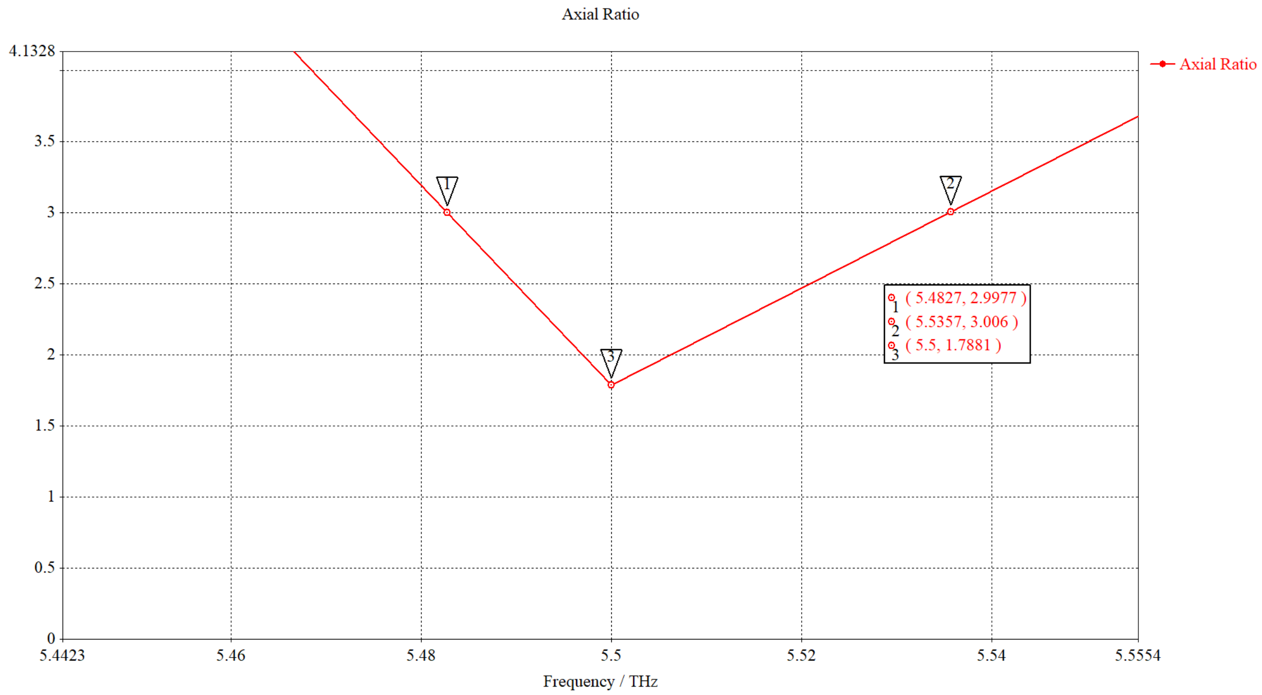

Figure 4.33 : Axial Ratio graph for RHCP Polarization

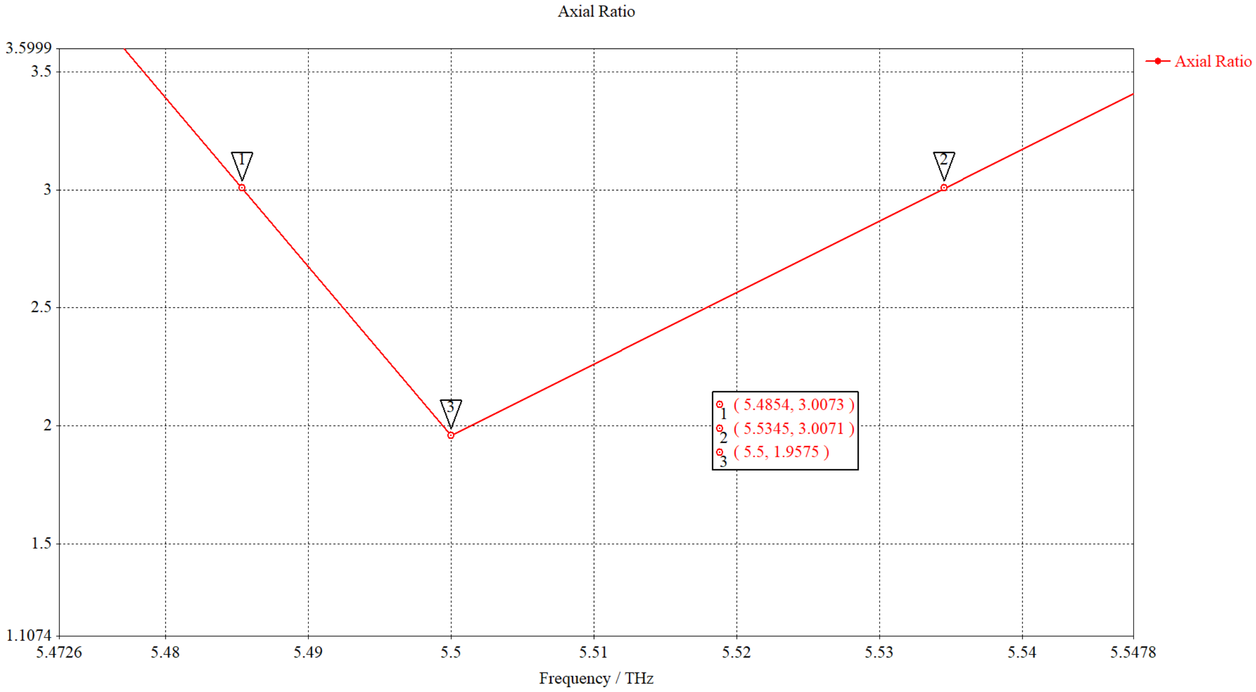

Figure 4.34 : Axial Ratio graph for LHCP Polarization

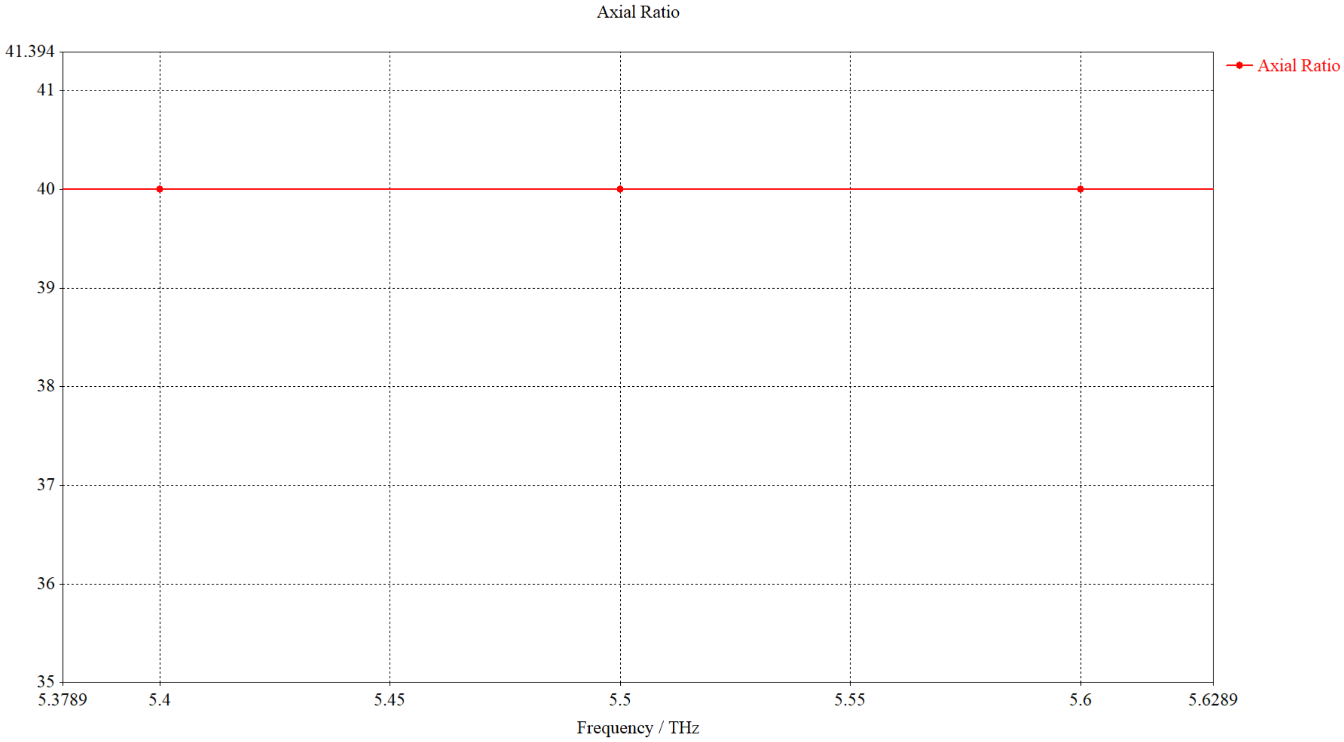

Figure 4.35 : Axial Ratio graph for LP Polarization

When the axial ratios of the configurations with RHCP and LHCP polarization are examined, it is observed that the lowest value for both polarizations is at 5.5 Thz, and they have circular polarization between 5.48 - 5.53 Thz. The axial ratio of the LP is 40 at 5.5 Thz. These measurements are made at the direction of the main lobe (φ=0, ϴ=0).

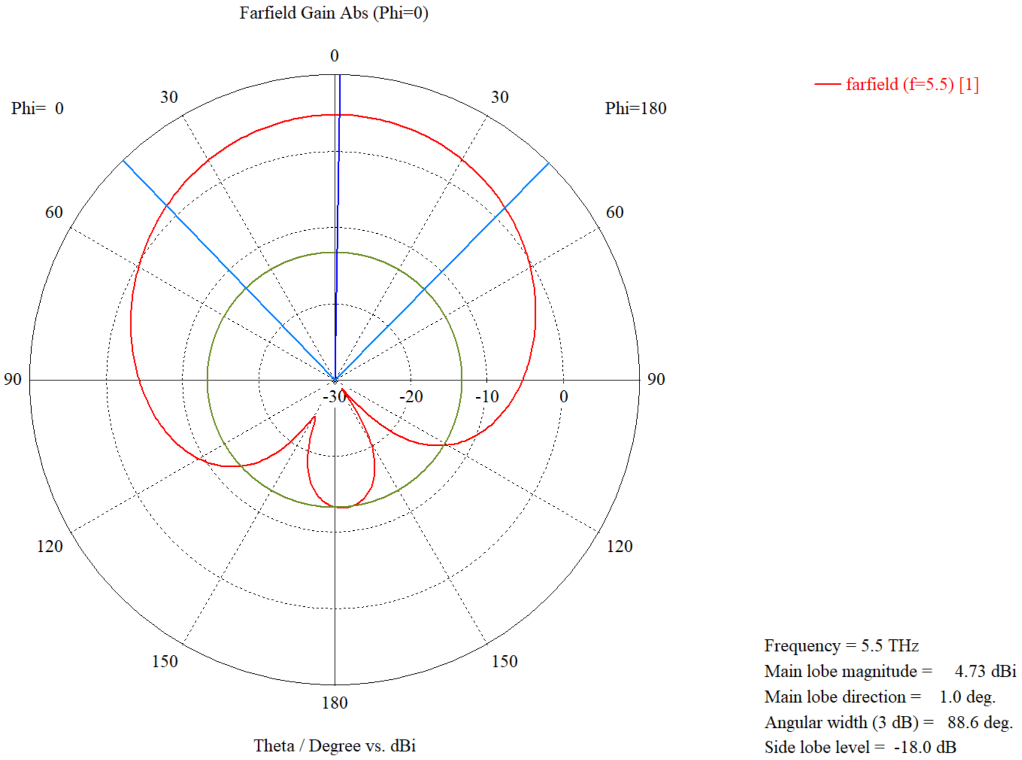

Figure 4.36 : Gain plot for LP antenna with Cassini Oval Slots

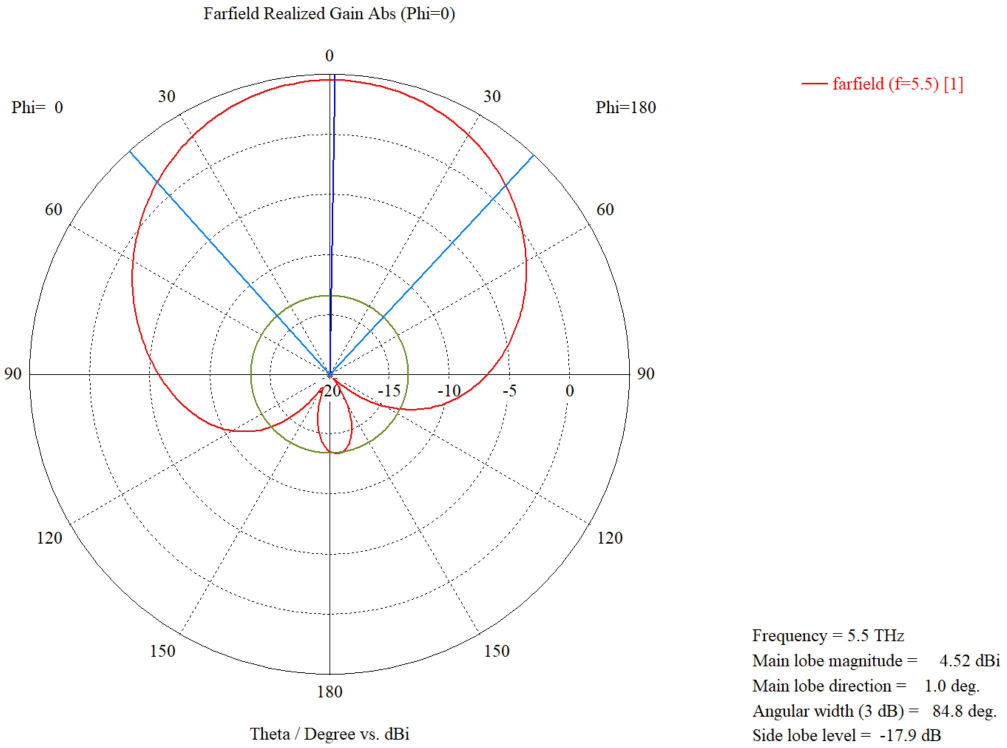

Figure 4.37 : Gain plot for RHCP antenna with Cassini Oval Slots

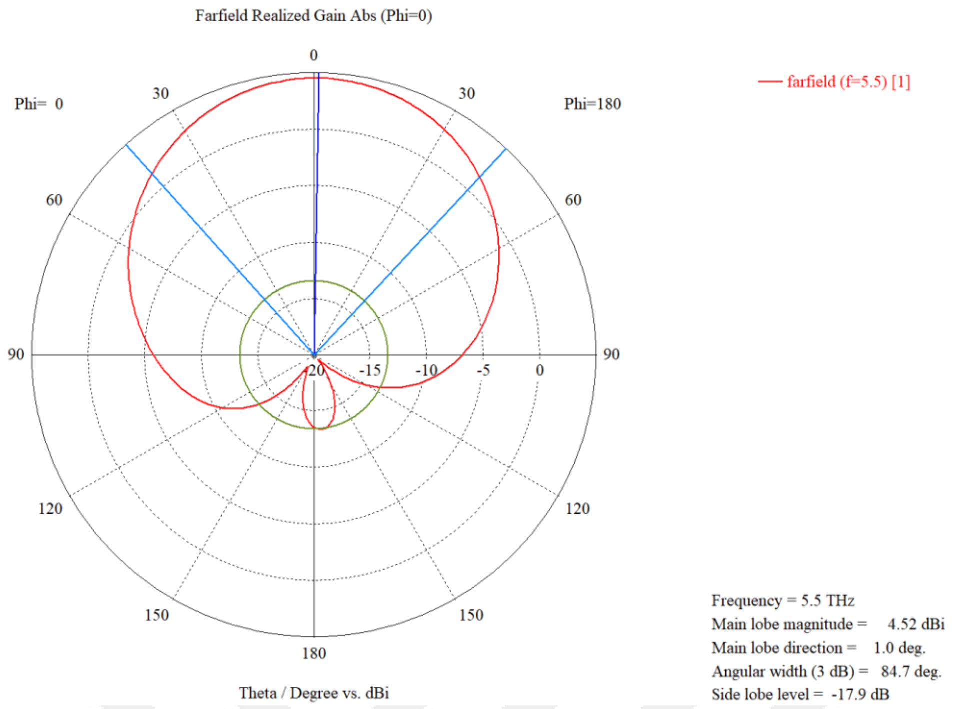

Figure 4.38 : Gain plot for LHCP antenna with Cassini Oval Slots

The figures above show that the antennas have similar radiation patterns for all polarizations. Accordingly, the antenna gain and directivity values are shown in the table below.

Table 4.6 : Antenna Gain and Directivity Table

Polarization	**Gain (φ=0, ϴ=0)**	**Directivity (φ=0, ϴ=0)**
LP	4.73 (dBi)	6.87 (dBi)
RHCP	4.52 (dBi)	6.87 (dBi)
LHCP	4.52 (dBi)	6.87 (dBi)

5. CONCLUSION

In this thesis, the basic models explaining the structure and working mechanisms of patch antennas are explained and then polarizable circular patch antenna designs using graphene and copper conductors are realized to operate at THz frequency. In the designs, circular polarizations are provided by the asymmetric slot insertion method. In this method, slot sizes are reduced in the direction of polarization rotation.

In the first design, it was observed that the operating frequency of the antenna was approximately 6 THz for all polarizations. In this study, the slots were placed with reference to the corner of the square tangent to the edges of the patch. According to the working simulations, the axial ratios in this structure are 2.65 and 2.72 for RHCP and LHCP, respectively. Since antennas with axial ratios below 3 dB are considered to have circular polarization, it is seen that the antenna structure provides all polarization transitions using a single structure.

In the second design, the aim is to reduce the axial ratio further to get closer to perfect circular polarization. For this, an asymmetric cross was placed in the center of the patch. The orientation of the asymmetry was changed by manipulating the chemical potential of graphene. In the developed structure, the antenna operates at 5.6 THz for RHCP and LHCP, while for LP, the operating frequency is shifted to 5.82 THz. In addition, the axial ratios are improved compared to the first study and are 0.3 and 0.34 for RHCP and LHCP, respectively.

In the third design, the aim is to control the antenna polarization by using fewer variable graphene regions and to observe the effect of adding a slot with circular edges in the structure on the bandwidth in contrast to the previous designs. When evaluated in line with these objectives, it is seen that the bandwidth is similar to the previous designs, and the radiation patterns are similar to the previous designs. The transition between polarization was achieved with graphene regions with two different bias voltages. Due to the size of the slots, the antenna operating frequency shifted towards the low-frequency region.

When the three studies are evaluated mutually, it is seen that the second structure has a better circular polarization. In addition, the operating frequencies of all polarizations are in the same region in the first structure. As a result of all these studies, LP, RHCP, and LHCP polarizations have been achieved by using surfaces whose conductivity can be controlled by using the properties of graphene material without changing the antenna structure or using active circuit elements.

In future studies, the best features of the three designs can be studied in the development of antennas that work in three different polarizations in the same working region, and circular polarizations are close to the ideal value of the “0” axial ratio and have improved bandwidth.

REFERENCES

[1] **W. L. Stutzman and G. A. Thiele**, *Antenna Theory and Design*. John Wiley & Sons, 2012. [Online]. Available: http://books.google.ie/books?id=xhZRA1K57wIC&printsec=frontcover&dq=Antenna+Theory+and+Design&hl=&cd=1&source=gbs_api

[2] **S.A Sahdman, K.S Islam, S.S Ahmed, S.S Siddiqui**, 2019. April Design and Comparative Analysis of Single-layer Graphene Microstrip Patch Antennas Operating at Terahertz Frequencies, Department of Electrical and Electronic Engineering at Brac University

[3] **Admin,** "Copper Cable vs Fibre Optic Cable Price, Is the Copper Really Cheaper? - Fiber Optic Components," *Fiber Optic Components*, Dec. 28, 2018. https://www.fiber-optic-components.com/copper-cable-vs-fibre-optic-cable-price-copper-really-cheaper.html

[4] **C. A. Balanis**, *Antenna Theory*. John Wiley & Sons, 2012. [Online]. Available: http://books.google.ie/books?id=v1PSZ48DnuEC&printsec=frontcover&dq=ANTENNA+THEORY+ANALYSIS+AND+DESIGN&hl=&cd=1&source=gbs_api

[5] **K. B. R. Cafe**, "Electronic Warfare and Radar Systems Engineering Handbook - Polarization - RF Cafe," Kirt Blattenberger, RF Cafe.

[6] **GEIM, A. and NOVOSELOV, K.** (2007). The rise of graphene. [online] Nature Publishing Group. Available at: http://www.nature.com/naturematerials [Accessed 18 Sep. 2018].

[7] **Novoselov, K. S., Geim, A. K., Morozov, S. V., Jiang, D., Zhang, Y., Dubonos, S. V., Grigorieva, I. V., and Firsov, A. A.** 2004. Electric field effect in atomically thin carbon films. Science 306 (5696): 666–669.

[8] **Bolotin, K. I., Sikes, K. J., Jiang, Z., Klima, M., Fudenberg, G., Hone, J., Kim, P., and Stormer, H. L**. 2008.Ultrahigh electron mobility in suspended graphene. Solid State Communications 146 (9–10): 351–355.

[9] **Bunch, J. S., van der Zande, A. M., Verbridge, S. S., Frank, I. W., Tanenbaum, D. M., Parpia, J. M., Craighead, H. G., and McEuen, P. L.** 2007. Electromechanical resonators from graphene sheets. Science 315 (5811): 490–493.

[10] **Lee, C., Wei, X., Kysar, J. W., and Hone, J.** 2008. Measurement of the elastic properties and intrinsic strength of monolayer graphene. Science 321 (5887): 385–388.

[11] **Bae, S., Kim, H., Lee, Y., Xu, X., Park, J.-S., Zheng, Y., Balakrishnan, J., Lei, T., Ri Kim, H., Song, Y. I., Kim, Y.-J., Kim, K. S., Ozyilmaz, B., Ahn, J.-H., Hong, B. H.,And Iijima, S.** 2010. Roll-to-roll production of 30-inch graphene films for transparentelectrodes. Nature Nanotechnology 5 (8): 574–578.

[12] **Kim, K. S., Zhao, Y., Jang, H., Lee, S. Y., Kim, J. M., Kim, K. S., Ahn, J.-H., Kim, P., Choi, J.-Y., and Hong, B. H.** 2009. Large-scale pattern growth of graphene films for stretchable transparent electrodes. Nature 457 (7230): 706–710.

[13] **Balandin, A. A., Ghosh, S., Bao, W., Calizo, I., Teweldebrhan, D., Miao, F., and Lau,C. N.** 2008. Superior thermal conductivity of single-layer graphene. Nano Letters 8 (3):902–907.

[14] **H. Philip Wong and D. Akinwande,** *Carbon nanotube and graphene device physics*. Cambridge University Press 2011, p. pages 49.

[15] **B. Helbig,** "1. Propagation of Electromagnetic Waves in Graphene Waveguides", Physik.uni-augsburg.de, 2019. [Online]. Available: https://www.physik.uni-augsburg.de/lehrstuehle/theo2/downloads/helbig.pdf. [Accessed: 13-Apr- 2019].

[16] **Llatser, I.; Kremers, C.; Cabellos-Aparicio, A.; Jornet, J.M..; Alarcon E.; and Chigrin D.N.** (2012). Graphene - based nano-patch antenna for terahertz radiation. Photonics and Nanostructures-Fundamentals and Applications, 10(4), 353-358.

[17] **Geim, A. K. &Novoselov, K. S.** The rise of graphene. Nature Materials 6, 183{191 (2007).

[18] **B. R., M. A. and M. S.**, "MATHEMATICAL FORMULATION OF SURFACE CONDUCTIVITY FOR GRAPHENE MATERIAL", *Core.ac.uk*, 2019. [Online]. Available: https://core.ac.uk/display/88830145. [Accessed: 23- Apr- 2019].

[19] **Razavizadeh M. S**, "2017 Simulation of Graphene in CST Microwave v2015 and COMSOL Multiphysics5.2a2017 [Online] Available: https://www.researchgate.net/publication/312146956_Simulation_of_Graphene_in_CST_Microwave_v2015_and_COMSOL_Multiphysics_52a. [Accessed: 11- Apr- 2019].

[20] **Slonczewski, J. C. & Weiss, P. R.** Band structure of graphite. Phys. Rev. 109, 292{297 (1958).

[21] **F. Ghasemzadeh and A. Pourziad,** "Yagi-Uda Frequency Reconfigurable THz Graphene-Based Antenna," 2022 6th International Conference on Millimeter-Wave and Terahertz Technologies (MMWaTT), Tehran, Iran, Islamic Republic of, 2022, pp. 1-4, doi: 10.1109/MMWaTT58022.2022.10172111.

[22] **Azizi, Med Karim & Mohamed, Ksiksi & Ajlani, H. & Gharsallah, A..** (2017). Terahertz Graphene-Based Reconfigurable Patch Antenna. Progress In Electromagnetics Research Letters. Vol. 71. 69–76. 10.2528/PIERL17081402.

[23] **S. I. Elgiddawy, H. A. Malhat, S. H. Zainud-Deen, H. Hamed and A. A. Ibrahim**, "Reconfigurable Radiation Pattern of Yagi-Uda Array Based on Graphene Patch Sectors," 2023 40th National Radio Science Conference (NRSC), Giza, Egypt, 2023, pp. 25-32, doi: 10.1109/NRSC58893.2023.10152905.

[24] **M. Mokhayer, S. Jarchi and R. Faraji-Dana**, "Reconfigurable Graphene-Based metasurface for THz transmission angle control," 2022 6th International Conference on Millimeter-Wave and Terahertz Technologies (MMWaTT), Tehran, Iran, Islamic Republic of, 2022, pp. 1-4, doi: 10.1109/MMWaTT58022.2022.10172113.

[25] **Y. Wang, Z. Guo, C. Li and X. Yan**, "Design of graphene frequency reconfigurable antenna in terahertz band," 2023 5th International Conference on Electronic Engineering and Informatics (EEI), Wuhan, China, 2023, pp. 521-525, doi: 10.1109/EEI59236.2023.10212546.

[26] **A. Sharma and D. K. Vishwakarma**, "Beam Steering of Graphene-Based Terahertz Antenna Array with Circular Polarization," 2023 IEEE 7th Conference on Information and Communication Technology (CICT), Jabalpur, India, 2023, pp. 1-3, doi: 10.1109/CICT59886.2023.10455514.

[27] **D. Samantaray, A. Shubham, S. K. Ghosh, S. Dwivedi and S. Bhattacharyya,** "A Graphene Patch Antenna with Improved Performance for THz Applications," 2023 IEEE Wireless Antenna and Microwave Symposium (WAMS), Ahmedabad, India, 2023, pp. 1-3, doi: 10.1109/WAMS57261.2023.10242933.

[28] **Won-Sang Yoon, Sang-Min Han, Seongmin Pyo, Jung-Woo Baik, and Young-Sik Kim,** “A polarization switchable microstrip patch antenna with a circular slot,” 2008 Asia-Pacific Microwave Conference, Dec. 2008. doi:10.1109/apmc.2008.4958544

[29] **A. O. Asok and S. Dey,** "A CPW-Fed Square Slot Circularly Polarized Antenna With Asymetrie Stubs For Ultra Wideband Applications," 2020 IEEE International IOT, Electronics and Mechatronics Conference (IEMTRONICS), Vancouver, BC, Canada, 2020, pp. 1-5, doi: 10.1109/IEMTRONICS51293.2020.9216332.

[30] **Nasimuddin, Z. N. Chen and X. Qing,** "Asymmetric-Circular Shaped Slotted Microstrip Antennas for Circular Polarization and RFID Applications," in IEEE Transactions on Antennas and Propagation, vol. 58, no. 12, pp. 3821-3828, Dec. 2010, doi: 10.1109/TAP.2010.2078476.

[31] **J. Zaid and T. A. Denidni,** "Tunable circular-polarization antenna for RFID applications," 2015 IEEE International Symposium on Antennas and Propagation & USNC/URSI National Radio Science Meeting, Vancouver, BC, Canada, 2015, pp. 2411-2412, doi: 10.1109/APS.2015.7305594.

[32] **K. Agarwal, Nasimuddin, and A. Alphones,** “Compact asymmetric-slotted-slit patch based circularly-polarized antenna with reactive impedance surface substrate,” *Microwave and Optical Technology Letters*, vol. 54, no. 11, pp. 2505–2510, Aug. 2012, doi: 10.1002/mop.27147.

[33] **M. F. Ali and R. Bhattacharya,** “Tunable high-gain graphene patch antenna for THz massive MIMO applications using FSS,” *Optical and Quantum Electronics*, vol. 55, no. 13, Oct. 2023, doi: 10.1007/s11082-023-05326-2.

[34**] S. N. Hafizah Sa'don et al.,** "The Review and Analysis of Antenna for Sixth Generation (6G) Applications," 2020 IEEE International RF and Microwave Conference (RFM), Kuala Lumpur, Malaysia, 2020, pp. 1-5, doi: 10.1109/RFM50841.2020.9344731.

[35] **S. Azam, M. A. K. Khan, T. A. Shaem and A. Z. Khan**, "Graphene based circular patch terahertz antenna using novel substrate materials," 2017 6th International Conference on Informatics, Electronics and Vision & 2017 7th International Symposium in Computational Medical and Health Technology (ICIEV-ISCMHT), Himeji, Japan, 2017, pp. 1-6, doi: 10.1109/ICIEV.2017.8338605.

[36] **N. Kiani, F. Tavakkol Hamedani, and P. Rezaei**, “Switchable circular polarization in flower-shaped reconfigurable graphene-based THz microstrip patch antenna,” *Analog Integrated Circuits and Signal Processing*, vol. 118, no. 2, pp. 259–270, Dec. 2023, doi: 10.1007/s10470-023-02215-2.

[37] **N. Kiani, F. T. Hamedani, and P. Rezaei**, “Polarization controlling plan in graphene-based reconfigurable microstrip patch antenna,” *Optik*, vol. 244, p. 167595, Oct. 2021, doi: 10.1016/j.ijleo.2021.167595.

[38] **N. Kiani, F. T. Hamedani, and P. Rezaei**, “Polarization controlling idea in graphene-based patch antenna,” *Optik*, vol. 239, p. 166795, Aug. 2021, doi: 10.1016/j.ijleo.2021.166795.

CURRICULUM VITAE

Name Surname : Güner ATALIK

EDUCATION : B.Sc. 2018, Istanbul University, Engineering Faculty, Electric and Electronic Engineering Department

PROFESSIONAL EXPERIENCE AND REWARDS:

- 2019-2021 TEKİRDAĞ Arçelik Elektronik İşletmesi, Production Engineer
- 2021-2022 İZMİR Bitron S.P.A, Production and Project Engineer
- 2022-2023 İSTANBUL Deka Elektronik A.Ş, Production Engineer

PUBLICATIONS, PRESENTATIONS AND PATENTS ON THE THESIS:

- **Soltani, F., Atalık, G., Karaçuha, K.,** (2023). Yama Anten Minyatürleştirme Teknikleri. URSI-TÜRKİYE 2023 XI. Bilimsel Kongresi, Boğaziçi Üniversitesi, İstanbul